Stony Brook University

Quantum Transport in Electron Fabry-Perot Interferometers in Quantum Hall Regime

A Dissertation Presented

by

Ping Lin

to

The Graduate School

in Partial Fulfillment of the Requirements

for the Degree of

Doctor of Philosophy

in

Physics

Stony Brook University

May 2010

Stony Brook University

The Graduate School

Ping Lin

We, the dissertation committee for the above candidate for the Doctor of Philosophy degree, hereby recommend acceptance of this dissertation.

Vladimir J. Goldman - Dissertation Advisor
Professor, Department of Physics and Astronomy

Ismail Zahed - Chairperson of Defense
Professor, Department of Physics and Astronomy

Meigan Aronson
Professor, Department of Physics and Astronomy

Serge Luryi
Distinguished Professor, Department of Electrical and Computer Engineering

This dissertation is accepted by the Graduate School.

Lawrence Martin
Dean of the Graduate School

Abstract of the Dissertation

Quantum Transport in Electron Fabry-Perot Interferometers in Quantum Hall Regime

by

Ping Lin

Doctor of Philosophy

in

Physics

Stony Brook University

2010

This dissertation describes quantum Hall transport experiments on Fabry-Perot electron interferometers fabricated from GaAs/AlGaAs heterostructure material. The devices consist of an island separated from the two-dimensional (2D) electron bulk via two tunable constrictions. Front gates deposited in etch trenches permit to fine tune the device. When tunneling occurs in the constrictions, electrons perform closed orbits around the island, producing an Aharonov-Bohm oscillatory signal in the conductance. Quantized plateaus in longitudinal and Hall resistances of the device allow us to determine the Landau level filling in both the bulk and the constriction.

A comprehensive experimental characterization of quantum Hall and Shubnikov-de Haas (SdH) transport is presented in the first interferometer. Application of front-gate voltage affects the constriction electron density, but the 2D bulk density remains unaffected. Analyzing the data within a Fock-Darwin model, we obtain the front-gate bias dependencies of constriction electron density, and, extrapolating to zero magnetic

field, the number of 1D electric subbands resulting from the electron confinement in the constrictions.

In the same interferometer, by carefully tuning the constriction front gates, we find a regime where interference oscillations with period $h/2e$ persist throughout the transition between the integer quantum Hall plateaus 2 and 3, including half-filling. In our experiment, neither period nor amplitude of the oscillations show a discontinuity at half-filling, indicating that only one interference path exists throughout the transition.

In the second interferometer, etch trench depletion is such that in the fractional quantum Hall (FQH) regime, filling 1/3 current-carrying chiral edge channels pass through the constrictions and encircle an island of the 2/5 FQH fluid. In this regime, we observe magnetic flux and charge periods $5h/e$ and $2e$, respectively, corresponding to creation of ten $e/5$ Laughlin quasiparticles in the island. The observed experimental periods are interpreted as imposed by the anyonic statistical interaction of fractionally charged quasiparticles.

To my dearest parents

Contents

List of Figures

Acknowledgments

During my years at Stony Brook several people and organizations have contributed to this dissertation. The text of this dissertation in part is a reprint of the materials as it appears in our previous publications. The co-authors listed in the publications directed and supervised the research that forms the basis for this dissertation.

First and foremost, I would like to express my particular gratitude to my advisor Professor Vladimir J. Goldman for all the guidance, encouragement and financial support. It is through your tireless mentoring and hand by hand demonstrations that I gradually get involved in the subject we have studied. During the past three years, I have learned from you so much knowledge about the subjects, moreover, I have greatly benefit from your attitude of doing research, which is, being meticulous, well prepared, thoroughly thinking and hard working, which has become an invaluable treasure in my life. Thank you for making me a better physicist.

I would like to thank Dr. Fernando Camino and Dr. Wei Zhou for insightful discussion and great help. Especially during the initial stages of my work, Dr. Camino and Dr. Zhou showed me the instrumentations and taught me to conduct many tasks in the lab. Your friendship and help are very important to me.

Many thanks should go to the Physics Department office for creating such a nice and friendly study environment, to Pat Peiliker, Sara Luttterbie and Maria Hofer especially, for taking care of business; to Pete Davis and others involved with the liquefier room for the supply of liquid Helium.

Help by Xiaoxu Lu in the final stages of the preparation of the dissertation is gratefully acknowledged. Thank you for critically reading part of the manuscript and offering numerous suggestions to improve the presentation.

I have also been truly blessed to have wonderful friends during my years as a graduate student Thank you for the great memories to Ying Cai, Xiaoxu Lu, Fen Zhang, Xingzhi Yu, Jie Ren, Jiayin Sun, Yan Zhang, Xiao Shen, Rui Wei, Shu Lin Sookhyun Lee, Li Li, Jue Wang and Xin Chen. Your friendships and helps are priceless.

Last but not the least, many thanks to the people who have supported me emotionally, most importantly my parents and my sisters. Thanks you for your love and understanding.

Chapter 1

Introduction

This thesis presents a detailed experimental study of quantum transport in electronic Fabry-Perot interferometers, throughout both the integer and fractional quantum Hall regime. The study traces its history back to one of the most fascinating phenomena in solid state physics: the quantum Hall effect, a distinguishing feature of two-dimensional electron systems (2DES) at low temperature and strong perpendicular magnetic field.

The integer quantum Hall effect (IQHE) was discovered by Klaus von Klitzing et al. in 1980.[1] In the discovery, the Hall resistance of a Si MOS (metal-oxide-semiconductor) field-effect transistor was reported to have fixed values, which depend only on the fine structure constant and the speed of light, and is insensitive to the geometry of the device. For this observation, von Klitzing was awarded the 1985 Nobel Prize in physics.

After a short while, the experimental discovery of the fractional quantum Hall effect (FQHE) was reported by Tsui, Störmer and Gossard.[2] In their work, the quantized Hall resistance plateau at $R_{XY} = 3h/e^2$ was reported to occur accompanied with a minimum in dissipative longitudinal resistance R_{XX} in the magnetotransport of high-mobility and low density GaAs/AlGaAs devices at temperature $T < 5\,\mathrm{K}$. It was absolutely unexpected, since at that time, no theoretical work existed that predicted new structures in the magnetotransport coefficients under conditions representing the extreme quantum limit, when $R_{XY} > 1h/e^2$. Shortly after, in 1983, Laughlin proposed a variational wave

function to explain the FQHE. For their ground-breaking work, Tsui, Störmer and Laughlin were awarded the 1998 Nobel prizes in physics.

Ever since these two intriguing discoveries, considerable efforts have been devoted to the investigation of low-dimensional strongly-correlated electron systems, both experimental and theoretical. Many review articles[3-5] are written for the summary of the astonishing experiments, new theoretical understanding, and sophisticated techniques followed.

Most quantum Hall experiments are performed on GaAs/AlGaAs heterostructures. Because of the small effective mass m* of the electrons in GaAs [$m^*(\mathrm{Si})/m^*(\mathrm{GaAs}) \approx 3$], the Landau level splitting is larger compared to that in Si and the high-quality of the interface results in a high mobility of the two-dimensional electrons. Furthermore, graphene is a novel research interest in the study of quantum Hall effect.[6-8]

The phenomenon of quantum Hall effect is characterized by plateaus of vanishing longitudinal resistance and quantized Hall resistance. Figure 1.1 shows experimental longitudinal (R_{XX}) and Hall (R_{XY}) magnetoresistances plotted as a function of magnetic field in a GaAs/AlGaAs heterostructure, where both IQHE and FQHE were observed. The longitudinal resistance vanishes at different regions of B, indicating a current flow without dissipation. In the same region, Hall resistance develops plateaus with $R_{XY} = h/fe^2$, where f is called "exact filling", a principle quantum number of the quantum Hall state. The unit, $h/e^2 = 25{,}812.807\Omega$ exactly, is adapted as the standard of resistance.

According to Laughlin,[9] the exactness of the Hall conductance quantization is understood as a consequence of gauge invariance and the existence of a mobility gap. The complete absence of dissipation at zero temperature can be understood by the assumption that in the plateau region the Fermi level lies in the localized states in the 2D bulk, and the applied current flows only in the extended edge channels at the periphery of the Hall bar. The R_{XY} remains quantized exactly even as Landau Level filling $v = hn/eB$ is varied from the exact filling f, because disorder localized extra electrons or holes. Changing of the magnetic field moves the Fermi level and when it passes through the extended states between the QHE, the transport becomes dissipative.

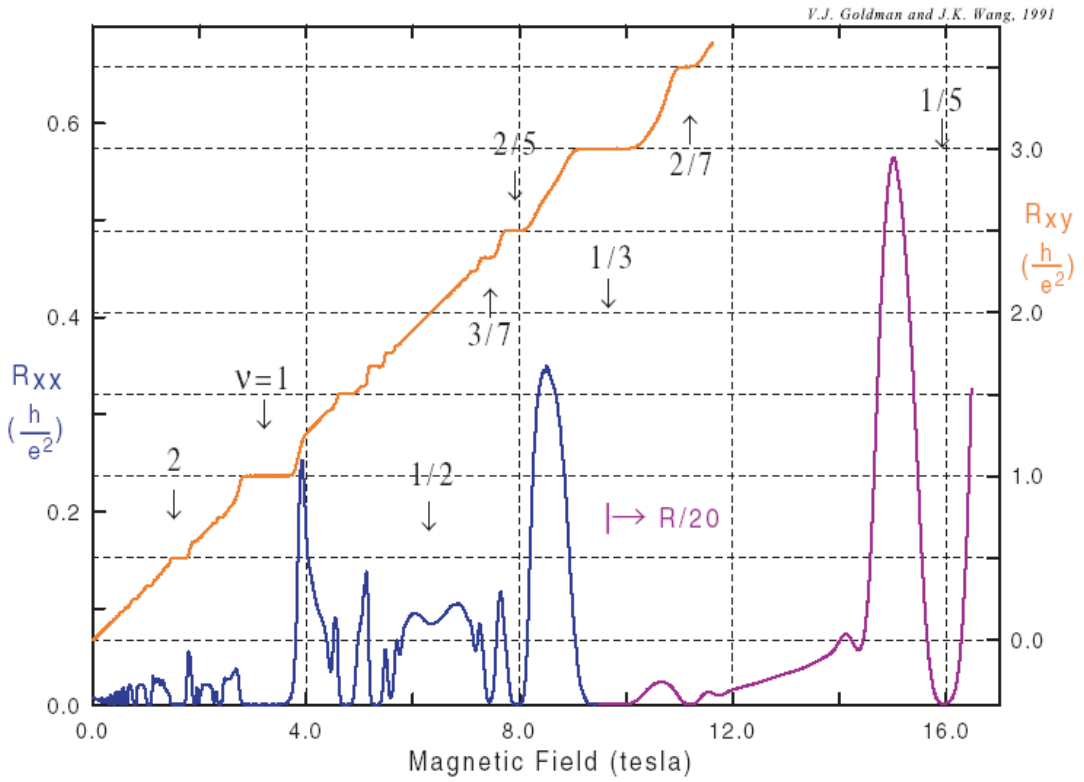

Figure 1.1: Representative experimental longitudinal resistance (R_{XX}) and Hall resistance (R_{XY}) as a function of magnetic field in a GaAs/AlGaAs heterostructure, where both IQHE and FQHE were observed. The Landau level filling factor ν is defined as $\nu = nh/eB$. (V. J. Goldman and J. K. Wang, 1991, unpublished, with permission)

The fractional quantum Hall effect at $f = 1/(2p \pm 1)$, where $p = 1, 2, 3, ...$ is an integer, is explained based on Laughlin's many electron wave function[10]. In the same work, Laughlin showed that quasiparticle excitations of FQHE state at $1/(2p+1)$ have fractionally-quantized electric charge $e/(2p+1)$. Halperin,[11] Arovas[12], Schrieffer[12] and Wilzeck[12] recognized that Laughlin's quasiparticles could be described by fractional statistics. Jain[13] developed a particularly transparent generalization of the Laughlin's theory and showed that the fractional QHE at $v \approx f = i/(2pi \pm 1)$ can be mapped onto the integer QHE at filling i using composite fermion (CF) theory.

The first direct measurement of the fractional charge of Laughlin's quasiparticles was reported in 1995[14] in Goldman's group at Stony Brook University. The fractional charge of Laughlin quasiparticles was observed in resonant tunneling experiments in quantum antidot devices. A quantum antidot (QAD) is a lithographically defined potential hill created by etching a hole placed in a constriction in a two dimensional electron system. Thereafter, QAD devices have attracted more and more interest to determine the fractional charge of Laughlin quasiparticles of the surrounding quantum Hall condensate[15-17].

The direct demonstration of fractional statistics was reported in 2005 in Goldman's group[18-20]. In their work, an inverse geometry to quantum antidot was utilized to observe the anyon. The novel geometry, called Fabry-Perot Interferometer (FPI), is shown in Figure 1.2. The Fabry-Perot Interferometer contains an electron island separated from the 2D bulk by two wide constrictions. In the quantum Hall regime, an edge channel of the 1/3 fractional quantum Hall fluid encircles an island of the 2/5 fluid. The magnetic flux affects the Aharonov-Bohm phase of the encircling 1/3 quasiparticles, and creates the 2/5 quasiparticles in the island. The superperiod is understood by the anyonic statistical interaction of Laughlin quasiparticles. The devices have attracted particular theoretical and experimental interest recently due to predicted signatures of fractional[11-12, 21-24] and non-Abelian statistics[25-27].

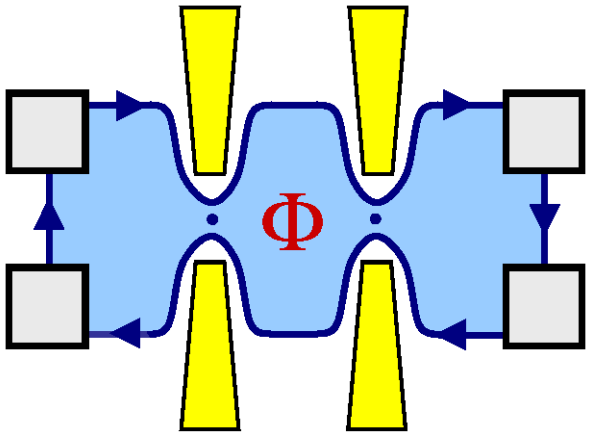

Figure 1.2: A quantum electron version of Fabry-Perot interferometer. Two wide constrictions defined by four metal gates (gold fingers) separate a 2D electron island from a bulk 2D electron gas contacted by a series of four electrodes (silver squares). A magnetic field quantizes the electron gas, which develops counterpropagating edge channels (blue lines with arrow), where quasiparticles can propagate without dissipation. When tunneling occurs in the constrictions (blue dots), quasiparticles circulate around these channels, and undergo quantum interference, which affects the measured conductance of the constrictions. The magnetic flux (Φ) passing through the electron island modulates the phase of the quasiparticles as they pass around the ring, and thereby how they interfere. As a result, varying this flux gives rise to periodic oscillations in the conductance -- known as the Aharonov-Bohm effect. (Nat. Phys. **3**, 517 (2007), with permission)

In the thesis, we present a detailed experimental characterization of electron Fabry-Perot interferometers both in the integer and fractional quantum Hall regime. These studies are motivated by application of similar interferometer devices in the fractional QH regime, where interference of fractionally charged Laughlin quasiparticles has been studied.[18-20, 28-31] Our approach is to investigate the properties of the devices in extremely wide magnetic field range, and study the behavior of the particles in low field and high field, including both IQHE and FQHE. Meanwhile, Aharonov-Bohm oscillations and fractional statistics are observed and corresponding discussion is presented.

The thesis is structured as follows:

In Chapter 2, a brief description of quantum Hall effect is given. The two-dimensional electron systems (2DES) realized in GaAs/AlGaAs heterostructure is described. The quantum mechanical treatment of 2DES is reviewed. The basic properties of quantum Hall effect, emphasizing the edge states and electron-electron interaction, are discussed.

In Chapter 3, the fabrication process and description of sample devices is presented; and the measurement setup and techniques used are discussed in details, together with the overview of the edge channel network model to calculate the four terminal resistances.

Chapters 4, 5 and 6 cover the results of the work. They follow, respectively, three research papers published in Physical Review B.

In Chapter 4, experiments addressing the quantum transport in low $B-$field are described. In the experiments, a systematic variation of front-gate voltage, V_{FG}, affects the constriction and the island electron density while the bulk density remains unaffected. A 1D Fock-Darwin model is employed to analyze the data. The constriction electron density as a function of the front-gate bias was obtained; and also, extrapolating to the zero $B-$field, the number of electric subbands (conductance channels) resulting from the electron confinement in the constrictions was obtained.

In Chapter 5, a study of an apparent h/fe Aharonov-Bohm flux period, where f is an integer, is presented. By carefully tuning the constriction front gates, a quantum regime was realized, where interference oscillations with period $h/2e$ persist throughout

the transition between the integer quantum Hall plateaus 2 and 3, including half-filling. An analysis of the front-gate dependence of the phase of the oscillating is presented. The result is discussed based on a single physical mechanism of the observed conductance oscillations: Aharonov-Bohm interference of interacting electrons in quantum Hall regime.

In Chapter 6, a different, not previously measured device is studied, and results in both integral and fractional regimes are presented. In the fractional regime, magnetic flux and charge periods $5h/e$ and $2e$, respectively, are observed. These periods were reported before in a much smaller interferometer device. They correspond to creation of ten $e/5$ Laughlin quasiparticles in the island. The observed experimental periods are interpreted as imposed by the anyonic statistical interaction of fractional-charged quasiparticles.

Finally, in Chapter 7 the conclusions of the dissertation and outlook of the future developments in the subject are given.

Chapter 2

Basics of Quantum Hall Effect

2.1 Two-Dimensional Electron Gas in GaAs/AlGaAs Heterostructure Material

A two-dimensional electron systems (2DES) was realized in the 1960's in the Si-MOSFET (Metal-Oxide-Semiconductor Field Effect Transistor). With the development of the fabrication techniques, the quality of 2DES realized was strongly enhanced. In 1970's, techniques were developed for growth of III−V semiconductor heterostructures. In modulation-doped semiconductor heterostructures, the carriers are spatially separated from the dopant atoms to reduce the ionized impurity scattering. In these structures, mobility much higher than that in the bulk can be attained. Moreover, because of the reduced disorder and scattering, such structures provide a nearly ideal system for studying many-body effects, such as the fractional quantum Hall effect, first observed in the high-mobility two dimensional electron systems at the interface of GaAs/AlGaAs heterojunctions. The realization of high-mobility ($\mu \sim 1\times 10^{6}\,\mathrm{cm}^{2}/\mathrm{V\,s}$) and nearly perfect 2DES in with low areal densities (around $1\times 10^{11}\,\mathrm{cm}^{-2}$) is of particular interest because it provides the means to study a wide regime of the 2DES in the extreme quantum limit. In the following, we provide a very brief discussion on the systems where the electron layers are created.

A schematic description of the cross-section through a wafer consisting of layers of GaAs and $Al_xGa_{1-x}As$ is shown in Figure 2.1:(a). The wafer is grown by Molecular Beam Epitaxy (MBE), which employs the atomic-plane doping technique as well as ultra-thick spacer with graded composition; in this case it produces a nearly perfect lattice-matched semiconductor/semiconductor interface. GaAs is a III-V compound, and it is tetravalent on average, therefore, it forms a diamond-like crystal, with the cubic zinc sulfide structure, where each As atom is surround by four Ga atoms and vice versa. It is well known that GaAs is a single-valley, direct gap, isotropic insulator and the Fermi level lies between the valence band and conduction band. Substituting a fraction (~40%) of the Ga atoms by Al, the resulting $Al_xGa_{1-x}As$ has similar structure as GaAs, but a wider band gap. MBE allows growing layers of $Al_xGa_{1-x}As$ on top of the GaAs substrate with atomically sharp interface. The lattice constants of GaAs and $Al_xGa_{1-x}As$ are almost the same so that the interface is nearly free from any disorder. The corresponding band diagram of the heterostructure is shown in Figure 2.1:(b). The dashed line is the Fermi energy (roughly defined as the highest energy that electrons can have in equilibrium at low T). The conduction bands (the lowest energy electrons can have) of GaAs and AlGaAs are offset from each other, and this allows electrons to collect in the GaAs but not in the AlGaAs.

When silicon is doped into the middle of the $Al_xGa_{1-x}As$ region (shown in red), the Fermi level on the $Al_xGa_{1-x}As$ side lies just above the bound state of the donors, which lies higher than the bottom of the GaAs conduction band. Therefore, electrons from the donors can be excited thermally, or by exposure to light, and move from the doped $Al_xGa_{1-x}As$ across the interface into the low-lying band near interface, states of the narrower band gap in GaAs; though they cannot go too far away because they are attracted back to the positive ions. The electric field due to the charge transfer bends the energy bands as shown in Figure 2.1:(c), where there is a triangular "quantum well" at the interface, and this goes slightly below the Fermi energy, so that electrons can collect there. The electrons are confined to the interface, and thus occupy well defined energy levels.

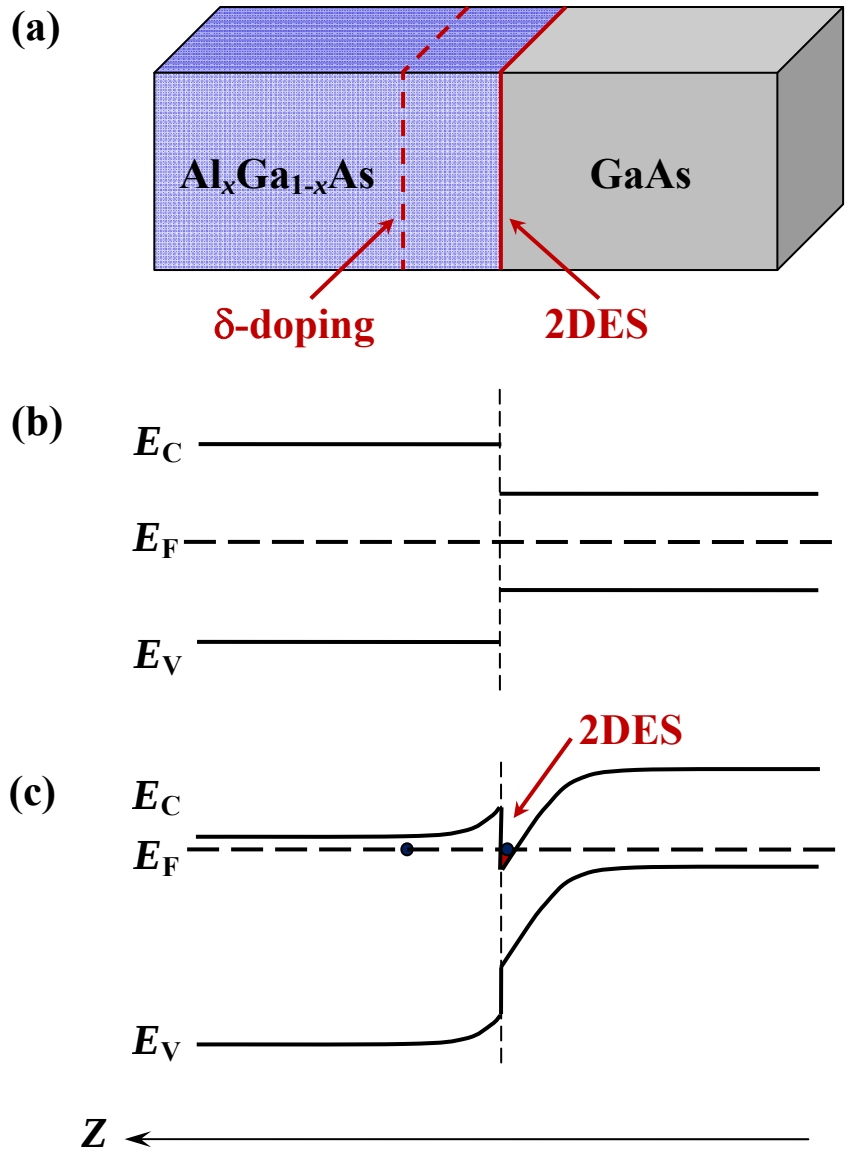

Figure 2.1: (a) a schematic description of GaAs/AlGaAs heterostructure. A thin layer of silicon, as shown in the red dashed line, is doped in the middle of the $Al_xGa_{1-x}As$ region. The two-dimensional electron system (2DES) is realized in the interface of AlGaAs and GaAs. (b) Energy levels of heterojunction without donors. E_C denotes the conduction band, E_V denotes the valence band, E_F denotes the Fermi energy. (c) Energy levels of heterojunction with donors. Electrons (black circles) are collected in the triangular "well" at the interface (the red triangle), and confined to move in the plane parallel to the interface, and so is quasi two-dimensional, at low T .

For a typical doping of $Al_xGa_{1-x}As$ with $x = 0.3$ and donor concentration of order $10^{11}cm^{-2}$, only the lowest quantum well level is occupied, and so the motion of the electrons perpendicular to the interface can be ignored at a low temperature $T \leq 10K$. However, it should be noted that the electron wavefunction in the lowest subband has some extent in the direction perpendicular to the 2D plane, which is comparable to several effective GaAs Bohr radius $a^* = \frac{m}{m^*}\varepsilon a_0 = 10.2\,nm$, where electron effective mass $m^* = 0.067m_e$ and dielectric constant $\varepsilon = 13$ in GaAs. But, the electrons are free to move in the plane parallel to the interface, and so is quasi two-dimensional.

In this structure, two-dimensional electrons are formed at the interface of $Al_xGa_{1-x}As$ and GaAs, while the doped donors are located several a^* away from the heterojunctions. The spatial separation of donors from the 2D electrons reduces electron scattering from the ionized donors. Moreover, the atomically sharp interface causes less scattering due to interface roughness. This results in a high quality and high mobility electron systems, in which the effect of the impurities is weak. In addition, the small effective electron mass, gives rise to a larger cyclotron frequency $\omega_C = eB/m^*$, which results in a larger separation of Landau levels, and facilitates the observation of quantum Hall effect. Low-temperature quantum magnetotransport measurements in these structures exhibit unprecedented, well-resolved, and well-developed FQHE states confirming the low disorder in these structures.

The equilibrium electron density of the 2D system is initially determined as the crystal is grown. However, it is possible to adjust the density by applying a perpendicular electric field to the interface, by applying a metal gate electrode near the interface.

2.2 2DES in Perpendicular Magnetic Field

For a 2D electron system subjected to a uniform perpendicular magnetic field B, ignoring the electron-electron interaction and spin, the Hamiltonian of a single electron is expressed as:

$$\mathrm{H} = \frac{1}{2m^*}(-i\hbar\nabla + \frac{e}{c}A)^2, \tag{2.1}$$

where m^* is electron effective mass, A is the vector potential which is related to the magnetic field $B = \nabla \times A$.

The electron energy is quantized into discrete energy levels. These quantized Landau levels have energy spectrum as:

$$E_n = (n + \frac{1}{2})\hbar\omega_C, \tag{2.2}$$

where $\omega_C = eB/m^*$ is the cyclotron frequency, and $n = 0,1,2,...$ is a quantum number called Landau level (LL) index.

Considering the spin of electron, each Landau level is split further into two levels, which are referred to spin-polarized Landau levels. The separation of the two spin-polarized Landau Levels that belong to the same Landau level is given by the Zeeman energy $\mu_B g^* B$, where μ_B is the Bohr magnetron, and $g^* \simeq -0.42$ is the effective conduction band Laude factor in GaAs.

The density of states of the 2DES, i.e. the number of states in each the Landau level per unit aera, $D(E)$ is very important to understand QHE. In the absence of impurity, Dirac $\delta-$function is introduced for the discrete quantized Landau level. $D(E)$ is defined as :

$$D(E) = \frac{eB\delta(E)}{h}. \tag{2.3}$$

Considering the magnetic length $\ell_0 \equiv \sqrt{\hbar/eB}$, the density of states $D(E)$ can be expressed in terms of the magnetic length ℓ_0 as

$$D(E) = \frac{1}{2\pi \ell_0^2} \delta(E) . \tag{2.4}$$

Introducing the magnetic flux $\Phi = BS$, and the flux quantum $\Phi_0 = h/e$, the The density of states $D(E)$ can be rewritten as

$$D(E) = \frac{\Phi / S}{h/e} \delta(E) = \frac{\Phi / S}{\Phi_0} . \tag{2.5}$$

Therefore, the number of spin-polarized electron states in each Landau level is understood as the total number of flux quanta per unit area in the external magnetic field.

In 2D transport measurement, another important parameter is the dimensionless electron Landau level filling factor of the Landau level, which is defined as

$$\nu = \frac{nh}{eB} = \frac{n}{B/\Phi_0} = \frac{\text{density of } e^-}{\text{density of } \Phi_0} , \tag{2.6}$$

where n is the electron density in the system. As shown in the expression, the electron Landau level filling factor can be understood as the ratio of number of electrons over the number of flux quanta for a given area. The number of flux quanta is defined in units of the flux quantum $\Phi_0 = h/e$.

For impurity-free system, the energy spectrum is a sequence of $\delta-$functions, one for each discrete spin-polarized Landau level, as shown in Figure 2.2(a). In a more general case, in the presence of impurities in the system, Landau levels are broadened into bands of extended states separated by tails of localized states, as shown in Figure 2.2(b). The localized states are in the tails of $D(E)$, and the extended states lead to a finite conductivity σ_{XX} and to a contribution to the Hall current in the region of the maximum of $D(E)$.

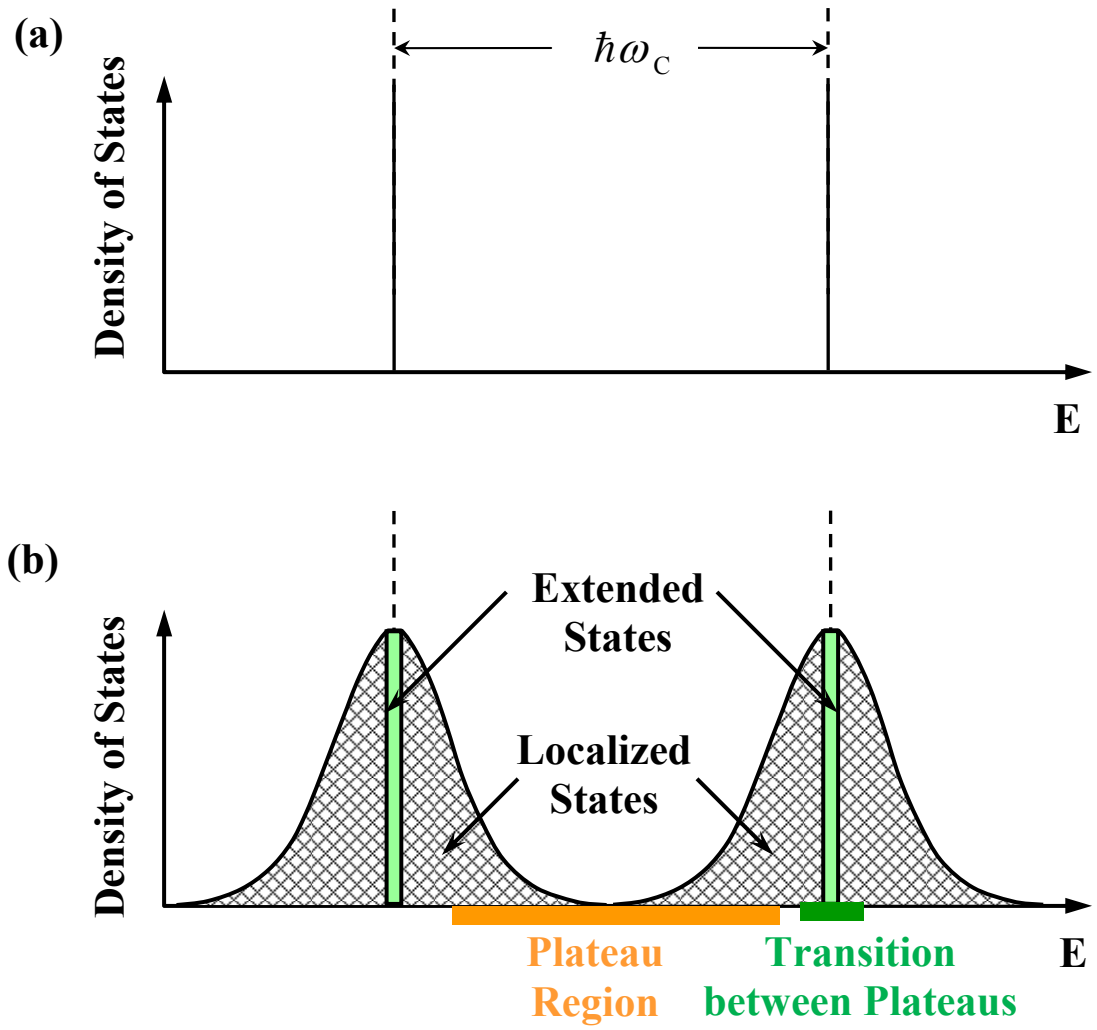

Figure 2.2: Density of states in a 2D electron system in a strong magnetic field. ω_C is the cyclotron frequency. (a) Discrete Landau levels in impurity-free 2DES system. (b) In the presence of disorder, Landau levels are broadened into bands of extended states separated by tails of localized states. In quantum Hall effect, the plateau appears when Fermi level lies in localized states. While Fermi level is located in the extended states, the Hall resistance shows a transition between plateaus.

2.3 Integral Quantum Hall Effect

The most conspicuous feature of integer quantum Hall effect is the observation of quantized Hall plateaus with values given by the Hall resistance $R_{XY} = V_Y / I_X = h / f e^2$ ($f = 1, 2, 3, ...$). When the Hall resistance is quantized, the diagonal resistance $R_{XX} = V_X / I_X$ will approach zero: the sample is in a dissipationless state.

While the Landau level filling factor $\nu = nh / eB$ of the 2D electron system is a variable and can be changed continuously, the quantum Hall exact filling f is a principal quantum number, defined by the quantized Hall resistance as $f = h / e^2 R_{XY}$. QH plateaus have finite width, that is, a $B-$region with different ν has the same f. In experiments, the filling factor ν can be changed either by changing the 2D electron density via a global back gate, or by changing the magnetic field.

The finite width of a Hall plateau is attributed to the broadening of Landau levels due to impurities. In the presence of impurities, the density of states of the 2D electron system can be described as in Figure 2.2(b). Each Landau level is broadened with tails consisting of localized states. However, there are extended states existing at the center of each Landau level. When f Landau levels are fully filled, the Fermi level is located in the gap between the f and $f+1$ Landau levels, where there are only localized states. Varying ν only changes the electron distribution within the localized states, which do not carry the transporting current. Therefore the Hall resistance is kept constant when the Fermi level resides in the localized states, resulting in the appearance of the characteristic plateaus.

Another point of IQHE that should be pointed out is the exactness of the quantization. The quantization of the Hall resistance to h / fe^2 is independent of the sample geometry, material, and contact details. Therefore, the origin of the quantization must depend on some fundamental properties of the 2D electron system. Laughlin[9] first proposed a general argument based on gauge invariance to demonstrate the exact

quantization of the Hall resistance. According to Laughlin's approach, the quantization is so accurate because it is based on two very general conditions, the gauge invariance of the electromagnetic field and the existence of a mobility gap in 2DES. As shown in Figure 2.3, a variation of Laughlin's *gedanken* experiment considers an annulus of two-dimensional electrons of areal density n with quantizing magnetic field B applied normal to annulus. The XY coordinates are chosen as shown in the figure: the X axis is along the radial direction and the Y axis is along the circumstance. A magnetic flux Φ through the center of the annulus changes at a constant rate. The electron Landau level filling is $\nu = hn/eB$. At low temperature T, the system of electrons condenses into a QH state. Let us consider the case of the integer QHE, where the integer $f = 1, 2, ...$ is the number of Landau level occupied by electrons, and the exact filling occurs at $\nu = f$.

Let us see what happens when we change magnetic flux Φ. The magnetic flux Φ passes through the center (the hole) of the annulus and does not exist at the 2DES, thus the magnetic field an electron on the annulus feels is independent of Φ. However, the vector potential of the field affects the motion of electrons. Therefore, a change of the vector potential because of the change of magnetic flux Φ is a gauge transformation, $A \to A + \delta A = A + \delta\Phi / L$, where L is the circumference of the loop. The electron wavefunction is changed according to

$$\Psi' \to \Psi \exp(i \frac{e}{\hbar} \frac{\delta\Phi}{L} y) = \Psi \exp(2\pi i \frac{\delta\Phi}{\Phi_0} \frac{y}{L}). \tag{2.7}$$

In the condition that all the states are localized, the wave function is finite and vanishes outside a localization region which is smaller than L, and the memory of the phase is lost as the wavefunction vanishes somewhere. In this case, the system will not respond to the flux and the energies of localized states are unchanged.

On the other hand, when the electron states are extended at the edges of the annulus, such a transformation must satisfy the condition that $\delta\Phi / \Phi_0$ is an integer, since the wave functions are required to be single-valued.

Let us consider adding adiabatically one flux quantum $\Phi_0 = h/e$ in the inner hole of the annulus. Since the flux is added in the whole, the state of the electron system must map identically into itself as that before flux was added (gauge invariance). Therefore,

the net result of the adiabatic adding one Φ_0 is that one electron per occupied Landau level is transferred between the inner and the outer edges of the annulus (provided they are connected by a wire). Thus, in the steady state, we add $\delta\Phi = \Phi_0$ every δt, the magnetic flux Φ through the annulus center changes at the rate $d\Phi / dt = \Phi_0 / dt$. According to the Faraday's induction law, the azimuthal voltage (emf) is $V_Y = -\Phi_0 / dt$. On the other hand, the radial Hall current is $I_X = -ie / \delta t$, the charge transferred in one Landau level per δt times the number of occupied Landau levels. Thus the Hall resistance $R_{XY} = V_Y / I_X = h / f e^2$.

To summarize, for the integer quantum Hall effect, the quantum Hall energy gap is provided by the energy separation of two successive Landau levels. The relevant quasiparticles are just electrons and holes. By varying the filling factor, creation of quasiparticles can be achieved by redistribution of electrons to the next empty Landau level or by creating holes in the highest filled Landau level. What is important is that R_{XY} remains quantized exactly even as ν is varied from the exact QH filling *f*, because disorder localize extra electrons or holes, and thus the diagonal resistance R_{XX} along an edge is zero.

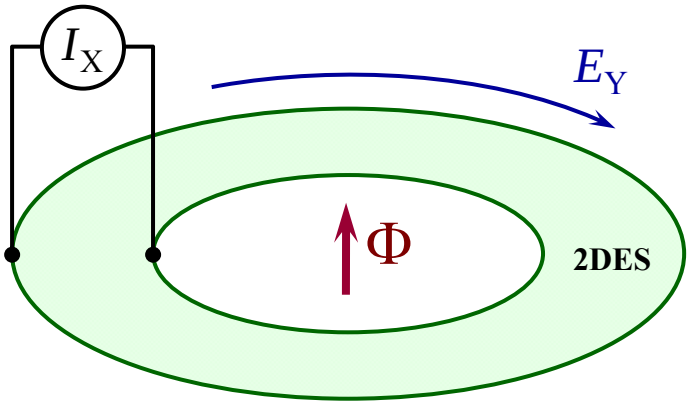

Figure 2.3: Laughlin's *gedanken* experiment to demonstrate the exactness of quantization of Hall resistance on a QH plateau. Magnetic flux Φ through the center of the annulus of two-dimensional electrons of areal density n changes at a constant rate thus inducing azimuthal electric field E_Y. The X axis is chosen along the radial direction, and the Y axis is chosen along the circumference of the annulus. The loop integral of E_Y is V_Y, and it corresponds to the radial Hall current: $V_Y = I_X R_{XY}$.

2.4 Fractional Quantum Hall Effect

FQHE is characterized by the fact that the Hall conductance has plateaus quantized to certain simple fractions ν of the unit e^2/h, and at the same places, the longitudinal conductance shows an almost dissipationless current flow. The fact that only part of the lowest Landau level is occupied indicates that the non-interacting single electron explanation for IQHE is inadequate for FQHE, because the energy gap cannot come from the gap between successive Landau levels. The electron-electron interaction must be prominent in the FQHE.

Our understanding of FQHE is based on Laughlin's many-electron wavefunction,[10, 32] which provides an excellent description of the primary filling FQH sequence $f = 1/m$ (m odd). The wave function is written as:

$$\Psi_m = \prod_{j<k} (z_j - z_k)^m \exp\left(-\frac{1}{4\ell_0^2} \sum_l |z_l|^2 \right), \tag{2.8}$$

where $z = x + iy$ denotes the complex coordinate of the electrons in the 2D plane. With corrections for Landau level mixing, the results of the calculated energy gap agree well with experimental data from high-quality 2D electron system.[10, 33-34]

The FQHE is understood as resulting from condensation of interacting electrons into a highly-correlated incompressible fluid. The elementary charged excitations of a FQH condensates are the Laughlin quasiparticles, as predicted from Laughlin's wave function. When the filling factor ν is not equal to the exact filling, either quasielectrons or quasiholes are excited out of the condensate. At such filling, the ground state of a FQH fluid consists of the exact filling condensate and the matching density of quasiparticles. For the filling $f = 1/m$, the FQH quasiparticles, quasielectrons and quasiholes, process fractional electric charge charge,[10, 14, 32, 35] $q = -e/m$ and $q = e/m$, respectively, and obey anyonic (fractional) exchange statistics, intermediate between the familiar Bose and Fermi statistics, thus, they are anyons.[11-12, 21-23]

After the fundamental work of Laughlin, a hierarchical model was proposed by Haldane[35] and Halperin[11] for the general FQHE states, $f = n/m$, with $n \neq 1$ an integer and m an odd integer number. It states that the quasiparticles of one *parent* condensate condense into a new fractional quantum Hall state, creating a *daughter* state. By applying this process repeatedly, all possible fractions can be obtained. In addition, it is pointed out that for the general filling $f = n/m$, the charge of the relevant quasiparticles is $\pm e/m$.

Another particularly transparent generalization of the Laughlin's theory has been developed by Jain. He showed that the fractional QHE at $\nu \approx f = \frac{i}{2pi \pm 1}$ can be mapped onto the integer case using composite fermion theory.[13, 36] A composite fermion is an electron bound to an even number $2p$ ($p = 1, 2, \ldots$) of vortices of the many-particle wave function. The binding results from Coulomb interaction between the electrons, and it has been shown that the exact FQH ground states are very close to those of the composite fermion theory. Also, the composite fermion theory predicts the hierarchy of the FQH states observed in nature.[37] Since, on the average, in an area, the number of vortices of the many-particle wave function is equal to the number of the flux quanta in units of Φ_0, in mean field theory, composite fermions can often be thought of as electrons each binding $2p\Phi_0$ of applied B. Thus composite fermions experience effective magnetic field $B_{cf} = B - 2pn\Phi_0$, and the filling of the pseudo "Landau levels" of composite fermions $\nu_{cf} = n\Phi_0 / |B_{cf}|$ corresponds to $\nu = n\Phi_0 / B = \nu_{cf} / (2p\nu_{cf} \pm 1)$. For $p = 1$, for example, the FQHE of interacting electrons at $f = \frac{i}{2i+1}$ looks like the IQHE of weakly interacting composite fermions at $i = i_{cf}$, with i_{cf} pseudo "Landau levels" occupied by composite fermions.

Fractionally charged quasiparticles were first observed in quantum antidot experiments, where quasiperiodic resonant conductance peaks are observed when the occupation of the antidot is incremented by one quasiparticle[14, 16, 38]. A quantum antidot is a small potential hill defined lithographically in the 2D electron system. Complementary geometry, where a 2D electron island is defined by two nearly open constrictions,

comprises an electron interferometer[19, 31, 39-40]. In Chapter 6, we report experiments in a quasiparticle interferometer where $e/3$ quasiparticles of $f = 1/3$ fluid execute a closed path around an island of $f = 2/5$ fluid.

Experiments show that FQHE states are sensitive to disorder. Low-mobility samples do not show a FQHE. The FQHE has a characteristic energy scale of only a few degree Kelvin. Moreover, there is a tendency for the quantized states with higher denominator to exhibit weaker transport features. The last but not the least, higher magnetic fields promote the observation of the FQHE.

In addition, experimental results clearly demonstrated that for the FQHE to occur, the odd denominators are favored exclusively. However, there has also been other surprise in the FQHE. In the second Landau level, the observation of a fractional Hell plateau at $\rho_{XY} = \left(\frac{h}{e^2}\right) \Big/ \frac{5}{2}$ was reported,[41-42] corresponding to an even denominator filling ($\nu = 2 + \frac{1}{2}$). The even denominator states are not discussed here since they involve more complex theoretical constructions and are not studied in our experiments.

2.5 Edge States in the Quantum Hall Effect

From the experimental point of view, it is clear that under the quantum Hall condition, the edge states play an important role in transport measurements. An electric current can flow through a device only when both the source and drain contacts are connected by a common edge. Halperin[43] pointed out that the current flows along the one-dimensional channel at the edge of the two-dimensional layer. The localized states do not play any part in the response to a changing flux. If there is a Hall current, there must be extended states to respond to the changing flux, and, in particular, the edge states at the Fermi energy must be extended.

Consider a noninteracting electron system confined by a boundary potential. The confining potential raises the energy of states near the edge and results in quasi-one-dimensional extended states along the edge, that is, the edge states. The total energy of a Landau level, kinetic energy plus that of a confining potential, is shown in see Figure 2.4. It has also been shown that the edge states can survive moderate disorder. On a quantized Hall plateau, the current is carried only by edge states, since in the bulk there are only localized states near the Fermi level. All edge states belonging to the same edge carry current in the same direction, determined by the perpendicular magnetic field B and the gradient of the confining potential. Edge states belonging to a given Landau level are also referred to as edge channels, and are typically represented as lines with arrows in a diagram.

When f Landau levels are occupied, f quasi-one-dimensional edge channels are produced at the Fermi energy on either side of the sample through which dissipationless current flows. MacDonald and Streda[44] showed that, if μ_R is the chemical potential at the right (positive y) edge of the sample and μ_L is the chemical potential at the left edge, the net current is

$$I = \frac{ef}{h}(\mu_R - \mu_L). \tag{2.9}$$

This expression shows that edge channels on opposite sides of the sample carry current in the opposite directions. A net current is established if there is a difference in the magnitude of these opposite flowing currents.

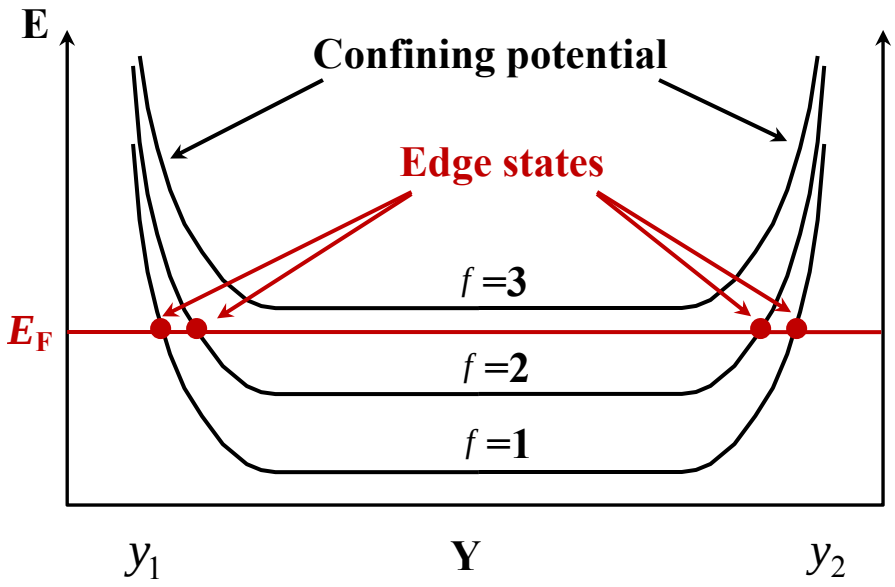

Figure 2.4: The energy spectrum of a noninteraction electron system with finite size. The boundaries of the 2DES are y_1 and y_2. Landau levels are labeled by f. At low temperature T, all electron states below Fermi energy E_F are occupied.

Chapter 3

Sample Preparation and Experimental Techniques

3.1 Sample Fabrication

Lithography techniques are required to fabricate devices with lower than two dimensional electron systems. The basic technique in semiconductor industry is photolithography, where patterns are transferred to the sample with the help of masks and resists that are sensitive to UV-light. The photolithography resolution is crucially limited by the wavelength of the light. In order to achieve even smaller scale design, electron beam (e-beam) lithography is employed. It is popular in research because of its relative simplicity, as the pattern is written directly onto the resist pixel by pixel, by scanning the e-beam around.

In the fabrication of our devices, first, macroscopic level optical lithography is employed o define a large scale mesa structure; then, finer scale front gates were defined by e-beam writing. A detailed fabrication process for interferometer geometry devices is present as follows. The parameters of a real sample may differ from the values as described here.

The sample is roughly a 4 × 4 mm square cut from the GaAs/AlGaAs wafer. The first processing step is the mesa pattern definition. The wafer is processed by 4-cycle cleaning, which is done by rinsing the wafer with Trichloroethylene (TCE), Acetone, Methanol, and de-ionized (DI) water in ultrasonic bath successively. Then the wafer is glued on a glass slide and a thin layer of photoresist is spinned onto the wafer. After

baking, the wafer is covered by an optical mask of the mesa pattern and exposed to ultraviolet light. After developing, the wafer is etched in $1H_2SO_4:8H_2O_2:100H_2O$ solution at 1.5 ºC for the desired depth. After etching, the remaining photo resist is removed in acetone. This completes the mesa definition.

Next, four Ohmic contacts at each corner of the sample are prepared by alloying with Indium metal at 410 ºC in Hydrogen atmosphere. Then the sample is gradually cooled to room temperature.

Then the gates of the sample are defined. First, the sample is processed by 4-cycle cleaning and glued to a macor holder. Then, the sample is coated with a thin layer PMMA electron resist and subsequently baked at 170 ºC for 30 min. These front gate patterns are defined by electron-beam lithography. After exposure to electron beam, the PMMA is developed. The developed sample is baked at 95 ºC and then etched to the desired depth in $1H_2SO_4:8H_2O_2:100H_2O$ solution at 1.5 ºC. This gate areas defined by etching are depleted of electrons even without a bias voltage on them due to the fact that they have been etched down beyond the level of dopants. After that, metal deposition is processed on the sample with the remaining photoresist on top of it. Then a 5 nm Ti layer followed by 45 nm Au is deposited on top of the sample. Subsequently, the sample is immersed in acetone for lift-off. Only the metal deposited in the etched front gate area will remain, the rest just comes off with the photo resist. This completes the front-gate process.

After the front gate definition, a global backgate is placed under the sample. First, a chip of single crystal sapphire is cut with slightly larger size than the sample. Then the sapphire chip is coated with a thin layer of Indium metal and heated on a hot plate. The sample is placed on top of the sapphire chip, with Indium melted in between. The Indium layer now serves the global backgate of the sample, see Figure 3.1.

At this stage, the sample is ready to cool down for experiments. To measure the transport of the sample, the sample is mounted to a header, which is a chip holder with pins that can be plugged into the sample probe. As seen in Figure 3.1:, four Ohmic contacts, four front gates, and the backgate contacts are connected to the header pins by gold wires,

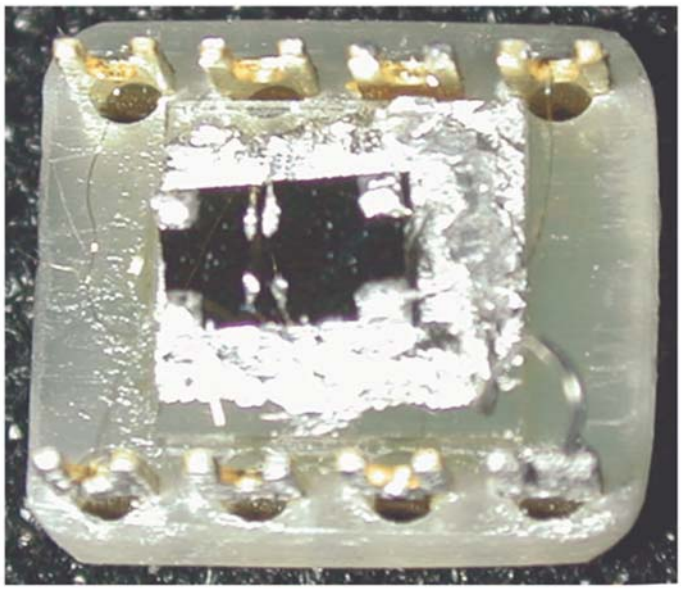

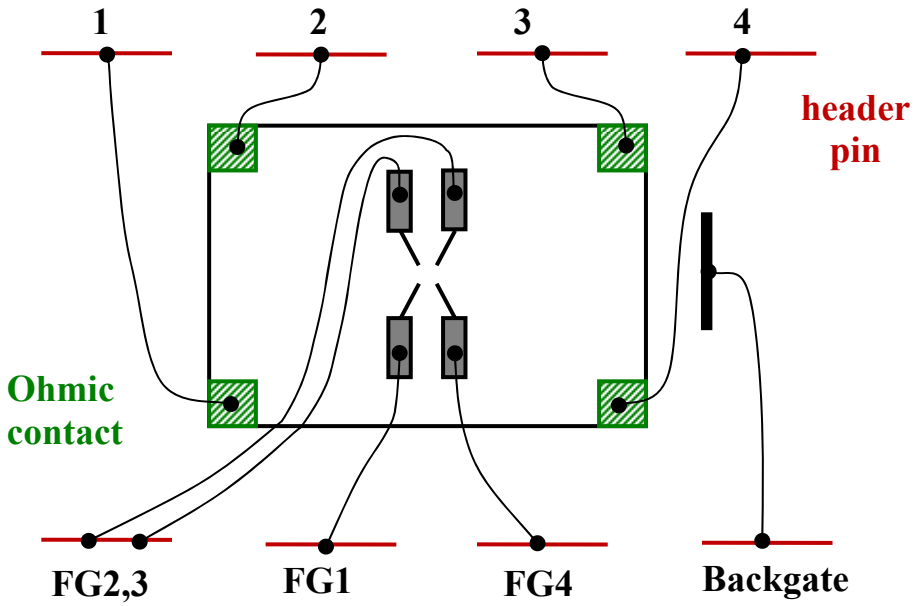

Figure 3.1: Top: The optical microscope photograph of the sample mounted on a header. The thick wire at the bottom right corner connects the backgate to the header pin. Buttom: the illusion scheme of the connection. Ohmic contacts and front gates (FG) are all connected to the header pins by gold wires. Indium metal, served as backgate, is spread all over the sapphire substrate, with the wafer chip placed on it.

3.2 Measurement Techniques

A Schematic diagram of the apparatus for four-terminal resistance measurement is shown in Figure 3.2. The sample is loaded into an Oxford Instruments TLM-400 top-loading-into-mixture ^{3}He-^{4}He dilution refrigerator. The header (with sample mounted) is plugged into the sample probe and inserted into the tail of the mixing chamber, which is located at the center of the magnet. During the measurement, the sample is immersed into ^{3}He-^{4}He mixture.

The superconducting solenoid magnet surrounding the tail of the mixing chamber produces nearly uniform magnetic field at the position where the sample is located. The sample is mounted on the probe in the way that the magnetic field is perpendicular to the sample. At liquid He temperature ($4.2\,\mathrm{K}$), the magnet provides high magnetic field up to $14\,\mathrm{T}$. With the operation of the λ-plate refrigerator attached to the magnet, a high field up to $17\,\mathrm{T}$ can be achieved. The magnet is powered by an IPS-120 power supply. There are two operating mode, ramp current mode and persistent current mode, can be easily controlled by a computer program.

The base temperature of the system is about $10\,\mathrm{mK}$ The sample temperature is measured by a calibrated Ruthenium Oxide (RuO2) chip resistor placed close to it. There is a red LED mounted on the probe, placed close to the sample. The desired 2D electron density is achieved by exposing the sample to LED light at $4.2\,\mathrm{K}$.

One critical issue in the experiment is to filter the electromagnetic noise travelling down the measurement wires that heats electrons in the sample, especially the electrons in the island. The electromagnetic environment incident on the sample is attenuated by a combination of RF-lossy manganine wire ribbons and a series of cold low-pass RC network filters with a combined cut-off frequency $\sim 50\,\mathrm{Hz}$. Extensive cold filtering cuts the electromagnetic "noise" environment incident on the sample to $\sim 7\times10^{-16}\,\mathrm{W}$, allowing us to achieve an effective electron temperature $\sim 15\,\mathrm{mK}$ in an interferometer device. [28]

The excitation current is from the oscillator output of the EG&G model 5302 lock-in amplifier. The resulting signal from the sample is detected by the same lock-in amplifier.

A schematic diagram of a four-terminal resistance measurement is shown in Figure 3.3. Four terminal resistance R_{XX} and R_{XY} are measured with lock-in technique. The longitudinal resistance $R_{XX} = V_X / I_X$ is measured with $5.4\,\text{Hz}$ AC current injected at contacts 1 and 4 and the resulting voltage V_X, including the Aharonov-Bohm oscillatory signal, is detected at contacts 2 and 3; for the Hall resistance R_{XY}, current is passed through contacts 1 and 3, and the resulting voltage V_Y is detected at contacts 2 and 4. The sample resistance is measured as a function of magnetic field (with ramp current mode) or backgate voltage (with persistent current mode). The four independently contacted front gates are connected to a high precision, high stability voltage source power. By biasing front gates, we can fine-tune the symmetry of constrictions, and change the electron density at the constrictions and the island. The back-gate voltage can be swept up or down continuously in the range within $-10\,\text{V}$ to $+10\,\text{V}$ with good precision by a ramp generator.

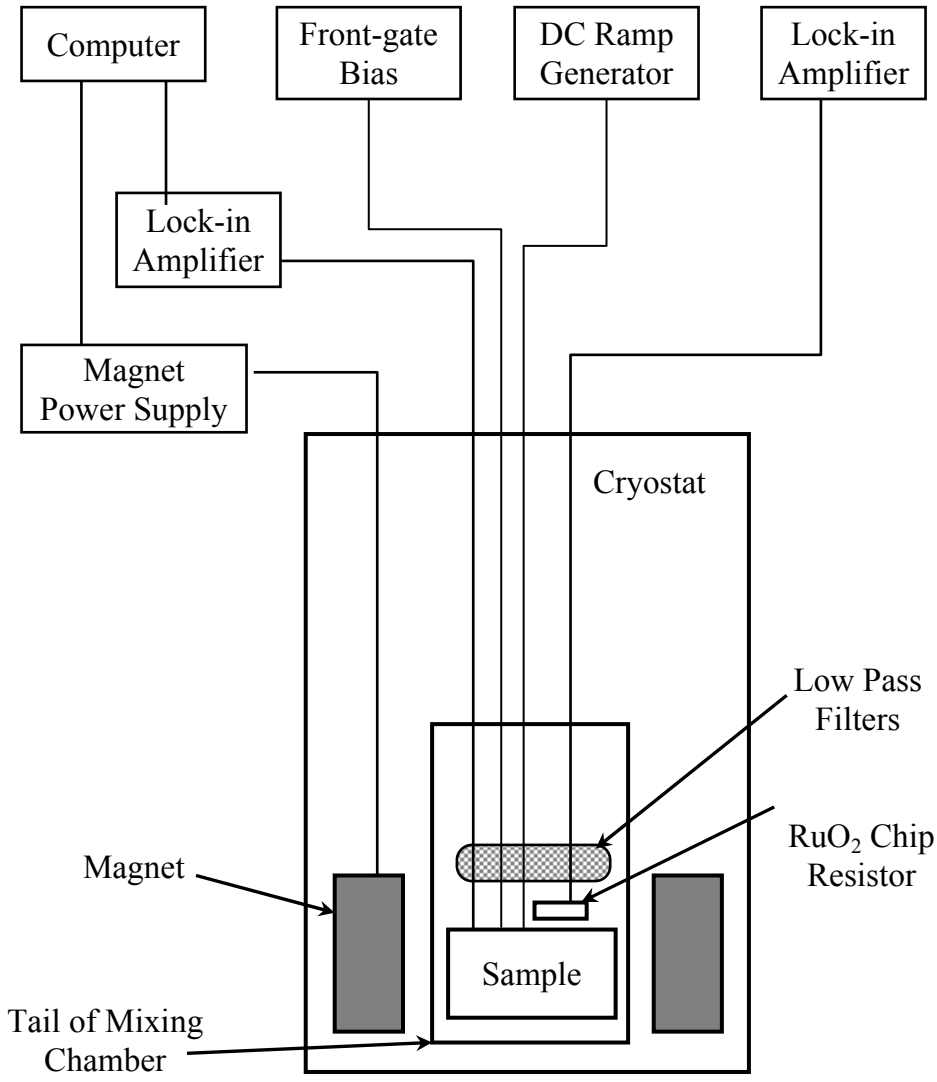

Figure 3.2: Schematic diagram of the apparatus for four-terminal resistance measurement.

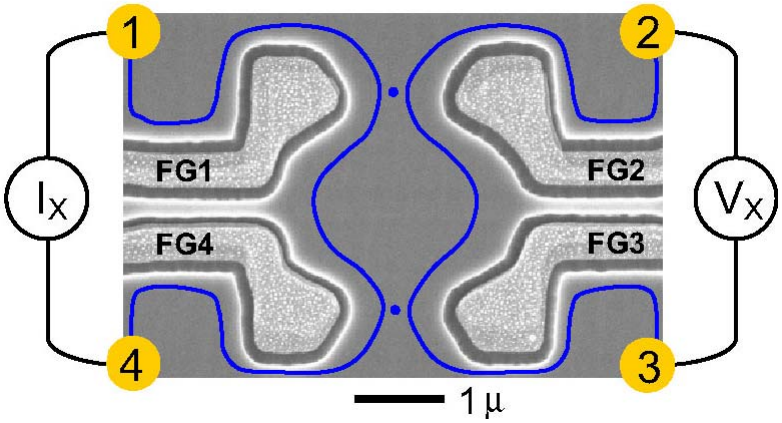

Figure 3.3: Schematic diagram of a four-terminal resistance measurement. $R_{XX} = V_X / I_X$ is measured with $5.4\,\text{Hz}$ AC current injected at contacts 1 and 4 and the resulting voltage V_X, including the Aharonov-Bohm oscillatory signal, is detected at contacts 2 and 3. The Hall resistance R_{XY} is measured with current injected at contacts 1 and 3 and the resulting voltage V_Y, is detected at contacts 2 and 4.

3.3 Edge Network Model

The sample contains two domains with different filling factors, ν_B in the bulk and ν_C in the constriction. Because, in an applied magnetic field B, the Landau-level filling factor $\nu = hn/eB$ is proportional to the local electron density n, in the depleted regions of the sample, ν_C is smaller than ν_B. The plateaus appearing in the measurement R_{XX} and R_{XY} allow us to determine both the bulk (ν_B) and the constriction filling factor (ν_C). The calculation is based on the edge network model,[45] as illustrated in Figure 3.4.

We use I_j to denote the edge current on the $j-$th edge; and the corresponding chemical potential is symbolized by μ_j. The edge currents I_j are related to the chemical potentials μ_j by a thermodynamical relation:

$$I_j = \Delta\nu_j \mu_j \frac{e}{h}, \tag{3.1}$$

where $\Delta\nu_j$ is the difference of the filling factors on the two sides of the $j-$th edge.

Four Ohmic contacts are labeled by circled numbers. The chemical potentials in four Ohmic contacts are labeled μ_1 to μ_4. Contacts 2 and 3 are the ideal voltage probes that draw no current, therefore,

$$I_1 = I_2, \tag{3.2}$$

$$I_3 = I_8, \tag{3.3}$$

and contacts 1 and 4 are the current probes with current I_X.

$$I_X = I_4 - I_3 = I_6 - I_1. \tag{3.4}$$

Since 1D chiral edge channels follow an equipotential, the chemical potential remains unchanged when the edge current passes through a branch point dividing into two branches. Therefore, as shown in Figure 3.4, we get:

$$\mu_2 = \mu_7 = \mu_{10}, \tag{3.5}$$

$$\mu_4 = \mu_5 = \mu_9. \tag{3.6}$$

According to Kirchhoff's junction law, the current is conserved as it passes through a branch point; therefore, we get the following relations,

$$I_9 = I_4 - I_5 = I_8 - I_7, \tag{3.7}$$

$$I_{10} = I_2 - I_7 = I_6 - I_5. \tag{3.8}$$

Since the chemical potentials μ_j is related to the edge voltages V_j in the form as $\mu_j = eV_j$; to determine the voltages on different edges, first we find out the chemical potentials on each edge. According to equation (3.1), we write down the equations for the system as following, setting $e \equiv h \equiv 1$,

$$I_1 = \nu_B \mu_1 \tag{3.9}$$

$$I_2 = \nu_B \mu_2 \tag{3.10}$$

$$I_3 = \nu_B \mu_3 \tag{3.11}$$

$$I_4 = \nu_B \mu_4 \tag{3.12}$$

$$I_5 = \nu_C \mu_4 \tag{3.13}$$

$$I_6 = \nu_B \mu_6 \tag{3.14}$$

$$I_7 = \nu_C \mu_2 \tag{3.15}$$

$$I_8 = \nu_B \mu_8 \tag{3.16}$$

$$I_9 = (\nu_B - \nu_C)\mu_4 \tag{3.17}$$

$$I_{10} = (\nu_B - \nu_C)\mu_2 \tag{3.18}$$

In our experiments, the voltages are detected through contacts 2 and 3 for R_{XX}, and through 2 and 4 for R_{XY}, therefore, the important quantities we care about is $\mu_3 - \mu_2$ and $\mu_4 - \mu_2$. We take the following steps to figure out them.

First, considering equations (3.3), (3.4) and (3.7), we find,

$$I_5 - I_7 = I_4 - I_8 = I_X, \tag{3.19}$$

Subtracting equation (3.12) from (3.11), and substituted with (3,19), it gives,

$$\mu_4 - \mu_2 = \frac{I_X}{\nu_C}, \tag{3.20}$$

From equations (3.11) and (3.12), we get,

$$I_X = I_4 - I_3 = \nu_B(\mu_4 - \mu_3), \tag{3.21}$$

Therefore, we obtain

$$\mu_4 - \mu_3 = \frac{I_X}{\nu_B}, \tag{3.22}$$

Now, $(\mu_4 - \mu_2) - (\mu_4 - \mu_3)$ gives us the value $\mu_3 - \mu_2$, expressed as

$$\mu_3 - \mu_2 = I_X(\frac{1}{\nu_C} - \frac{1}{\nu_B}). \tag{3.23}$$

In our experiments, voltage for R_{XX} is measured through contacts 3 and 2, and voltage for R_{XX} is measured through contacts 4 and 2. From above discussion, we get:

$$R_{XX} = \frac{V_{3-2}}{I_X} = \frac{h}{e^2}(\frac{1}{\nu_C} - \frac{1}{\nu_B}) \tag{3.24}$$

$$R_{XY} = \frac{V_{4-2}}{I_X} = \frac{h}{e^2}\frac{1}{\nu_C} \tag{3.25}$$

Therefore, the plateaus appearing in the measurement R_{XX} and R_{XY} allow us to identify both the bulk (ν_B) and the constriction filling factor (ν_C) uniquely.

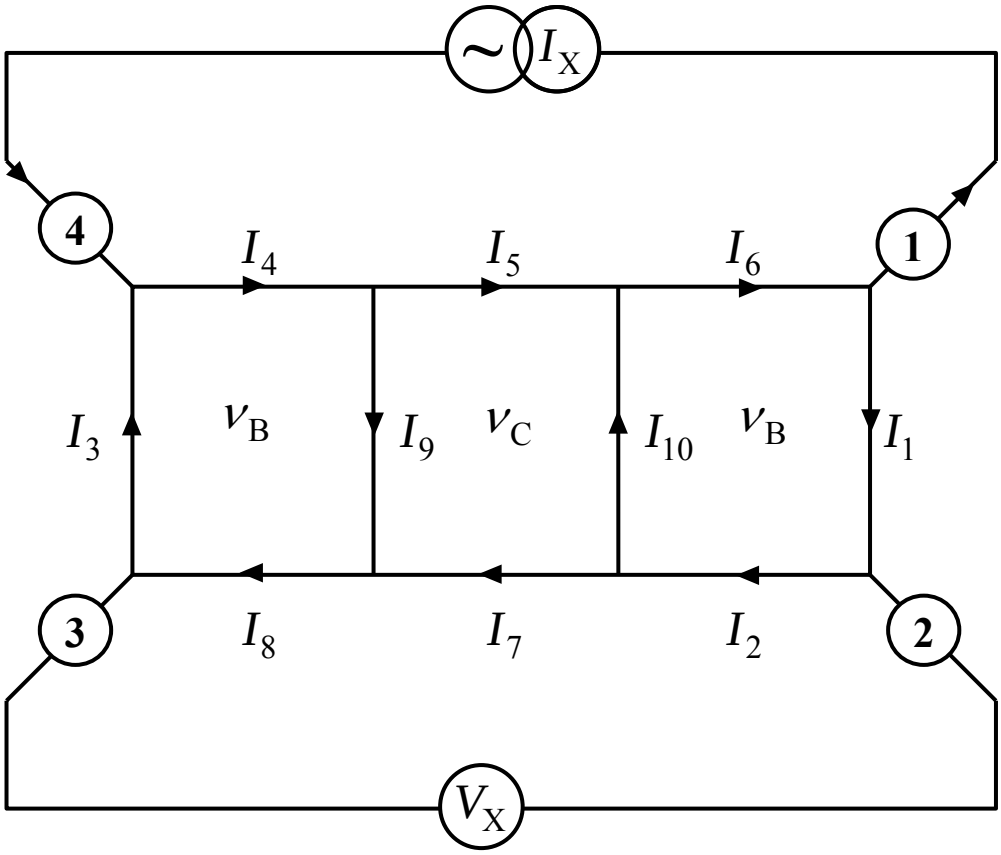

Figure 3.4: Quantum Hall sample containing two different filling factors: the bulk filling factor is ν_B and the constriction filling factor is ν_C ($\nu_B > \nu_C$). Circled numbers denote the Ohmic contacts. The four Ohmic contacts have chemical potentials μ_1 to μ_4. μ_2 and μ_3 are the ideal voltage probes that draw no current, and μ_1 and μ_4 are the current probes with current I_X. The current in the edge channels are labeled I_j, and the current directions are indicated by arrows.

Chapter 4

Quantum Magnetotransport at Low Fields[1]

We report systematic quantum Hall transport experiments on Fabry-Perot electron interferometers at ultralow temperatures. A systematic variation of the front-gate voltage affects the constriction and the island electron density, while the bulk density remains unaffected. This results in quantized plateaus in longitudinal resistance, while the Hall resistance is dominated by the low-density, low-filling constriction. At lower fields, when the quantum Hall plateaus fail to develop, we observe bulk Shubnikov-de Haas oscillations in series corresponding to an integer filling of the magnetoelectric subbands in the constrictions. This shows that the whole interferometer region is still quantum coherent at these lower fields at $10\,\mathrm{mK}$. Analyzing the data within a Fock-Darwin model, we obtain the constriction electron density as a function of the front-gate bias and, extrapolating to the zero field, the number of electric subbands (conductance channels) resulting from the electron confinement in the constrictions.

[1] Published in P. V. Lin, F. E. Camino, and V. J. Goldman, Phys. Rev. B **78**, 245322 (2008).

4.1 Motivation

There has been a continuing wealth of research into the ground state and transport properties of confined two-dimensional (2D) electron systems ever since the discovery of the integer quantum Hall effect[1] (IQHE) and the development of lithographic techniques. The IQHE can be understood in terms of transport by one-dimensional (1D) chiral edge channels corresponding to an integer number of fully occupied Landau levels.[3-4, 32] In this picture, near an integer Landau level filling $\nu \approx f$, when the chemical potential lies in the gap of localized bulk states, the current is carried by dissipationless edge channels and the Hall resistance is quantized exactly to h/fe^2. Dissipative transport occurs when current is carried by the extended bulk states of the partially occupied topmost Landau level, between the plateaus. Such interpretation of the IQHE of non-interacting electrons in terms of edge channels is straightforward since for non-interacting electrons the edge channels are formed in one-to-one correspondence with the bulk Landau levels. Including effects of electron interaction is not so straightforward, but, qualitatively, the concept of current-carrying chiral edge channels is till applicable.[45-50]

In a constricted geometry, even in zero magnetic field $B = 0$, an approximate quantization of conductance[51-52] is understood as resulting from size-quantized nonchiral 1D conducting channels passing through the constriction.[53] In a quantized B, the size-quantized and the chiral edge channels hybridize, there exists a transitional regime where both effects co-exist, and the plateau positions in B depend on both size and Landau quantization. Here, the noninteracting electron theory does not provide quantitatively accurate description so that effects of interaction resulting in a self-consistent confining potential have to be included. In addition, in such constrictions, "backscattering" by quantum tunneling between the extended states is possible and leads to a deviation from exact plateau quantization.

In this chapter we present a comprehensive experimental characterization of quantum Hall (QH) and Shubnikov-de Haas (SdH) transport in an electron Fabry-Perot

interferometer.[19, 29, 54] The constrictions are wide: we obtain the zero $-B$ number of conduction channels between 10 and ~ 500. Similar electron interferometer devices have been studied by others in the integer QH regime.[40, 55-56] Earlier studies of dependence of constriction electron density were done in single unetched quantum point contacts defined by the split-gate technique, where the number of conductance channels was varied between zero (pinch-off) to a dozen.[51-53] Indeed, one reason why no similar work was feasible earlier is that in our device, the main depletion is provided by etching so that the constriction density can be varied in a wide range while maintaining the deice geometry. In the front-gate-only device of Ref. 40, changing gate voltage appreciable either opens or closed the constrictions completely so that the intended device geometry is lost.

Our experiments on the interferometers in the low-field integer QH regime presented here are moreover motivated by application of such devices in the fractional QH regime, where interference of fractionally charged Laughlin quasiparticles has been reported.[18, 20, 28, 30-31, 57] Additional motivation is provided by proposed application of such Fabry-Perot interferometers, in conjunction with quantum antidots,[14] to detection of non-Abelian braiding statistics and as a physical implementation of topological quantum computation.[25, 58-60]

4.2 Devices and Measurement Techniques

The interferometer sample was fabricated from a very low disorder double-δ-doped GaAs/AlGaAs heterostructure.[61] The 2D electron system is buried 320 nm below the surface. First, Ohmic contacts are formed on a pre-etched mesa. Then etch trenches are defined by electron-beam lithography, using proximity correction software for better definition of narrow and low gaps between the exposed area. After a shallow 160 nm wet etch, 50 nm thick Au/Ti front-gate (FG) metallization is deposited in a self-aligned process. Finally, samples are mounted on sapphire substrates with In metal, which serves as the global back gate. The interferometer sample studied in this paper is the same as in Ref. 30, but on a subsequent cool-down and under different illumination.

Samples were cooled in the tail of the mixing chamber of a top-loading into mixture dilution ^{3}He-^{4}He refrigerator. A bulk 2D electron density $n_B = 1.16 \times 10^{11}\,\mathrm{cm}^{-2}$ was achieved after illumination by a red light emitting diode (LED) at $4.2\,\mathrm{K}$. All experiments reported in this work were performed at the fixed bath temperature of $10\,\mathrm{mK}$, calibrated by nuclear orientation thermometry. Extensive cold filtering in the electrical leads attenuates the electromagnetic background "noise" incident on a sample, allowing to achieve effective electron temperatures of $\leq 15\,\mathrm{mK}$.[28] Four-terminal longitudinal $R_{XX} = V_X / I_X$ and Hall $R_{XY} = V_Y / I_X$ magnetoresistances, see Figure 4.1, were measured with a lock-in technique at $5.4\,\mathrm{Hz}$. The excitation current was set so as to keep the larger, Hall or longitudinal voltage $\leq 5\,\mu\mathrm{V}$.

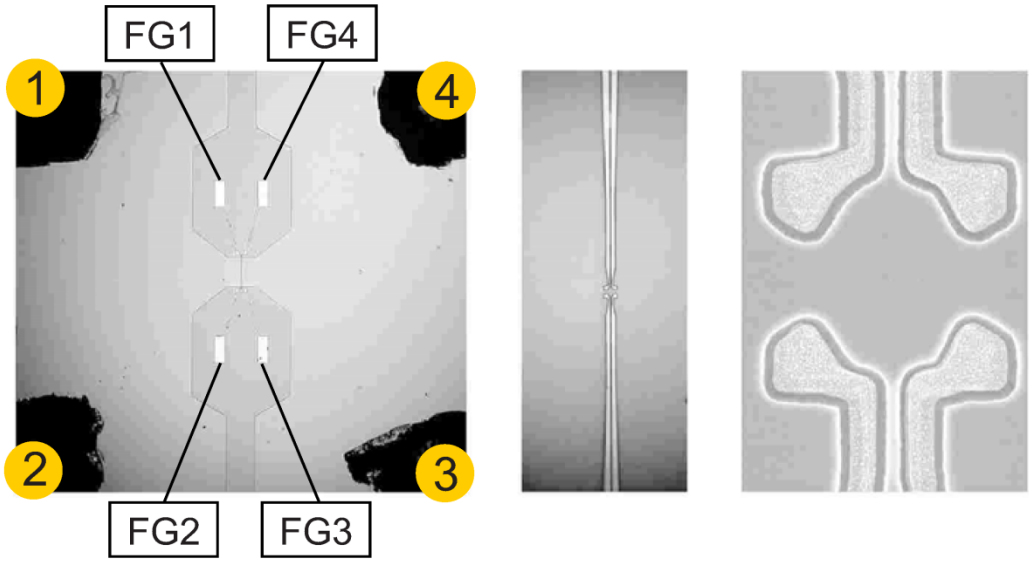

Figure 4.1: A Fabry-Perot electron interferometer device. Optical (two left) and scanning electron (SEM, right) micrographs of the interferometer sample. Numbered circles on the four corners of the 4×4 mm mesa show Ohmic contacts to 2D bulk electron layer. Four front gates (FG1−4) are deposited in shallow etch trenches, defining a circular island separated from the 2D bulk by two 1.2 μm wide constrictions. In a quantizing magnetic field, chiral edge channels follow an equipotential at the periphery of the undepleted 2D electrons. Longitudinal R_{XX} (current 1−4, voltage 2−3) and Hall R_{XY} (current 1−3, voltage 2−4) resistances are measured. The back gate (not shown) extends over the entire sample.

4.3 Magnetotransport

Figure 4.2 − Figure 4.4 summarize experimental longitudinal and Hall four-terminal magnetoresistance in sample M97Ce, the same as reported in Ref. 30, but under different illumination, taken in a range of front-gate voltage $-580\,\mathrm{mV} \le V_{\mathrm{FG}} \le +100\,\mathrm{mV}$. Even at zero front-gate $V_{\mathrm{FG}} = 0$, the GaAs surface depletion of the etch trenches, which remove the doping layer, creates electron confining potential, so that the constriction and the island electron densities are less than the 2D "bulk". Application of a negative V_{FG} depletes the constrictions-island region of the sample further. The two constrictions were tuned for approximate symmetry by application of a constant $\pm 20\,\mathrm{mV}$ differential bias between FG1 and FG4, additional to the common front-gate bias given in this paper as V_{FG}. Detuning front-gate voltage from symmetry allows us to verify each constriction filling separately.

Because in a uniform applied B the Landau filling factor $\nu = hn/eB$ is proportional to the local electron density, ν in the depleted region of the sample is different from the 2D bulk ν_{B}. While $\nu \propto n/B$ is a variable, the quantum Hall exact filling f is a quantum number defined by the quantized Hall resistance as $f = h/e^2 R_{\mathrm{XY}}$. Because QH plateaus have finite width, regions with different ν may have the same f. In samples with lithographic constrictions, in general, there are two possibilities: (i) when depletion is small and on a wide QH plateau, the whole sample may have the same QH filling f ; and (ii) more often, the constriction filling f_{C} and the bulk filling f_{B} are different. As can be seen in Figure 4.2, as the front gates are biased more negative, there is a continuous series of well-developed constriction QH plateaus for each f_{C}, shifting to lower magnetic fields, and thus to higher f_{B} plateaus.

The Hall resistance R_{XY} allows us to determine the filling in the constrictions, the plateau positions in B giving definitive values of f_{C}. The longitudinal R_{XX} shows

quantum Hall minima and quantized plateaus at $R_{XX} = (h/e^2)(1/f_C - 1/f_B)$ when plateaus in constrictions and the bulk overlap in B.[62] Note the special case: when $f_C = f_B$, $R_{XX} = 0$. Thus, a quantized plateau in $R_{XX}(B)$ implies quantum plateaus for both the constriction region and the bulk, and a set of quantized $R_{XX}(B)$ plateaus provides definitive values for both f_C and f_B. Evolution of several stronger QH constriction and bulk plateaus as a function of V_{FG} is indicated in Figure 4.3. As expected, the constriction plateaus are shifted to lower magnetic fields by a negative front-gate voltage, while the bulk plateaus are not affected.

Figure 4.4 shows detail of the magnetotransport data in the range of B where SdH oscillations in the bulk occur, transitioning to the developing QH plateaus. As seen in the raw data, SdH oscillations are not shifted in B by front-gate bias; this is confirmed by Fourier analysis, which gives a V_{FG} -independent SdH oscillation frequency corresponding to the bulk density. The vertical positions of the bulk SdH oscillations are grouped in series corresponding to the number of conduction channels passing through the constriction. This shows as a constant resistance plateau in Hall data, and a $(h/e^2)(1/f_C - 1/f_B)$ background, the bulk Hall effect when f_C is constant, in the R_{XX} data. The values of the Hall plateaus and the $B = 0$ intercept of the negative slope R_{XX} background are both $h/f_C e^2$, which can be used to ascertain the channel number of the constriction series.

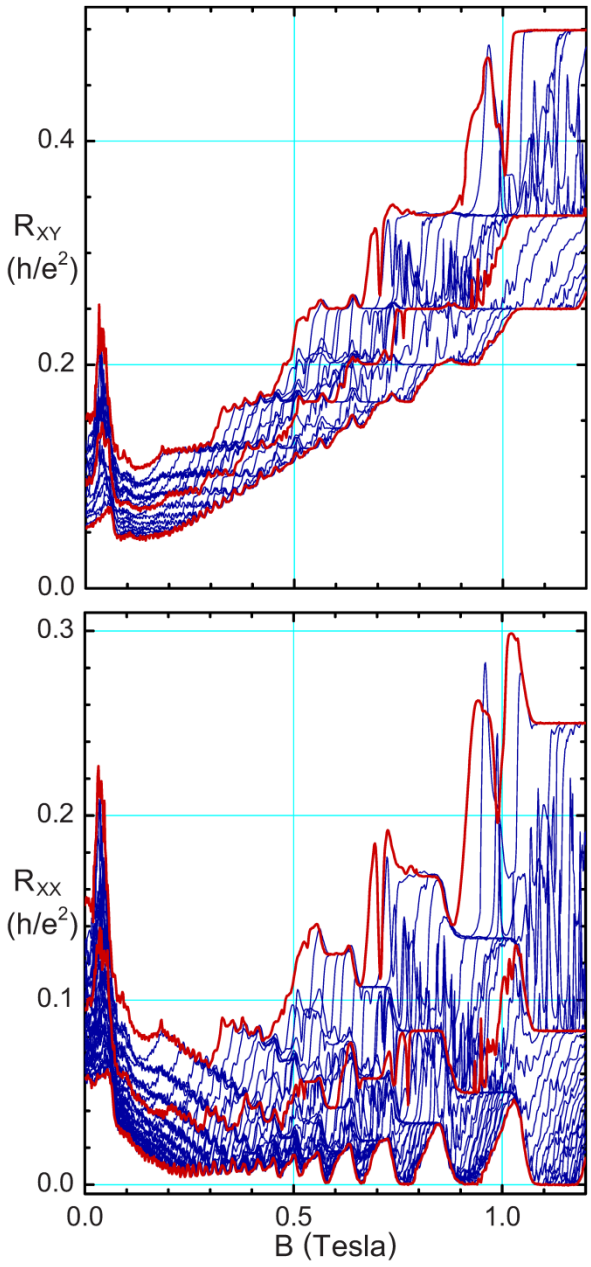

Figure 4.2: Representative longitudinal (R_{XX}) and Hall (R_{XY}) magnetoresistance traces of the interferometer sample. The front-gate voltage is stepped by multiples of 20 mV in the range $-580\,\text{mV} \le V_{FG} \le +100\,\text{mV}$. The zero resistance level is the same for all traces. Application of V_{FG} changes the electron density in the interferometer region, both the island and the constrictions, thus shifting the B positions of the quantized plateaus. The smallest filling factor, which in constrictions, determines the Hall signal (R_{XY}), while the longitudinal signal (R_{XX}) depends on filling in all regions of the sample, including the 2D bulk.

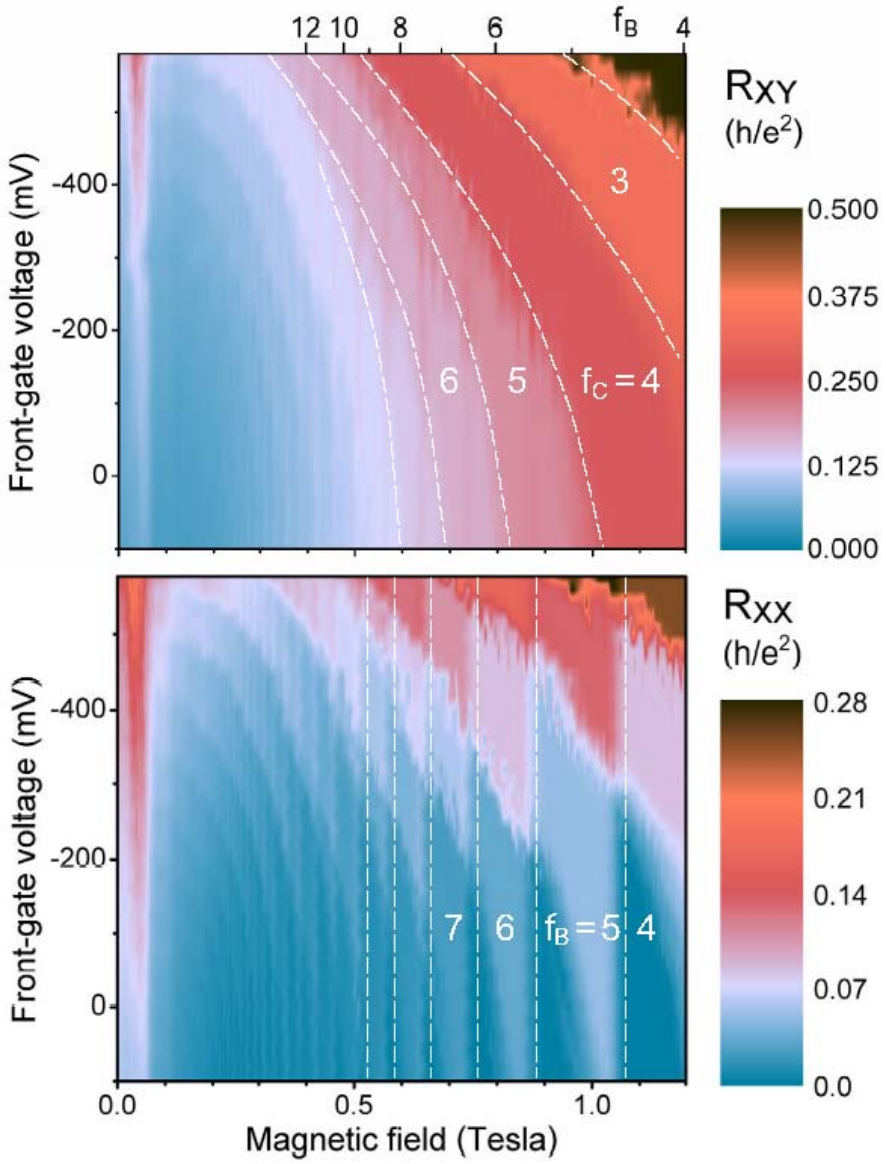

Figure 4.3: Color-mapped plot of the magnetoresistance data of Figure 4.2. The Hall R_{XY} and longitudinal R_{XX} plateau regions correspond to the same shade. Note that the constriction plateaus are shifted to lower magnetic fields by a negative front-gate voltage, while the bulk plateaus are not affected. The absolute resistance values of the R_{XX} plateaus allow us to determine both constriction and bulk fillings as a function of magnetic field, as shown. The dashed white lines give approximate boundaries between consecutive QH plateaus.

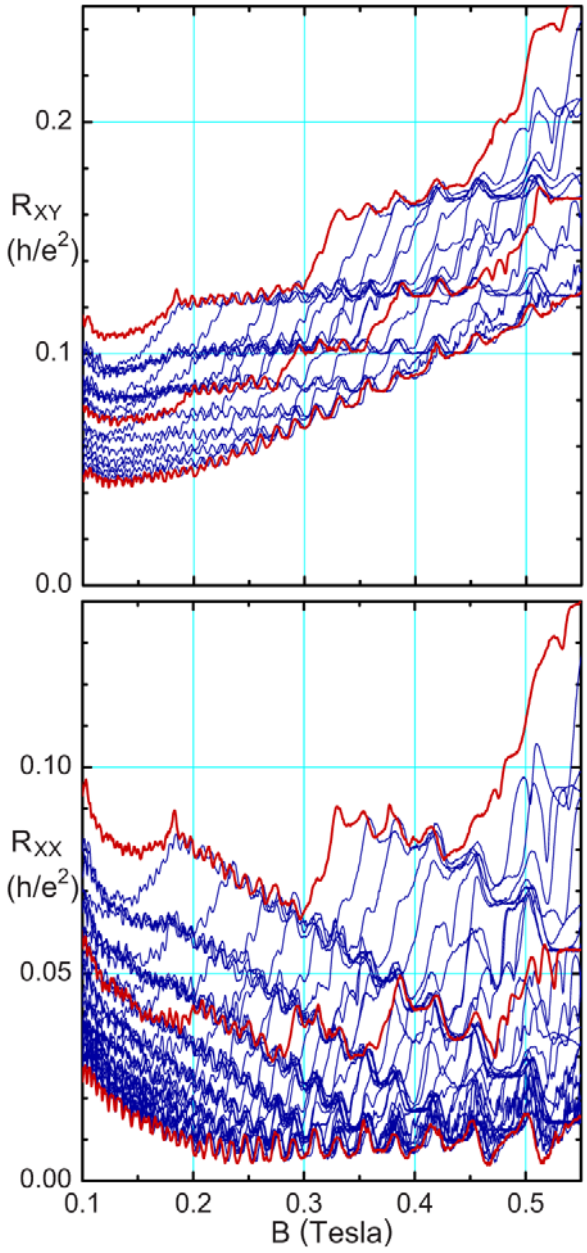

Figure 4.4: Blow-up of the magnetoresistance data of Figure 4.2 in the region of Shubnikov-de Haas oscillations and developing quantum Hall plateaus in the bulk. Some traces are shown in thicker red lines to help distinguish individual traces. The lowest trace corresponds to the positive bias +100 mV, the middle is at −360 mV, and the top (lower electron density) is at −580 mV. Note that the B positions of the bulk SdH oscillations are not affected by V_{FG}, while superimposed on resistance background determined by the number of the conduction channels in the constrictions, which is shifted by V_{FG}. This allows us to separate the bulk and constriction features. The zero resistance level is the same for all traces.

It is not surprising that the QH edge channels pass through both constrictions. As can be seen in Figure 4.4, there is a smooth, continuous transition from well-developed QH constriction plateaus to the low-field magnetoelectric conduction channel regime for each f_C series formed by various V_{FG} traces. This means that the whole interferometer region, including both constrictions, is quantum-coherent even at $0.1\mathrm{T}$, and most likely, indeed, even at $B = 0$. If the two constrictions were not quantum-coherent, their individual resistances would add, which would be seen as an apparent doubling of the constriction channel number as B is lowered.

Because a four-terminal R_{XY} generally contains longitudinal contributions, it may not be clear-cut as to what is the true Hall effect. We can ascertain the assignment of various features to the bulk or to the constriction by the following two techniques. First, we can reverse the direction of the magnetic field, that is, take the corresponding magnetoresistance data at both $B+$, up, and $B-$, down, (shown in Figure 4.5). The $R_{XY}(B-)$ data is multiplied by -1, both the magnetic field and resistance. According to Onsager relations for a magnetoconductivity tensor in an inversion-symmetric sample,[63] the Hall contribution changes sign, while the diagonal contributions remain unaffected. Thus, the average Hall $\frac{1}{2}[R_{XY}(B+) + R_{XY}(B-)]$ corresponds to the true bulk Hall effect, with all longitudinal contributions to resistance, including the effect of constrictions, removed (within the experimental accuracy). The thin solid line in Figure 4.5 gives the classical Hall slope corresponding to the bulk density $n_B = 1.16 \times 10^{11} cm^{-2}$, obtained from the B positions of the V_{FG}-independent QH plateaus in Figure 4.2 and Figure 4.3; as can be seen, it matches the $B+$, $B-$ average slope well. The difference $\frac{1}{2}[R_{XY}(B+) - R_{XY}(B-)]$ has no Hall contribution, and closely follows the raw R_{XX} data at the same front-gate voltage. Such analysis for the low-filling fractional QH regime has been reported in Ref. 64.

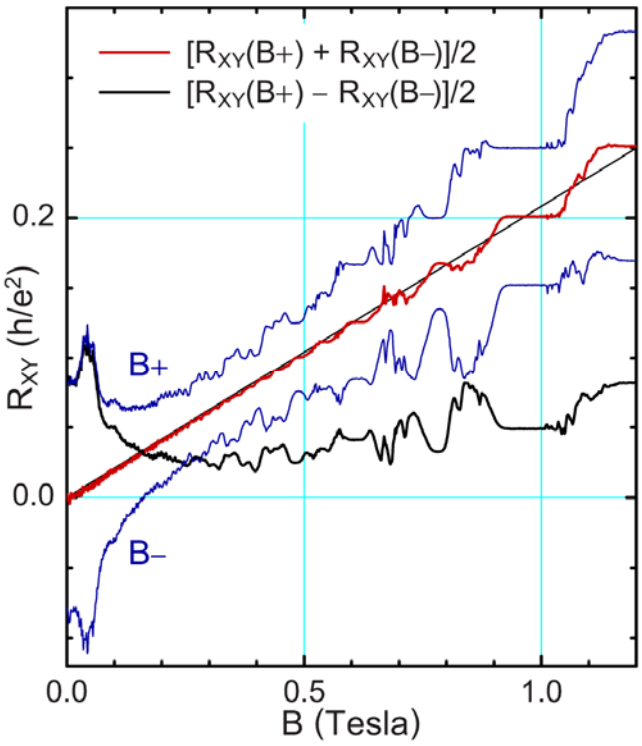

Figure 4.5: Experimental four-terminal Hall R_{XY} also contain longitudinal contribution. The two directly measured traces shown (thin blue lines) are obtained with magnetic field up ($B+$) and down ($B-$). The $R_{XY}(B)$ trace is shown multiplied by -1, both horizontal and vertical axes. The middle trace (thick red line) is the average $\frac{1}{2}[R_{XY}(B+)+R_{XY}(B-)]$, which, according to Onsager relations, gives the true bulk R_{XY} (straight thin line gives the bulk density). Likewise, the difference $\frac{1}{2}[R_{XY}(B+)-R_{XY}(B-)]$ gives the longitudinal R_{XX}, which displays the quantized plateaus, e.g., $R_{XX} = 0.05h/e^2$ ($f_C = 4$, $f_B = 5$) at $B \approx 0.98\,\mathrm{T}$. Data taken at $V_{FG} = -260\,\mathrm{mV}$.

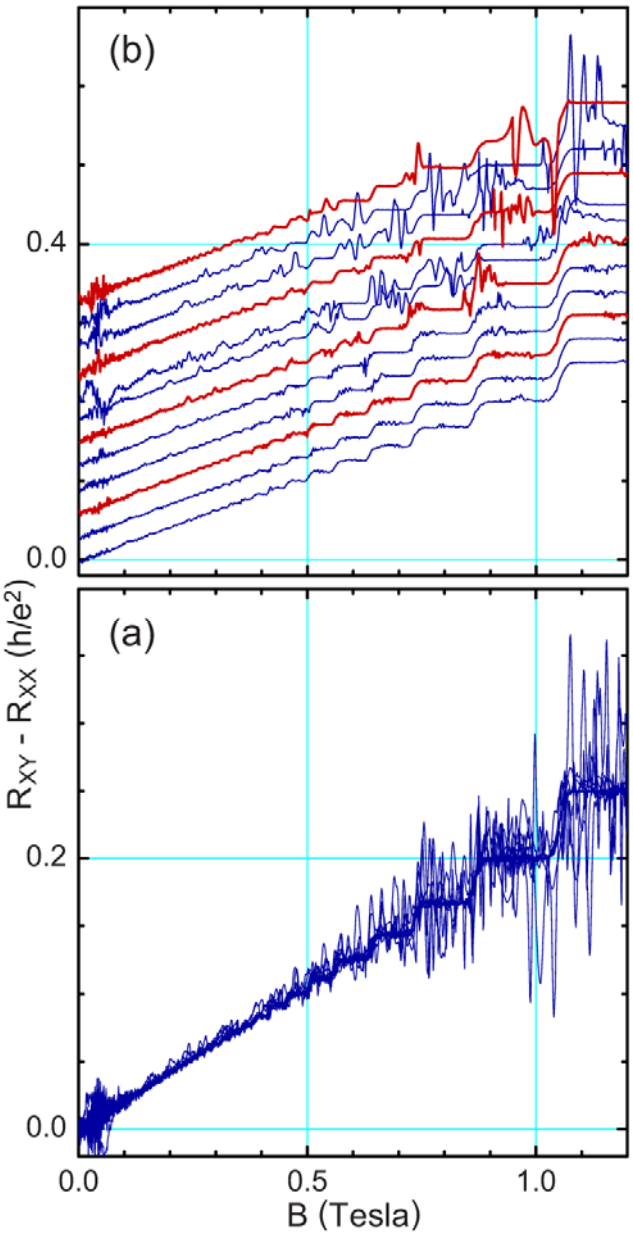

Figure 4.6: Representative traces illustrating subtraction of experimental Hall and longitudinal magnetoresistance at the same front-gate voltage. The lower panel shows the difference traces at various V_{FG}, all having true zero level. The subtraction results in the bulk Hall resistance (darker central region), with superimposed features due to mesoscopic effects and tunneling in the constrictions, different in each individual V_{FG} traces. The upper panel shows several individual V_{FG} traces shifted vertically by $0.01h/e^2$ per $-20\,\mathrm{mV}$ of V_{FG}.

The second technique is approximate; it is exact in certain bulk-edge network models of QH transport,[44, 65-67] and is also an approximate semiclassical result in the limit of $\sigma_{XX} << \sigma_{XY}$ in 2D samples.[68] For each V_{FG} in Figure 4.2, we subtract longitudinal from the Hall magnetoresistance, $R_{XY}(B) - R_{XX}(B)$, both for $B+$. When both constriction and bulk are on a QH plateau, it is apparent that the difference is $h / f_B e^2$, the bulk Hall effect. However, this technique also subtracts the finite σ_{XX} contributions between the plateaus, present both in R_{XY} and R_{XX} (as shown in Figure 4.6).

The fine structure in the traces of Figure 4.2 − Figure 4.6 is attributed to disorder-assisted tunneling and quantum interference effects. It is particularly visible in the difference data of Figure 4.6 (more negative V_{FG}), since the individual R_{XY} and R_{XX} traces for the same V_{FG} were taken several days apart, so that the detailed B-positions and magnitude of the "mesoscopic features" do not match, and thus do not subtract, due to their slow drift as a function of time. Aharonov-Bohm oscillations,[19, 29, 40, 53, 55] present in some data, have small amplitude ($\leq 4 \times 10^{-3} h/e^2$) and are not visible on the scale of Figure 4.2−Figure 4.6.

4.4 Constriction Electron Density

The $B = 0$, $V_{FG} = 0$ shape of the electron density profile resulting from etch trench depletion in the interferometer region of the sample is illustrated in Figure 4.7. The interferometer island is large, contains $2 - 4 \times 10^3$ electrons, and the 2D electron density profile is determined mostly by the classical electrostatics, minimizing the energy of the electron-electron repulsion, compensated by attraction to the positively charged donors. The Fabry-Perot device depletion potential has saddle points in the constrictions, and so has the resulting electron density profile. In a quantizing magnetic field edge channels form, but the overall electron density profile closely follows the $B = 0$ profile in these relatively large devices, so as to minimized total Coulomb energy.

Because the in-plane screening by 2D electrons is relatively weak, [46-47, 50] application of a negative front-gate voltage V_{FG} decreases electron density throughout the interferometer region. The main depletion is provided by the etch trenches; modeling[19, 29, 31] shows that application of a moderate V_{FG}, besides the overall depletion, increases effective depletion length by $\sim 100\,\mathrm{nm/V}$. Changing magnetic field affects the equilibrium electron density profile in the device only weakly, particularly for $f \geq 4$, the principal effect is to redistribute the electron occupation between various Landau levels. In a fixed B, when the density of states in each Landau level in a given area is fixed also, application of V_{FG} changes occupation of these states.

We model the constriction following the Fock-Darwin model[69-71] for non-interacting electrons as a 1D conductor with a parabolic confining potential with energy level (1D subbands) spacing $\hbar\omega_0$. The Hamiltonian for an electron is thus given by:

$$H = \frac{1}{2m^*}\left[\mathbf{p} + e\mathbf{A}(\mathbf{r})\right]^2 + U(y), \tag{4.1}$$

$$U(y) = \frac{1}{2} m\omega_0^2 y^2 . \tag{4.2}$$

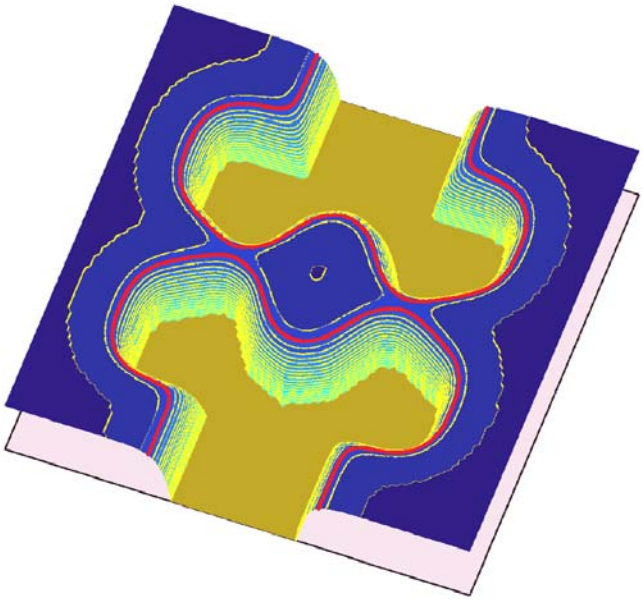

Figure 4.7: Illustration of the 2D electron density profile. Four front gates are deposited in shallow etch trenches. Depletion potential of the trenches defines the electron island. The chiral edge channels follow equipotentials at the periphery of the undepleted 2D electrons. Tunneling occurs at the saddle points in the two constrictions. The edge channel path is closed by the tunneling links, thus forming the interferometer. The back gate (not shown) extends over the entire sample. (duplicated from Fig. 1 of Ref. 30, with permission)

In a quantizing magnetic field with cyclotron energy $\hbar\omega_C$, hybrid magnetoelectric subbands with bottom at energy

$$E_n = (n+\frac{1}{2})\sqrt{(\hbar\omega_0)^2+(\hbar\omega_C)^2} \tag{4.3}$$

where $n = 0,1,2,...$, serve as conduction channels. In GaAs, spin splitting of the subbands is small compared with $\hbar\omega_C$, and develops only at higher magnetic fields. As $\hbar\omega_C \propto B$ is increased from zero, these magnetoelectric subbands cross the chemical potential, become de-populated, and so the number of the constriction conduction channels decreases. We use the experimental number of constriction conduction channels, taken as f_C from the corresponding constriction plateau position (the exact filling $\nu = f$) in the magnetoresistance data in Figure 4.2, shown as circles in Figure 4.8 (a). Both $R_{XX}(B)$ and $R_{XX}(B)$ data sets yield consistent constriction plateau positions; the horizontal error bar represent the uncertainty in the $B-$position of the centers of the plateaus.

The number of states in each hybrid magnetoelectric subband per unit aera, $D(E)$, is express as:

$$D(E) = m^*(\omega_C^2+\omega_0^2)^{1/2}/h. \tag{4.4}$$

The electron density n is related to the number of occupied hybrid magnetoelectric subbands f as:

$$n = f\cdot D(E) = f\cdot m^*(\omega_C^2+\omega_0^2)^{1/2}/h \tag{4.5}$$

For convenience, we introduce two parameters, B_1 and f_0, which are define as:

$$B_1 = n\cdot h/e, \tag{4.6}$$

$$f_0 = \frac{eB_1}{m^*\omega_0}. \tag{4.7}$$

Therefore, each set of channel number $\{f, B_f\}$ points, corresponding to a particular V_{FG}, is fitted with

$$f = f_0/\sqrt{1+(f_0 B_f/B_1)^2} \tag{4.8}$$

where f_0 is the conduction channel number at $B=0$, and B_1 is the $f=1$ plateau center, both refer to constriction. Figure 4.8 shows the $\{f, B_f\}$ point set and the fit for data taken

at $V_{FG} = -500\,\mathrm{mV}$. Figure 4.9 summarizes the fits performed for the data for V_{FG} stepped typically by 60 mV; they yield f_0 as the best fit parameter, plotted in Figure 4.10. One $f_0 = 582 \pm 300$ for $V_{FG} = +100\,\mathrm{mV}$ is not shown in Figure 4.10. The value $f_0 \sim 100$ at zero front-gate bias is consistent with the four-terminal sample resistance of $\sim 300\,\Omega$ at $1.2\,\mathrm{K}$. (At mK temperature, the $B = 0$ sample resistance is higher, $\sim 1.2\,\mathrm{k}\Omega$, as can be seen in Figure 4.2, likely due to quantum interference effects in the device). The absolute error in f_0 is, unsurprisingly, large for nearly open constriction, when the constriction density is only slightly less than n_B .

The second fit parameter, B_1 , gives information on constriction density, $n_C = eB_1 / h$ at $\nu_C = 1$. Thus obtained constriction density is plotted as a function of V_{FG} in Figure 4.11. Since n_C is derived from the QH transport data, it should correspond to the electron density near the saddle point in the constriction, which determines the constriction QH filling. We also have determined the constriction density as $n_C = \nu eB / h$, from the raw transport data Hall slope (crossed in Figure 4.11). The classical Hall line is forced through zero at $B = 0$, which results in a systematically larger Hall slope, and so underestimate n_C . Roughly, this procedure is equivalent to the Fock-Darwin analysis described above, but setting $f_0 \to \infty$ in Equation (4.8).

Within the Fock-Darwin model, that is, assuming parabolic constriction confinement potential and neglecting electron interaction, we can also estimate the constriction width[72-73] at chemical potential as $W \approx \pi f_0 / 2k_F \approx f_0 / \sqrt{\pi / 8n_C}$. The resulting width varies in the range $280\,\mathrm{nm} \le W \le 11000\,\mathrm{nm}$ in the experimental range of V_{FG} . The lower value of W is still larger than the tunneling distance of $100\,\mathrm{nm}$, estimated from the amplitude of Aharonov-Bohm oscillations.[18, 20] The larger value, $11\,\mu\mathrm{m}$, is much larger than the lithographic constriction width of $1.2\,\mu\mathrm{m}$, and thus is not realistic. Both assumptions of the model are not realistic, and it is remarkable that some values obtained, such as f_0 and n_C are reasonable, while others, such as W , are not.

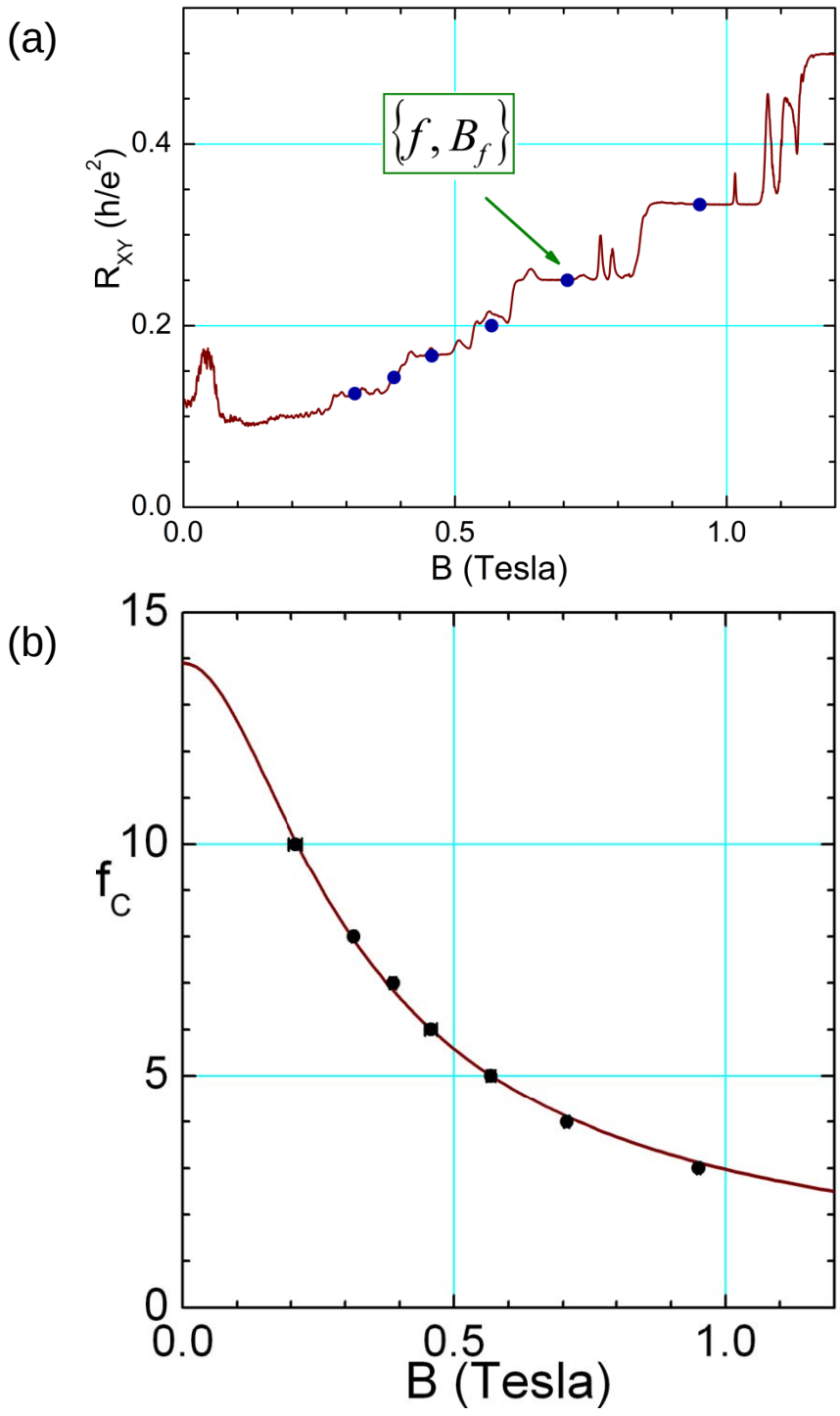

Figure 4.8: (a) Positions of the constriction plateaus from the R_{XX} data corresponding to $V_{FG} = -500\,\text{mV}$ (blue circles). (b) The fit to the 1D Fock-Darwin model (red line) for data at $V_{FG} = -500\,\text{mV}$.

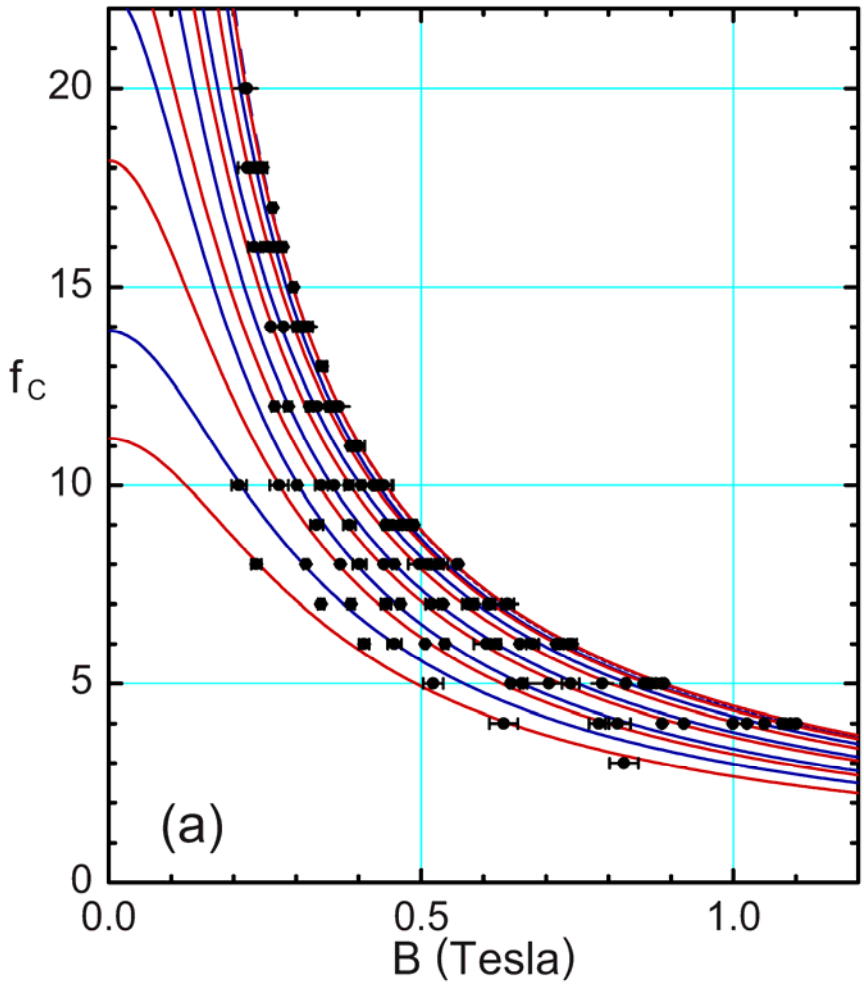

Figure 4.9: Positions of the constriction plateaus from the data of Figure 4.2 (circles with horizontal error bars) and the fits to the 1D Fock-Darwin model (lines). Each set of points and the fit correspond to a particular V_{FG} .

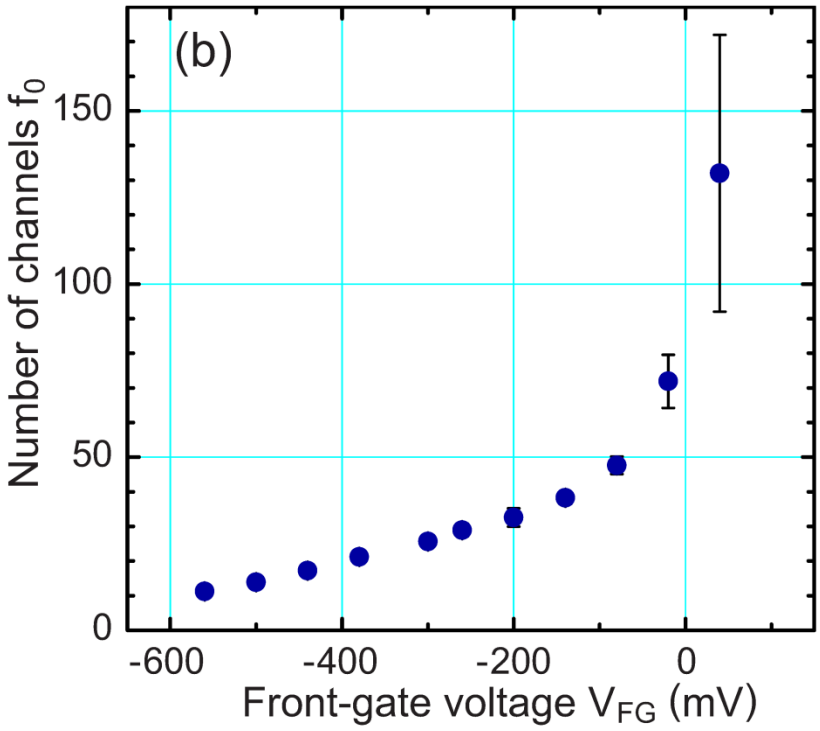

Figure 4.10: Zero-field number of conduction channels in the constriction obtained from the fits shown in Figure 4.9.

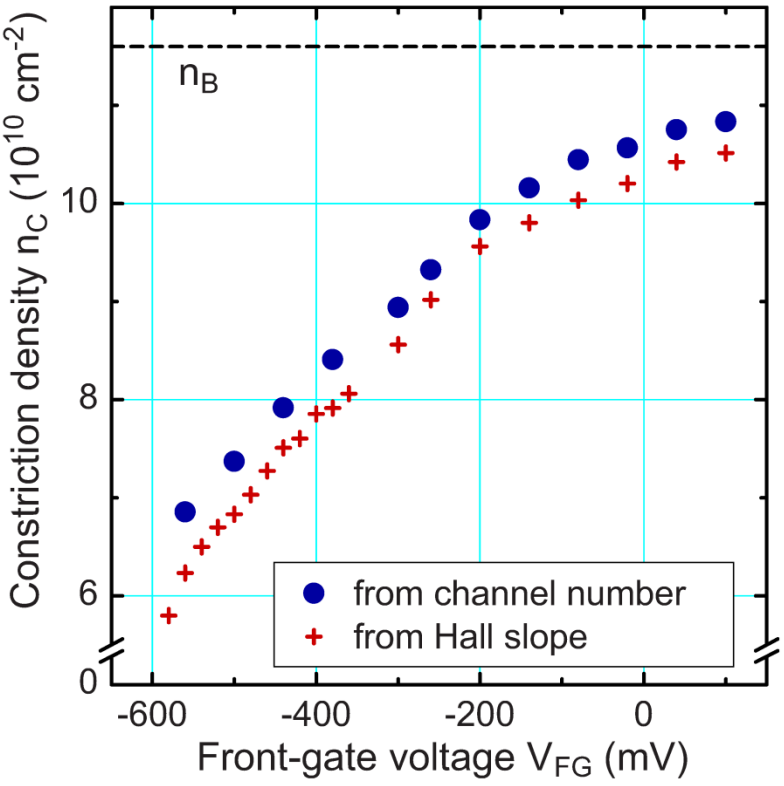

Figure 4.11: Constriction electron density obtained from the conduction channel number analysis, Equation (4.8), in Figure 4.9 (circles). Also shown is n_C obtained by conventional Hall slop (forced through zero) analysis (crossed). This neglects confinement in the constriction, and thus systematically underestimates the density. The 2D bulk density n_C is shown by the dashed line.

Several words are in order regarding the island center electron density n_I. Etch trench depletion modeling at $V_{FG} = 0$ gives $n_I \sim 2$ % lower than n_B, and ~ 7 % greater than constriction saddle point density n_C .[30, 74] This is consistent with the results shown in Figure 4.11, giving $n_C \approx 0.92 n_B$ at $V_{FG} = 0$. While present QH transport experiments do not probe n_I, an analysis of V_{FG} dependence of the period of the Aharonov-Bohm oscillations at lower filling $f \leq 4$ integer QH plateaus has lead us to conclude that n_C decreases proportionately less than n_I, upon application of a negative V_{FG} .[29, 31] This experimental conclusion is counterintuitive, but can be understood if one considers that the front gates have long leads and surround the island, while being only to one side of a constriction (Figure 4.1). Accordingly, the island QH edge channels, which follow the constant electron density contours with density equal that in the constrictions, move inward, towards the island center, the interference path area shrinks, and the Aharonov-Bohm period increases.

Chapter 5

Aharonov-Bohm Oscillations in Transition between Integer Quantum Hall States[2]

An apparent h/fe Aharonov-Bohm flux period, where f is an integer, has been reported in coherent quantum Hall devices. Such subperiod is not expected for noninteracting electrons and thus is thought to result from interelectron Coulomb interaction. Here we report experiments in a Fabry-Perot interferometer comprised of two wide constrictions enclosing an electron island. By carefully tuning the constriction front gates, we find a regime where interference oscillations with period $h/2e$ persist *throughout* the transition between the integer quantum Hall plateaus 2 and 3, including half-filling. In a large quantum Hall sample, a transition between integer plateaus occurs near half-filling, where the bulk of the sample becomes delocalized and thus dissipative bulk current flows between the counterpropagating edges "backscattering". In a quantum Hall constriction, where conductance is due to electron tunneling, a transition between forward and backscattering is expected near the half-filling. In our experiment, neither period nor amplitude of the oscillations show a discontinuity at half-filling, indicating that only one interference path exists throughout the transition. We also present experiments and an analysis of the front-gate dependence of the phase of the oscillations. The results point to a single physical mechanism of the observed conductance oscillations: Aharonov-Bohm interference of interacting electrons in quantum Hall regime.

[2] Published in P. V. Lin, F. E. Camino, and V. J. Goldman, Phys. Rev. B **80**, 125310 (2008).

5.1 Background and Motivation

The Aharonov-Bohm effect demonstrates the primacy of the potentials rather than fields in quantum mechanics.[75-77] Specifically, for a dilute beam of noninteracting electrons propagating in a magnetic field $\mathbf{B}$, the vector potential $\mathbf{A}$ attaches a phase factor $\exp\{-i\frac{e}{h}\int_O^{\mathbf{r}}\mathbf{A}(\mathbf{r}')\cdot d\mathbf{r}'\}$ to the electron wave function at position $\mathbf{r}$. For enclosed electron orbits, the phase factor is periodic in flux Φ through the area $\mathbf{S}$ enclosed by the interference path: $\Phi = \oint \mathbf{A}(\mathbf{r})\cdot d\mathbf{r} = \int_S \mathbf{B}\cdot d\mathbf{S}$ by the virtue of the Stokes' theorem; the 2π period of the phase corresponds to the $\Phi_0 \equiv 2\pi\hbar/e = h/e$ flux period.

Electron interaction usually does not affect the h/e Aharonov-Bohm flux period observed in conductance of normal metal and semiconductor rings with two leads. The situation is more complex in quantum Hall devices. An apparent h/fe Aharonov-Bohm flux period, where f is the integer quantum Hall effect (QHE) filling in the constrictions, has been reported in quantum antidot[78-79] and Fabry-Perot interferometer devices.[19, 29, 31] In quantum antidots, the closed Aharonov-Bohm path follows an equipotential around the lithographically defined potential hill in the two-dimensional (2D) electron plane. In interferometer devices, the interference path follows an equipotential at device's edges, and is closed by two tunneling links.

The experiments are done in a uniform magnetic field, so that a well-defined interference path enclosing an area is needed to translate the field into flux. This Aharonov-Bohm subperiod is accompanied by an e charge period as a function of a gate voltage, and is not affected by the 2D bulk filling outside the device. In quantum antidots, previously reported $h/2e$ period[14, 80] was tentatively attributed to spin-splitting of a Landau level. However, subsequent work has concluded that no model of non-interacting electrons can consistently explain this subperiod.[81-82] On the other hand, it seems apparent that the strong intereletron Coulomb interaction, present in nearly all QHE

samples, can naturally cause the observed Aharonov-Bohm and charge periods by substantially mixing the Landau level electron occupation.[79]

An isolated metallic island weakly coupled by tunneling to two electrodes displays quasiperiodic conductance oscillations observed as a function of gate voltage. In such Coulomb islands,[83-84] the net island charge $Q = -e(N - N_{\text{eq}})$ increments in steps of one electron due to the Coulomb blockade which opens a gap of $Q^2 / 2C$ in the island energy spectrum. The island has total capacitance C to the gate and the electrodes. Here N is the number of electrons in the nearly isolated island, an integer, and the equilibrium expectation value $N_{\text{eq}} = N_{\text{ion}} + N_{\text{gate}}$ is the sum of two terms: the number of electrons neutralizing the positively charged background of the fixed ions in the crystal lattice N_{ion} and the continuously varying polarization charge $N_{\text{gate}} = -\alpha V_{\text{gate}}$ induced by a gate voltage V_{gate}. Under conditions of low temperature and excitation (bias voltage between the two electrodes), the net island charge oscillates between $Q = -\frac{1}{2}e$ and $Q = \frac{1}{2}e$, conductance peaks occurring at gate voltages when N_{eq} is an integer and Q is zero, so the Coulomb gap vanishes.

Phenomenological Coulomb blockade models were proposed to evaluate the effects of on-site interaction in quantum antidot[81-82] and Fabry-Perot geometry.[59, 85-88] Specifically, it has been proposed that two distinct mechanisms producing conductance oscillations exist: one being Aharonov-Bohm interference of backscattered electrons, another is caused by forward scattering via a "compressible island" subject to Coulomb blockade (see Fig. 1 in Ref. 87). The third possibility, the backscattering via a compressible island (shown in Fig. 1 in Ref. 20 and as "type ii" in Ref. 87), does not conserve angular momentum in the integer QHE regime, and thus is expected to be much weaker. Experiments aimed at distinguishing the distinct Coulomb blockade and the Aharonov-Bohm mechanisms have been reported.[55, 89-90]

However: (i) a compressible island has no well-defined area, so that while Coulomb blockade is possible, it does not necessarily lead to $B-$periodic oscillations as a function of a uniform applied magnetic field. (ii) A compressible island, if formed, would vary in size and shape from a point at the island center to a ring of maximal radius,

when filling is changed in a QHE plateau transition; thus the forward tunneling distance and tunneling conductance would vary enormously. (iii) Further, in semiconductor heterostructures with $\sim 200\,\mathrm{nm}$ 2D depletion length, the confining potential has considerable radial gradient which results in a discrete island energy spectrum; no strictly compressible island is possible in the limit of low temperature.

The state of affairs is further obscured by the fact that the single-electron tunneling dynamics is similar for the discrete electron spectra resulting from Coulomb blockade and quantum confinement. In particular, the Schrödinger equation can be solved for an electron constrained to move on a circular ring of radius R enclosing flux Φ. The energy is periodic in Φ, $E = \dfrac{e^2}{8\pi^2 mR^2}(\Phi - n\Phi_0)^2$, where n is an integer. The lowest energy radii correspond to enclosed flux of an integer multiple of Φ_0. If the orbit radius is fixed and the applied magnetic field is varied, this Aharonov-Bohm periodic energy dependence, consisting of a set of intersecting parabolas, with the ground state switching at half-integer values of Φ/Φ_0, is similar to the Coulomb blockade energy $E = \dfrac{e^2}{2C}(N - N_{\mathrm{eq}})^2$. Thus, the characteristic tunneling conductance "Coulomb blockade diamonds" seen in the source-drain bias versus gate voltage plots[81, 83] are also expected for any size-quantized electron system with a discrete energy spectrum, including an Aharonov-Bohm ring.

Here we report experiments on a Fabry-Perot electron interferometer in the regime of transition between $f = 2$ and 3 QHE plateaus. By fine tuning the two constrictions, we have obtained a continuous sequence of the Aharonov-Bohm oscillations persisting throughout the transition, including Landau level filling $\nu = 2.5$. The half-filling $\nu = f + 1/2$ separates the high$-B$ side of the $f+1$ plateau and the low-B side of the f plateau.[4, 32] The two situations have been interpreted as corresponding to backscattering and forward-scattering regimes, respectively.[55, 87] We observe experimental flux period $h/2e$ all through the plateau transition, although a period of $h/3e$ is expected for the $f = 3$ plateau. We also present experiments and an analysis of the gate dependence of the phase of the oscillations that shows that the slope of the

constant-phase stripes depends on details of the confining potential and device geometry. We conclude that all reported experimental results can be understood without invoking tunneling via a compressible island. The observed continuous sequence of sub $-h/e$ period oscillations argues strongly for a single physical mechanism: the Aharonov-Bohm interference of interacting electrons in QHE regime.

5.2 Aharonov-Bohm Oscillations between $f = 2$ and 3 Plateaus

The Fabry-Perot device, shown in the inset in Figure 5.1, was described previously.[30, 91] The etch trenches define two 1.2 μm wide constrictions, which separate an approximately circular electron island from the 2D bulk. Tunneling occurs in the two constrictions, thus forming a Fabry-Perot interferometer. The depletion potential of the trenches determines the electron density profile, see Figure 4.7. Four Au/Ti front gates are deposited in the etch trenches. Front gates are used to fine tune the constrictions for symmetry of the tunneling and to vary the overall device electron density, but the shape of the electron confinement potential is dominated by the etch trench depletion. The 2D density $\sim 1\times 10^{11}\,\mathrm{cm}^{-2}$ is achieved by illumination at $4.2\,\mathrm{K}$, there are ~3000 electrons in the island. Four-terminal longitudinal R_{XX} and Hall R_{XY} resistances (see inset in) were measured with 200 or 400 pA, $5.4\,\mathrm{Hz}$ AC current excitation. All data reported here were taken at the bath temperature of $10\,\mathrm{mK}$.

Figure 5.1 shows several R_{XY} traces, each with slightly different front-gate voltage on one side of one constriction. The $f = 2$ and 3 constriction plateaus are connected by a QHE transition region, where the $h/2e$ Aharonov-Bohm oscillations are superimposed on a varying background. Similar oscillations are also seen in R_{XX}. In general, unless the two constrictions are fine tuned, the B−regions with oscillations are interrupted, so that the plateau transition does not contain a continuous oscillation sequence. In a large 2D sample, a transition between two plateaus displays a smooth, monotonic R_{XY}.[92] The aperiodic peaks or dips in Figure 5.1, spaced by ~0.03 T, are attributed to disorder-assisted tunneling outside the constrictions; similar ubiquitous mesoscopic fluctuations are also seen in the same device at lower magnetic fields[91] and in quantum antidots. That the aperiodic peaks originate outside of the island is evidenced by their different response to front gates of the left and right constrictions.

By fine tuning the constriction gate voltage, we managed to obtain a continuous, uninterrupted oscillation sequence. Figure 5.2 shows a high-resolution R_{XY} trace measured with $200\,\mathrm{pA}$ excitation and the oscillatory conductance δG obtained by subtracting a smooth background. Although $200\,\mathrm{pA}$ produces only $2\,\mu\mathrm{V}$ constriction Hall voltage at $\nu \approx 2.5$, we still observe non-Ohmic behavior, namely, the oscillatory conductance amplitude still increases upon lowering of the excitation at $10\,\mathrm{mK}$ temperature. This is evidence that the extensive cold filtering employed lowers the electromagnetic background "noise" to $\leq 2\,\mu\mathrm{V}$ at the sample's contacts.

Note that the conductance oscillations can be seen, without interruption, of Figure 5.2 shows the magnetic field period of the oscillations. In these data $\Delta_B = 1.14\ \mathrm{mT}$ is closely one half of the $2.3\,\mathrm{mT}$ $f = 1$ period. Thus we interpret the oscillatory data in Figure 5.2 as displaying two oscillations per h/e, the fundamental flux period, in agreement with earlier results.[26-27, 29, 54-55, 89, 93] The same $h/2e$ flux period persists in the whole $2 \leftrightarrow 3$ QHE transition region. The weak, systematic variation in Δ_B as B is increased is caused by the gradual, secular inward shift of the island circling edge channel (interference path area shrinks), so as to maintain a constant $\nu = hn/eB$ in the local edge-channel electron density n when B is changing. The sign of the $d\Delta_B / dB$ slope is consistent with both: forward and backscattering at the saddle point in the constrictions. The oscillation amplitude is maximal near half-filling, and falls off toward the quantized plateaus, similar to that reported in a Mach-Zehnder interferometer.[93]

We discuss these data in terms of a specific edge-channel model below. Here we note that the oscillatory behavior in Figure 5.2 is dramatically different from resistance peaks and dips in quantum antidots. In quantum antidots, resonant tunneling peaks are seen on the low $-B$ side of a QHE plateau, and dips on the high-B side of the same plateau, both having equal flux period h/fe.[79] In particular, for the $2 \leq \nu \leq 3$ transition, there are two dips per h/e below the $f = 2$ plateau, and three peaks per h/e above the $f = 3$ plateau, separated by a smooth region near half-filling. Such behavior is consistent with two distinct tunneling regimes of backscattering and forward scattering in the

antidot geometry. The continuous oscillation sequence with a constant flux period is consistent with only backscattering occurring in Fabry-Perot interferometers.

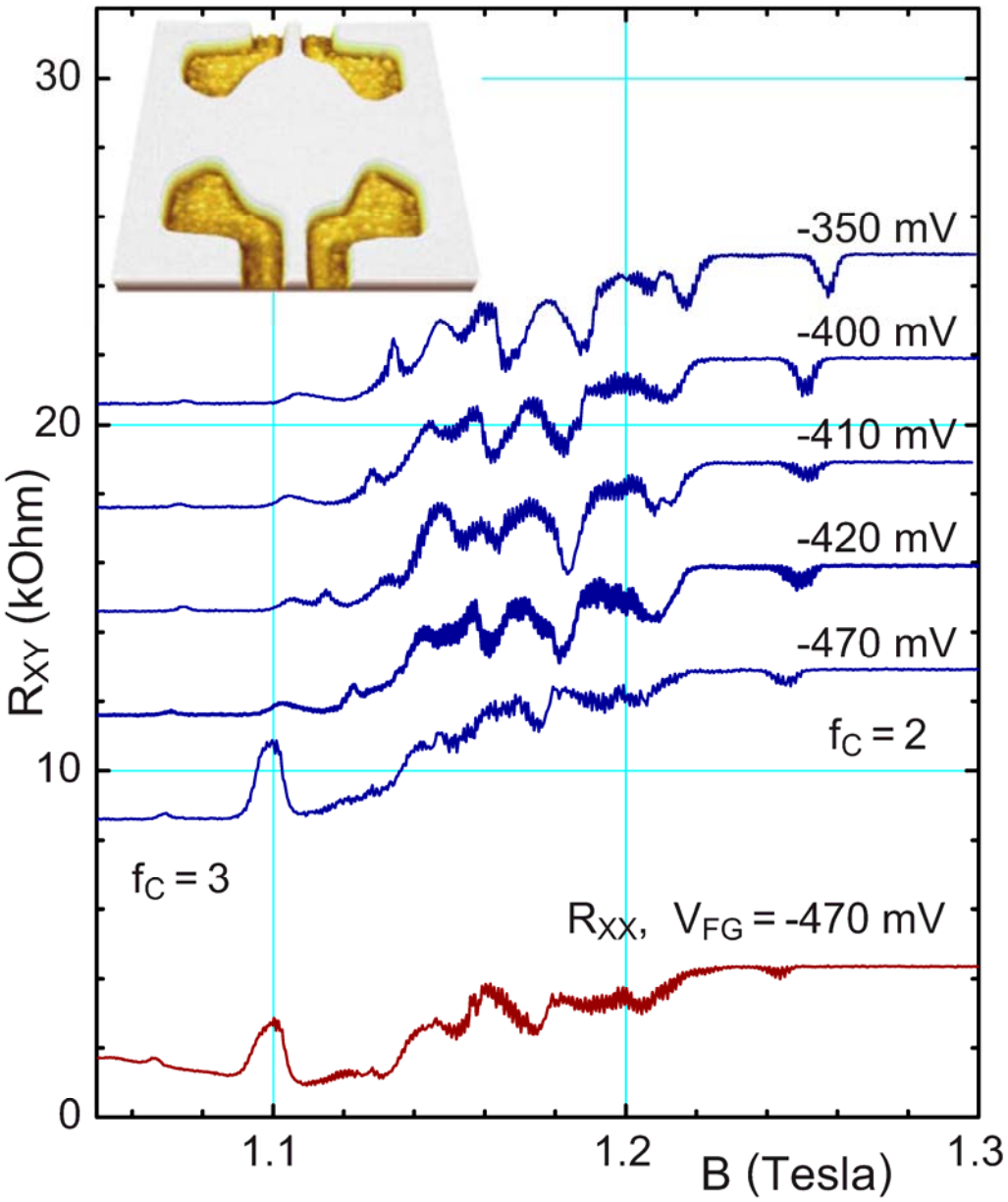

Figure 5.1: The Hall (R_{XY}) and longitudinal (R_{XX} , lowest trace) resistance of the interferometer device between constriction $f = 3$ and 2 QHE plateaus. The successive R_{XY} traces are shifted by $3\,\mathrm{k}\Omega$ and are labeled by bias of one of the front gates; the other three voltages are constant. Inset shows a $4 \times 4\,\mu$m AFM micrograph of the central region of the device.

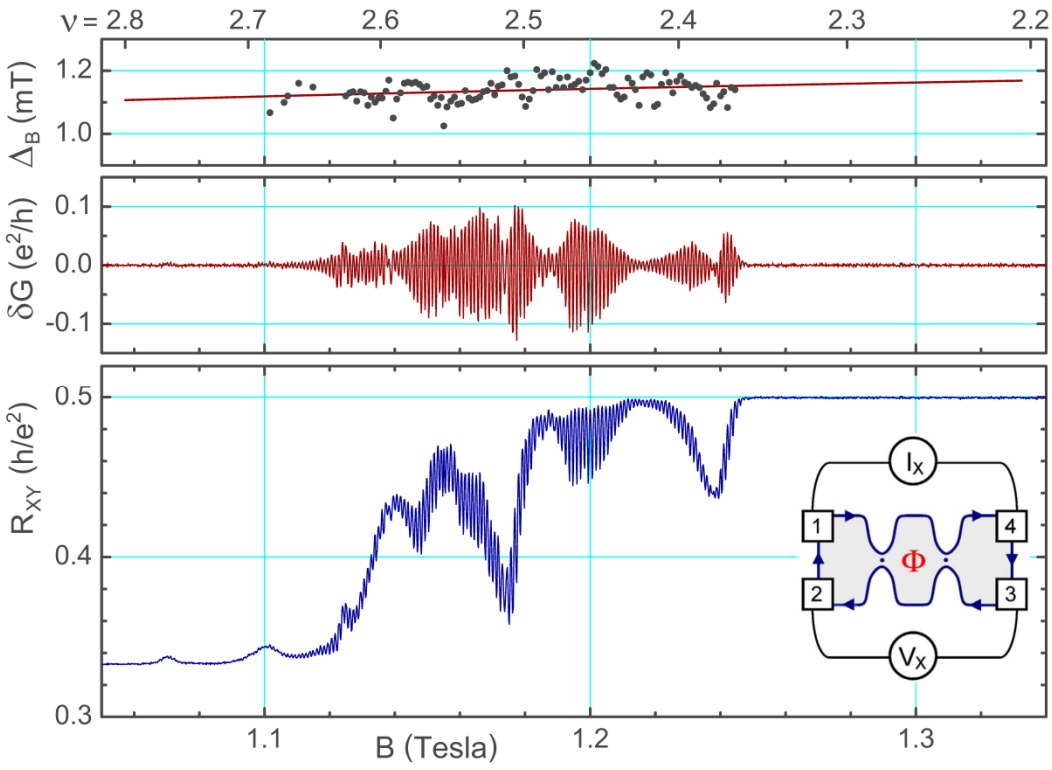

Figure 5.2: Hall resistance of the interferometer for the 2↔3 QHE plateau transition, the Landau-level filling is given at the top. The middle panel shows the oscillatory conductance and the upper panel the oscillation period; the red line is the linear fit: $\Delta_B = 0.104(2.5-\nu)+1.14$ mT . The oscillations persist uninterrupted throughout the transition region, including the half-filling. The inset shows four-terminal measurement configuration for $R_{XX} = V_X / I_X$; for R_{XY} current is passed 1–3, voltage is measured on contacts 2–4.

5.3 Front-gate Dependence of Aharonov-Bohm Oscillations

Figure 5.3 shows conductance oscillations at $\nu \approx 2.36$ with the front-gate voltage V_{FG} as a parameter. Here, all four $V_{\mathrm{FG1\text{-}4}}$ are stepped by a common bias of $0.01\,\mathrm{mV}$, and the average $V_{\mathrm{FG}} = \frac{1}{4}\sum_j V_{\mathrm{FG1\text{-}4}}$. The 2D electron density is greater in this cooldown than in Figure 5.2 so that equal ν occurs at a higher B. The fundamental flux period h/e contains two conductance oscillations, $S\Delta_{\mathrm{B}} = h/2e$. Stepping V_{FG} more negative reduces the overall island electron density and thus shifts the region of oscillations to lower B, see Figure 5.3 (b). The flux period is constant, but V_{FG} changes the interference path area S, form stripes spaced vertically by $V_{\mathrm{FG}} = 0.7 \pm 0.1\,\mathrm{mV}$. Interpreting V_{FG} as matching the change in the number of electrons within S by one gives $S(dn/dV_{\mathrm{FG}})\Delta_{V_{\mathrm{FG}}} = 1.0$, using the experimental $dn/dV_{\mathrm{FG}} = 7.9\times10^{14}\,\mathrm{m^{-2}V^{-1}}$, obtained from the low$-B$ magnetotransport,[91] and $S = h/2e\Delta_B = 1.83\times10^{-12}\,\mathrm{m^2}$, obtained from the Aharonov-Bohm period in Figure 5.3. This satisfactory agreement supports validity of our interpretation.

In general, the sign of the constant phase slope depends on details of heterostructure material and device geometry and fabrication. For one electron the Aharonov-Bohm phase $\gamma = -e\Phi/\hbar$. In a uniform B, the flux through the interference path $\Phi = BS$, and the differential

$$d\gamma/2\pi = -(e/h)(SdB + BdS)\,. \tag{5.1}$$

In the QHE of noninteracting electrons, in the symmetric gauge, each orbital in each Landau level is quantized so as to enclose an integer multiple of $\Phi_0 = h/e$,[4, 32] this also minimizes the $\frac{e^2}{8\pi^2 mR^2}(\Phi - n\Phi_0)^2$ per electron Aharonov-Bohm energy. Thus, the QHE ground-state maximum density electron droplet (a completely filled Landau level)

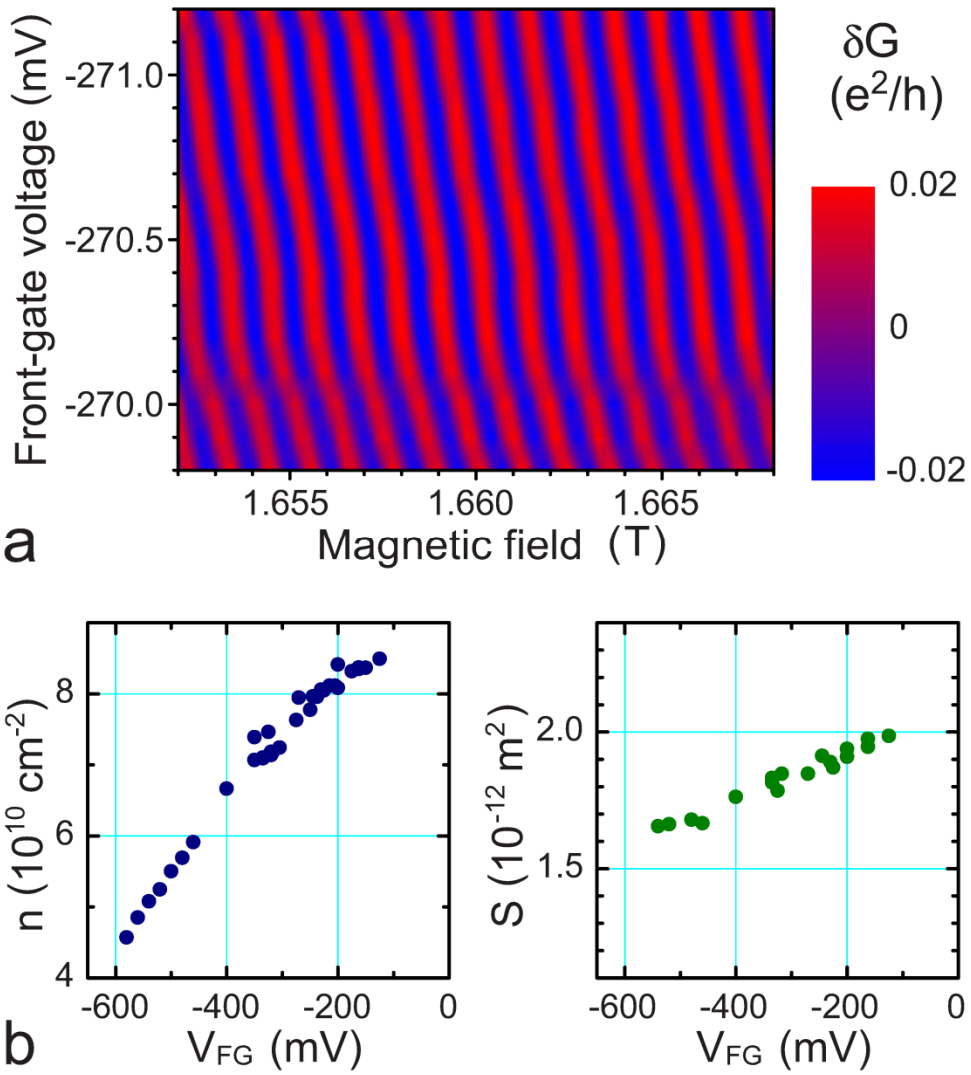

Figure 5.3: (a) Three-dimensional color plot of the Aharonov-Bohm oscillations on the $f = 2$ plateau $\nu \approx 2.36$. A negative V_{FG} is stepped by $0.01\,\mathrm{mV}$. The slope of the constant oscillation phase stripes is positive, consistent with Aharonov-Bohm effect in a QHE interferometer, as discussed in the text. (b) Constriction electron density and interference path area dependence on front-gate voltage. Constriction density n and interference S are determined from the B-field position and period of the $f = 2$ oscillations ($\nu \approx 2.5$) in several cooldowns.

is constructed by filling the Aharonov-Bohm orbitals from the center of the island (the minimum of the confining potential) outwards. Likewise, a partially filled Landau level contains an integer number of electrons within an Aharonov-Bohm path. Therefore, even the orbitals of noninteracting electrons in QHE regime are quantized to enclose an integer number of electrons in each Landau level. Invoking Coulomb blockade in ill-defined areas to ensure an integer number of electrons is redundant in this open geometry.

Between the QHE plateaus, at filling $f < \nu < f+1$, when f Landau levels are completely filled, lowering the uniform magnetic field and thus SdB by h/e "excites" f electrons. Thus $SdB - (h/fe)dN_e$, where N_e is thermal average number of the excited electrons (electrons in the $f+1$st Landau level) enclosed by the path. One may argue that the excitation of an electron into the partially filled Landau level is likely to modulate the conductance via the interference path closed by tunneling and thus result in conductance oscillations. This explains why there may be f conductance oscillations within the fundamental h/e period (or tunneling peaks in quantum antidots), but does not explain why the f oscillations are equally spaced in B or have equal amplitude.[79] Indeed, for noninteracting electrons the positions of oscillations in B depend on the detail of the confining potential, each oscillation originating in a different filled Landau level. For interacting electrons, the many-electron ground states involve occupation of higher Landau levels, "Landau-level mixing." But the basis orbitals, and thus the interference paths, are still quantized by the Aharonov-Bohm flux condition. When electron-electron interaction is strong, occupation of neighboring Landau levels is similar, and the "excited" electrons do not originate in any specific Landau level. Thus, excitation of an electron by reduction in B would result in approximately equivalent oscillations. This provides a qualitative model explaining the experimental observations as resulting from effects of electron Coulomb interaction on Aharonov-Bohm effect in QHE regime.[79] However, this qualitative model has proven difficult to implement in a formal theory.

We now turn to consideration of the effect of front gates. For interacting electrons, minimization of the ground-state energy requires local charge neutrality for 2D density n.[4, 32] Thus $\partial n/\partial B = 0$, and $\partial n_e/\partial B = -ef/h$. Using B and a gate voltage V as two independent variables, the differentials dN_e and dS are displayed as:

$$dN_e = (\partial N_e / \partial B)dB + (\partial N_e / \partial V)dV \,, \tag{5.2}$$

$$dS = (\partial S / \partial B)dB + (\partial S / \partial V)dV \,. \tag{5.3}$$

Here, the total number of electrons within the interference path is $N = nS$, and

$$\partial N_e / \partial B = -fBS / h + (1 - f / \nu)n(\partial S / \partial B) \,, \tag{5.4}$$

$$\partial N_e / \partial V = S(\partial n / \partial V) + (1 - f / \nu)n(\partial S / \partial V) \,. \tag{5.5}$$

Because the fraction of the excited electrons is $1 - f / \nu$, $n_e = (1 - f / \nu)n$. A gate changes the occupation only of the partially filled Landau level: $\partial n / \partial V = \partial n_e / \partial V$ in a fixed B. Combining the terms and defining $\beta = 2f / \nu - 1$, we obtain

$$\frac{f d\gamma}{2\pi} = -\left[\frac{feS}{h} + \beta n \frac{\partial S}{\partial B} \right] dB + \left[S \frac{\partial n}{\partial V} - \beta n \frac{\partial S}{\partial V} \right] dV \tag{5.6}$$

For etch trench depletion a good approximation may be the hard confinement: $\partial n / \partial B = 0$, $\partial n / \partial V = 0$. Then the periods (exciting one electron, $f \Delta_\gamma = 2\pi$) are $S\Delta_B = h / fe$ and $S\Delta_V = (\partial n / \partial V)^{-1}$. Note that the $B = \text{const}$, $V = \text{const}$ partial derivatives in Equation (5.6) are not equal to the experimental slopes in Figure 5.3 (b), which correspond to $\nu \approx \text{const}$.

The $d\gamma = 0$ stripe slope depends on the signs of the dB and dV multipliers in Equation (5.6). For electrons, the chief dB term is always positive. The net sign of the dV term depends on the two contributions. Positive gate voltage attracts electrons: $\partial n / \partial V$ is always positive; $\partial S / \partial V$ is negative for anticonfining (quantum antidots[78-79]) and positive for confining potential (Fabry-Perot devices). Mach-Zehnder devices[93-95] have one edge with confining and one with anticonfining potential, the net term depends on device details. In most experiments $\beta \sim 1$. Thus, the hard confinement model predicts a small positive $\gamma = \text{const}$, dV / dB slope for Fabry-Perot interferometers and quantum antidots. For devices with soft confinement and/or modulation gates the dV / dB slope can be large in magnitude (weak net gate coupling) and its sign depends on device details. A small modulation gate may have Sdn and ndS effects different than large gates.

A Coulomb blockade model of Ref. 87 was used in Ref. 89. It predicts constant oscillation phase when the charging energy is constant, $dN_e = 0$. However, the island area is assumed fixed for one device, while not so for the larger, very constricted

($n_C / n_B = 0.4$) device. We see that, in general, there are more terms contributing: gate voltage changes flux, too, by affecting the area ($\nu = \text{const}$ means $n / B = \text{const}$, not $N / B = \text{const}$).

5.4 Discussion of Edge Channel Structure

When the interference oscillations are observed, the counterpropagating edge channels must pass near the saddle points in the constrictions where tunneling occurs. Thus the filling of the relevant edge channels is determined by the saddle-point filling ν_C. The filling outside the constrictions and at the island center ν_I is greater than ν_C, the exact profile of the depletion is determined by the heterostructure material, device geometry and fabrication, and also by the gate voltage. In this device, $n_I / n_C \approx 1.07$, thus the entire interferometer, including the island center and the constrictions, is on the same integer QHE plateau for $f \leq 8$.[30, 91]

Figure 5.4 shows an illustration of edge-channel configurations used to analyze the Fabry-Perot geometry in Ref. 87. In this model, lines represent compressible edge channels, where local filling varies $f - 1 < \nu < f$, that carry edge currents. The incompressible (gapped) regions between the lines are at an exact filling $\nu = f$; they do not have low-energy charged excitations and so do not carry current, except when tunneling occurs. Tunneling through the energy barrier formed by the QHE gap occurs over a short distance t; for $t > 5\ell$ the tunneling rate $\propto \exp\left[-(t/2\ell)^2\right]$ is exponentially small. Here, the magnetic length $\ell = \sqrt{\hbar / eB}$. Tunneling between different Landau levels does not conserve angular momentum, or involves a spin flip, and is expected to be much weaker; thus the backscattering via a compressible island (type ii in Ref. 87) is not considered here.

In 2D, a compressible QHE state is formed near half-filling, when the top Landau level is half filled.[4] However, a confining potential lifts electron state degeneracy and a small confined "compressible island" is, in fact, incompressible in the low-temperature limit. This fundamental fact and the following detailed considerations seem difficult to reconcile with forward scattering via a compressible island as the mechanism of the

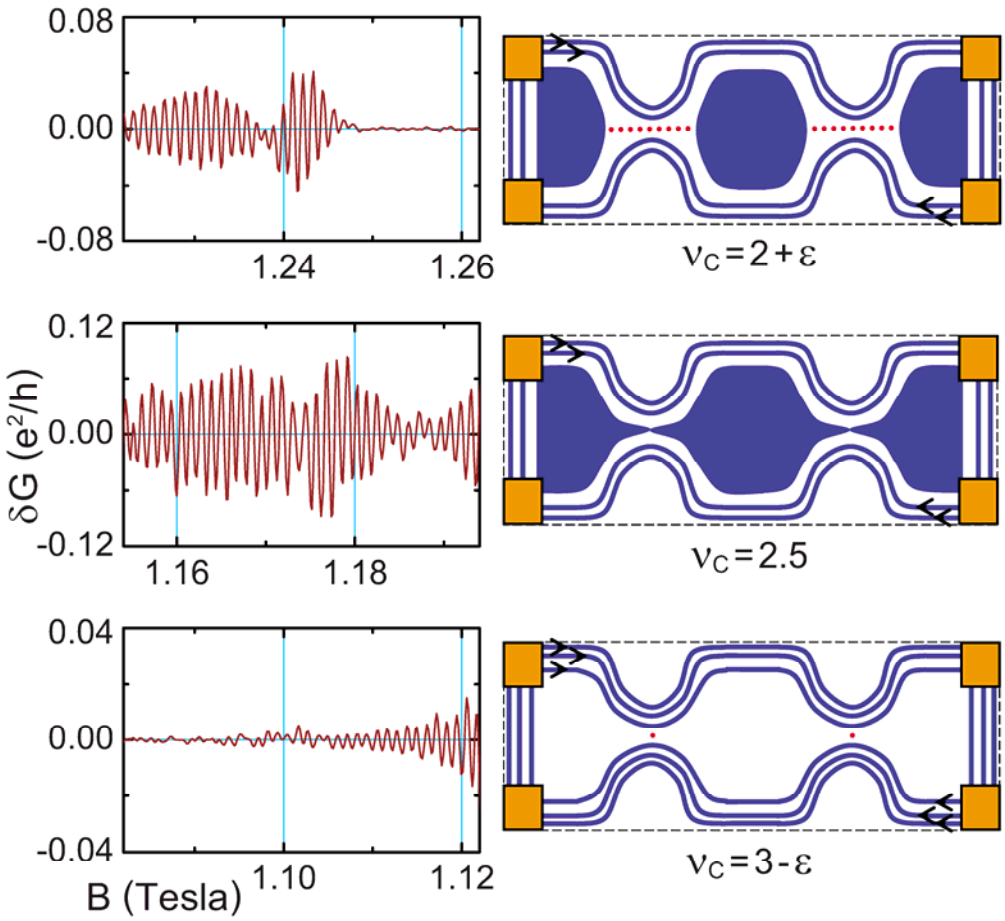

Figure 5.4: Right: illustration of edge-channel structure in a Fabry-Perot interferometer for the 2↔3 QHE plateau transition. The arrowed lines show edge channels connecting the Ohmic contacts (squares). Red dots in the constrictions show tunneling. The three regimes illustrated correspond to backscattering ($\nu_C = 3 - \varepsilon$), forward scattering ($\nu_C = 2 + \varepsilon$) and to half-filling. Left: the corresponding experimental oscillatory conductance for the 2↔3 QHE transition, see Figure 5.2

conductance oscillations reported in experiments. (i) Conductance oscillations periodic in applied uniform magnetic field B are observed in experiments. Gauge invariance requires periodicity in magnetic flux $\Phi = BS$;[77] a well-defined area S is necessary to translate a uniform field into flux through this area. Aharonov-Bohm area is well defined but it is not clear what exactly the area of a compressible island is. (ii) As a function of Landau-level filling factor $\nu = nh/eB$, in a transition between QHE plateaus f and $f+1$, the size of the compressible island changes from zero to a maximum value, so that a large variation in the $B-$period would result near half-filling $\nu = f + \frac{1}{2}$. (iii) Even at the maximum size, the radius of the compressible island must be less than the outer Aharonov-Bohm edge ring by at least $5\ell = 120\ \text{nm}$ at $B = 1.2\,\text{T}$ (See Figure 5.2). Thus one would expect a 30% smaller "compressible ring" area and thus 30% different oscillation periods Δ_B if the two distinct mechanisms were involved. This is not seen in the experiment, the maximal variation in Δ_B is under 10% (See Figure 5.2).

Similar conductance oscillations have been observed in devices with variously depleted constrictions, relative to the island center, from 5 to 50 %. Different saddle-point constriction depletion and filling factor would result in different edge-channel structure in the island. In a device with 50% depletion, Landau-level filling $\nu = 4.5$ in constrictions is accompanied by filling $\nu = 9$ at island center, so that several concentric compressible rings would be expected to form; while in a device with 5% depletion, the island center has $\nu = 1.26$ when $\nu = 1.20$ in constrictions, when oscillatory conductance has been reported, but no compressible island is expected at filling $\nu = 1.26$. Thus widely different regimes of constriction versus island center Landau-level fillings ν result in similar oscillatory behavior.

While pleasingly simple and easy to visualize, the edge channel models, like that of Figure 5.4, have certain serious drawbacks. It can be deceptive to imply both tunneling rate and the QHE filling by one set of lines, while tunneling is exponentially sensitive to distance and thus to detail of constriction. For example, in Figure 5.4, $\nu_C = 2 + \varepsilon$, hole forward scattering in the inner $2 < \nu < 3$ edge channels is shown; but electron backscattering between the outer $1 < \nu < 2$ channels, over a shorter distance in the

perpendicular direction, is also easy to envision. The tunneling rate for forward scattering can be extremely different for short and long constrictions, depending on device fabrication, while the backscattering rate is about the same. Another drawback is that the "compressible island" in Figure 5.4, $\nu_C = 2 + \varepsilon$, is not truly compressible: the electron state degeneracy is lifted by the confining potential. These energies can be estimated as the increment of the self-consistent (screened) confining potential over the distance separating two consecutive island-circling basis orbitals, like in quantum antidots[78-79]. This energy is 60 mK in the interferometer of Ref. 20, in agreement with thermal excitation experiments. In the present device it is slightly lower but still greater than temperature or excitation.

The continuous experimental oscillation sequence in Figure 5.2 is consistent with a single physical mechanism, rather than a different mechanism for the different regimes in the edge channel model of Figure 5.4 backscattering ($\nu_C = 3 - \varepsilon$) and forward scattering ($\nu_C = 2 + \varepsilon$), and also at half-filling ($\nu_C = 2.5$). Such interpretation has been disputed in Refs. 55, 89-90, where two physically different regimes, called "Aharonov-Bohm" for backscattering and "Coulomb blockade" for forward scattering have been proposed. The oscillatory behavior at half-filling has not been anticipated in Ref. 87. However, no qualitative discontinuity in the oscillation period or amplitude at half-filling is apparent in the data of Figure 5.2, and single physics, the Aharonov-Bohm interference of interacting electrons in QHE regime, appears to fit all the regimes.

Chapter 6

Interference of $e/3$ quasiparticles encircling 2/5 fractional quantum Hall island[3]

We report experiments in a large, 2.5 μm diameter Fabry-Perot quantum Hall interferometer with two tunneling constrictions. Interference fringes are observed as conductance oscillations as a function of applied magnetic field (the Aharonov-Bohm flux through the electron island) or a global backgate voltage (electronic charge in the island). Depletion is such that in the fractional quantum Hall regime, filling 1/3 current-carrying chiral edge channels pass through constrictions when the island filling is 2/5. The interferometer device is calibrated with fermionic electrons in the integer quantum Hall regime. In the fractional regime, we observe magnetic flux and charge periods $5h/e$ and $2e$, respectively, corresponding to creation of ten $e/5$ Laughlin quasiparticles in the island. These results agree with our prior report of the superperiods in a much smaller interferometer device. The observed experimental periods are interpreted as imposed by anyonic statistical interaction of fractionally charged quasiparticles.

[3] Published in P. V. Lin, F. E. Camino, and V. J. Goldman, Phys. Rev. B **80**, 235301 (2008).

6.1 Background

A system of electrons contained to move in two dimensional (2D) in a strong magnetic field exhibits exact quantization of Hall conductance at certain integer and fractional Landau level fillings.[1-4, 10] While the integer quantum Hall effect can be understood as a consequence of Landau quantization of non-interacting electrons, the fractional quantization is understood as resulting from condensation of interacting electrons into a highly-correlated incompressible fluid. The elementary charged excitations of a fractional quantum Hall (FQH) condensate are Laughlin quasiparticles possessing bizarre properties: they have fractional electric charge[3-4, 10, 14, 96-97] and obey anyonic (fractional) exchange statistics,[11-12, 20-22, 30] intermediate between the familiar Bose and Fermi statistics.

Upon exchange of two anyons, the quantum state of the system acquires a phase which is neither 0 nor π, but can be *any* value.[98] In two dimensions, one particle adiabatically encircling another is equivalent to their exchange done twice (exchange operation squared).[21] This topologically robust property can be used to detect anyons in interference experiments, because when either bosons or fermions encircle other particles, the system's wave function acquires an integer multiple of 2π phase difference, which does not affect the interference pattern. For anyons, the acquired phase difference is, in general, non-trivial, and thus does affect the interference. This nonlocal, topological interaction of anyons has lead to several proposals to use braiding of anyons in 2D systems for topological quantum computation.[25, 58]

Specifically, for charge $e/3$ quasiparticles of the filling $f = 1/3$ FQH fluid, an explicit calculation shows that the system's wave function acquires an anyonic Berry phase contribution when one Laughlin quasihole adiabatically encircles another.[12] Experiments on quantum antidots[38] and Fabry-Perot quantum Hall interferometers[30] reported Aharonov-Bohm flux period $\Delta_\Phi = h/e$ for the $e/3$ quasiparticles, while for fermionic or bosonic $e/3$ quasiparticles the expected flux period would be

$h/(e/3) = 3h/e$. These experimental results were interpreted as evidence that the quasiparticles of the $f = 1/3$ FQH fluid are indeed anyons, the "missing" $4\pi/3$ phase difference supplied by the statistical Berry phase contribution, in agreement with the theory of Ref. 12. Experiments[19, 29, 39, 55, 57, 89-90, 99] on two-constriction electron Fabry-Perot interferometer devices in the integer quantum Hall regime, and a chiral Luttinger liquid theory[24] of such devices in the primary Laughlin states were also reported.

Less clear theoretically is the situation when different kinds of quasiparticles are involved, even for the next simplest case of the $e/3$ and the charge $e/5$ quasiparticles of the 2/5 FQH fluid, which is the simplest hierarchical "daughter state" of the 1/3 fluid.[11, 35] Earlier, we reported experiments on an interferometer where $e/3$ quasiparticles of the 1/3 FQH fluid encircle an island of the 2/5 fluid.[18, 20, 28, 31] The interference conductance oscillations occur as a function of magnetic field, or the island electronic charge varied by a backgate. The flux and charge periods were obtained using the Aharonov-Bohm interference area,[75-76] which, in turn, was determined either from modeling of the island electron density profile,[20] or experimentally, via scaling the Aharonov-Bohm period dependence on front-gate voltage.[31] The reported flux and charge superperiods, $\Delta_\Phi = 5h/e$ and $\Delta_Q = 2e$, were deduced theoretically using several FQH island models.[88, 100-102] On the other hand, these periods were reported as either "not understood" in a Coulomb blockade model,[87] or even claimed as not possible in a composite fermion model[103] of the island.

Here we report experimental results obtained in a similar Fabry-Perot electron interferometer device, but with much larger 2D electron island, see inset in Figure 6.1. The integer quantum Hall regime is used to determine the interferometer island area. In the FQH regime, the interfering $e/3$ quasiparticles execute a closed path around the island of the 2/5 FQH fluid containing $e/5$ quasiparticles. The 2D electron depletion, which largely determines the width of the $f = 1/3$ edge ring, does not depend on the device diameter. On the other hand, the enclosed 2/5 island is several times larger than before.[18, 20, 28, 31] Hence, in this device, most of the island area is occupied by the 2/5 FQH fluid under coherent tunneling conditions, so that the directly-measured magnetic field period well approximates the flux period. We confirm the previously reported flux and

charge superperiods of $\Delta_\Phi = 5h/e$ and $\Delta_Q = 2e$, respectively, both corresponding to addition of ten $e/5$ quasiparticles to the area enclosed by the interference path. These results are consistent with the Berry phase quantization condition that includes both Aharonov-Bohm and anyonic statistical contributions.[101]

6.2 Devices and Measurement Techniques

The electron interferometer device was fabricated from a low disorder AlGaAs/GaAs heterojunction crystal with 2D electrons $\sim 320\,\mathrm{nm}$ below the surface.[61] The four independently-contacted front gates (FG) were defined by electron beam lithography on a pre-etched mesa with Ohmic contacts. After a shallow $\sim 160\,\mathrm{nm}$ wet etching, Au/Ti front-gate metal was deposited in the etch trenches, followed by lift-off, inset in Figure 6.1. The etch trenches define two $\sim 1.1\,\mu\mathrm{m}$ lithographic width constrictions, which separate an approximately circular electron island from the 2D "bulk". Moderate front-gate voltages V_{FG} are used to fine tune the constrictions for symmetry of the tunnel coupling and to increase the oscillatory interference signal. The shape of the electron density profile is predominantly determined by the etch trench depletion. The depletion potential has saddle points in the constrictions, and so has the resulting density profile. For the 2D bulk density $n_{\mathrm{B}} = 1.0\times 10^{11}\,\mathrm{cm}^{-2}$ there are ~4,500 electrons in the island.

The lithographic layout and dimensions of the present device are very similar to the device in Refs. 30 and 92, that has the entire island at filling 1/3 in the fractional regime. The two significant differences are: (i) the constriction-defining lip of the front gates is widened, and (ii) the etch trench depth is greater by $\sim 20\,\mathrm{nm}$. These relatively small differences combine to yield about three times more depleted constrictions, with the saddle point electron density estimated as ~0.78 of the island center density. This results in formation of a filling 1/3 edge ring passing through the constrictions, when the island and the 2D bulk both have FQH filling 2/5.

Samples were mounted on sapphire substrates with Indium metal, which serves as the global backgate, and were cooled in the tail of the mixing chamber of a ^{3}He-^{4}He dilution refrigerator, immersed in the mixture. All data reported here were taken at $10.3\,\mathrm{mK}$ bath temperature, calibrated by nuclear orientation thermometry. The electromagnetic environment incident on the sample is attenuated by a combination of

RF-lossy manganine wire ribbons and a series of cold low-pass RC network filters with a combined cut-off frequency $\sim 50\,\mathrm{Hz}$. Extensive cold filtering cuts the electromagnetic "noise" environment incident on the sample to $\sim 7\times10^{-16}\,\mathrm{W}$, allowing to achieve an effective electron temperature $\leq 15\,\mathrm{mK}$ in an interferometer device.[28]

6.3 Aharonov-Bohm Superperiod

Figure 6.1 shows longitudinal and Hall resistances in the interferometer sample with $V_{FG} \approx 60\,\mathrm{mV}$, similar to front-gate voltage in the oscillatory regime. Four-terminal resistance $R_{XX} = V_X / I_X$ was measured with $100\,\mathrm{pA}$ ($f = 1/3$) or $200\,\mathrm{pA}$ ($f = 1$) $5.4\,\mathrm{Hz}$ AC current injected at contacts 1 and 4. The resulting voltage V_X, including the Aharonov-Bohm oscillatory signal, was detected at contacts 2 and 3. The Hall resistance $R_{XY} = V_{4\text{-}2} / I_{3\text{-}1}$ is determined by the quantum Hall filling f_C in the constrictions, giving definitive values of f_C. The oscillatory δR is obtained from the directly measured R_{XX} or R_{XY} data after subtracting a smooth background. The conductance δG is calculated from δR and the quantized Hall resistance $R_{XY} = h / fe^2$ as $\delta G = \delta R / (R_{XY}^2 - \delta R R_{XY})$, a good approximation for $\delta R \ll R_{XY}$.

In the range of B where the interference oscillations are observed, the counterpropagating edge channels must pass near the saddle points, where tunneling may occur.[20, 30] Thus, the filling of the edge channels is determined by the saddle point filling. This allows to determine the saddle point density from the $R_{XX}(B)$ and $R_{XY}(B)$ magnetotransport; a systematic study of quantum Hall transport and analysis were reported for a similar sample in Ref. 91. The local Landau level filling $\nu = hn / eB$ is proportional to the local electron density n; accordingly the constriction ν_C is lower than the bulk ν_B in a given B. While ν is a variable, the quantum Hall exact filling f is a quantum number defined by the *quantized* Hall resistance as $f = h / e^2 R_{XY}$.

In this device, the island center density is estimated to be close to the bulk n_B at $V_{FG} = 0$, the constriction vs. island center density difference is ~20%. Thus, the whole interferometer can be on the same plateau for strong quantum Hall states with wide plateaus, such as $f = 1$ and 1/3. For example, in Figure 6.1, there is a range of B when both $f_C = 1$ and $f_B = 1$, as seen for $3.6\,\mathrm{T} < B < 4.2\,\mathrm{T}$, and both are $f = 1/3$ for $B > 12\,\mathrm{T}$.

The second possibility is an overlap of two plateaus with different filling. For example, a quantized value of $R_{XX} = h/e^2(1/f_C - 1/f_B) = h/4e^2$ for $f_C = 1$ and $f_B = 4/3$, is seen at $B \approx 3.2\,\mathrm{T}$; and $f_C = 1/3$ and $f_B = 2/5$, resulting in $R_{XX} = h/2e^2$, in the range $11.0\,\mathrm{T} < B < 11.6\,\mathrm{T}$ in Figure 6.1. However, $f_C = 2$, $f_B = 3$, e.g., when $n_C \approx 0.67 n_B$, is not seen in this sample.

In the integer quantum Hall regime the Aharonov-Bohm ring is formed by the two counterpropagating chiral edge channels passing through the constrictions.[19, 29] Backscattering, which completes the interference path, occurs by quantum tunneling at the saddle points in the constrictions. The relevant particles are electrons of charge $-e$ and Fermi statistics, thus we can obtain an absolute calibration of the Aharonov-Bohm path area and the gate action of the interferometer. Figure 6.2 shows conductance oscillations for $f = 1$; analogous oscillations for $f = 2$ were studied in this device, but are not reported here. The $f = 1$ magnetic field oscillation period is $\Delta_B = 1.06\ \mathrm{mT}$. The flux period here is $\Delta_\Phi = h/e$, this gives the interferometer path area $S = h/e\Delta_B = 3.91\ \mu\mathrm{m}^2$, the radius $r_{\mathrm{Out}} = 1115\ \mathrm{nm}$.

We also observe the interferometric oscillations as a function of magnetic field in the FQH regime, when an $f = 1/3$ edge ring surrounds a 2/5 fluid island, Figure 6.2. This occurs when the bulk 2/5 plateau and the constriction 1/3 plateau overlap, when the longitudinal $R_{XX} = h/e^2(3 - 5/2) \approx h/2e^2$. The magnetic field oscillation period in this regime is $\Delta_B = 5.7 \pm 0.3\ \mathrm{mT}$. Assuming the flux period is $\Delta_\Phi = 5h/e$, this gives the interferometer path area $S = 5h/e\Delta_B = 3.60\ \mu\mathrm{m}^2$, the radius $r_{\mathrm{In}} = 1070\ \mathrm{nm}$. The conductance oscillations in this regime are found to be robust and reproducible, Figure 6.3, systematically responding to a moderate change of front-gate voltage, as reported before for a smaller interferometer device.[31]

Classically, increasing B by a factor of ~3 does not affect the electron density distribution in the island at all. Quantum corrections are expected to be small for a large island containing ~4,500 electrons.[46] Indeed, in experiments on a similar device, the

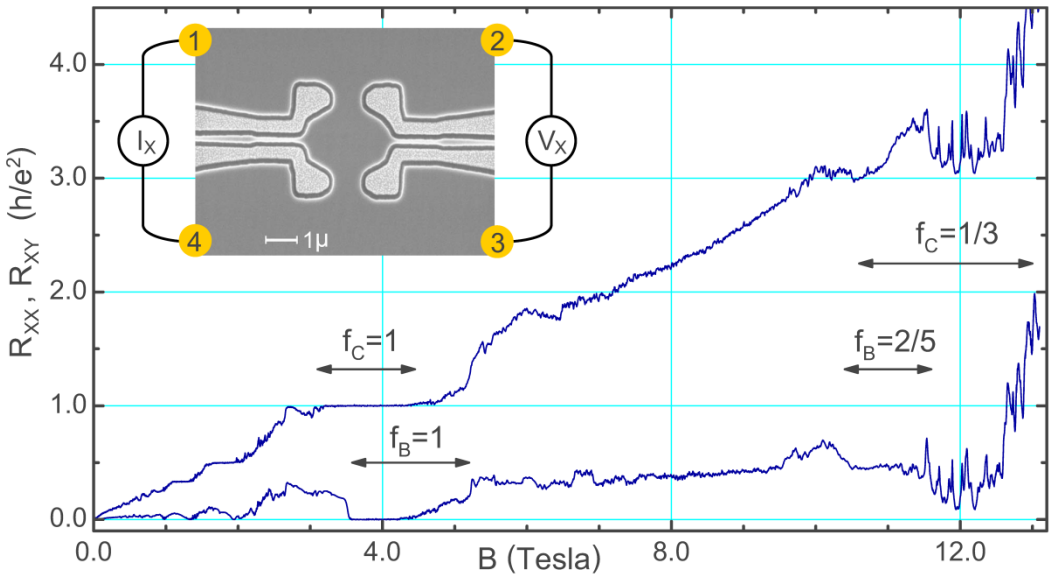

Figure 6.1: The longitudinal R_{XX} (lower trace) and Hall R_{XY} magnetoresistance of the interferometer. The quantized plateaus (bulk f_B, constriction f_C) allow to determine the filling factor in the constrictions. The fine structure is due to quantum interference effects, sharp peaks are due to impurity-assisted tunneling. Inset: electron micrograph of the interferometer device. The front gates (light) are deposited in shallow etch trenches (dark). Depletion potential of the trenches defines the electron island. The edge channels circling the island are coupled by tunneling in the two constrictions, thus forming a Fabry-Perot interferometer. The backgate (not shown) extends over the entire 4×4 mm sample.

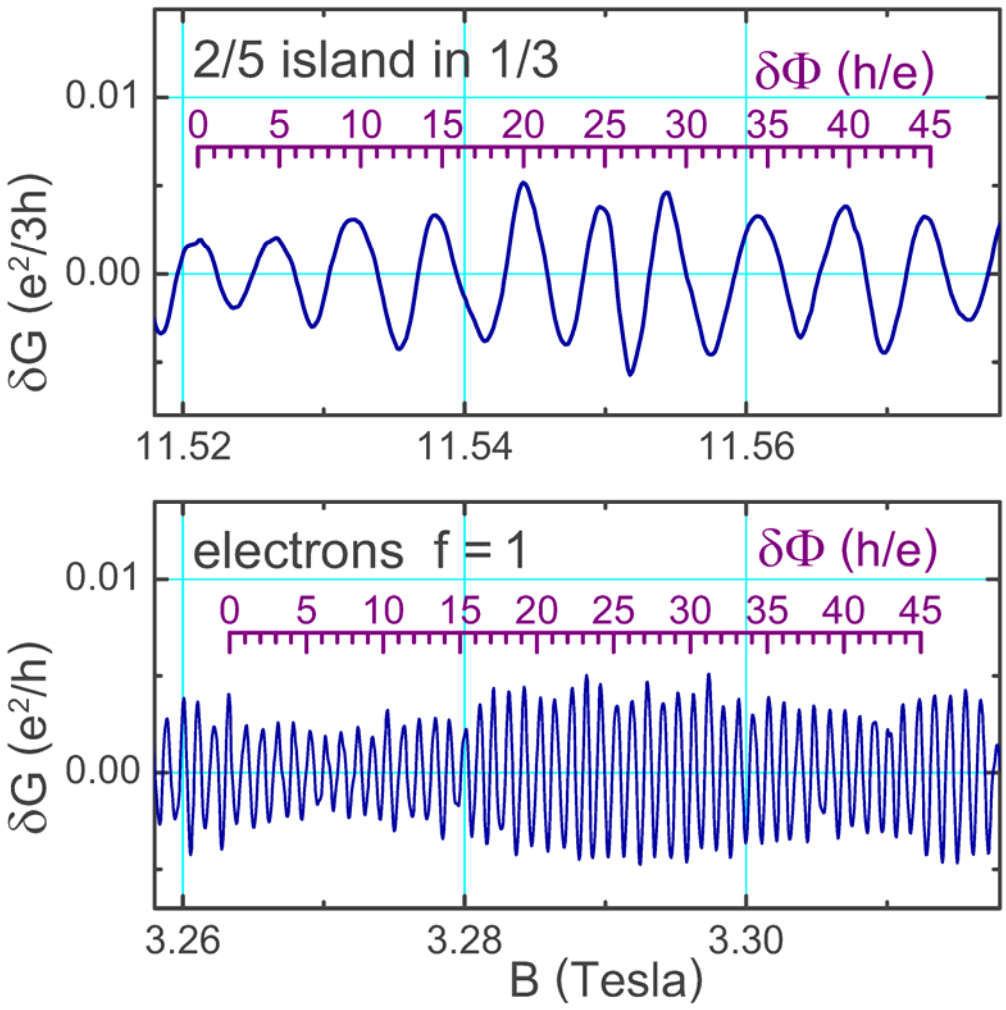

Figure 6.2: Representative interference conductance oscillations for electrons, $f = 1$, and for $e/3$ quasiparticles in $f = 1/3$ edge channel circling around an island of 2/5 FQH fluid. Both are plotted on the same magnetic field scale, the magnetic field period ratio is 5.4 ± 0.3. The flux scales are slightly different because the 2/5 island area is ~7% less than the $f = 1$ edge ring area.

$f = 1/3$ edge ring area was found to equal the integer value, within the ±3% experimental uncertainty.[30] As in the model of Ref. 20, in the fractional regime, the outer $f = 1/3$ edge ring of radius r_{Out} encloses the 2/5 FQH island of radius r_{In}. The difference $r_{\mathrm{Out}} - r_{\mathrm{In}} \approx 45$ nm ($\approx 6\ell$, the magnetic length $\ell = \sqrt{\hbar / eB}$) approximates the width of the 1/3 incompressible ring. This width can be estimated from the model of Ref. 46: the incompressible edge "dipolar strip" width is $a_{1/3} = 50$ nm, where we use the value of the electron density gradient $\left[dn/dr \right]_{r=r_{\mathrm{Out}}} = 3.6 \times 10^{20}\,\mathrm{m}^{-3}$ from a self-consistent island density model,[19-20] and the $f = 1/3$ FQH gap of 5 K at 12 T. The square of $a_{1/3}$ is proportional to gap and inversely proportional to the density gradient. Since the FQH gap is itself a weak function of B, $a_{1/3}$ is more sensitive to the gradient of the self-consistent island confining potential.

The ratio of the magnetic field periods Δ_B for the integer and fractional regime oscillations is 5.4 ± 0.3 in this sample. In interferometers with a smaller island (that also had somewhat different lithographic design), we reported the Δ_B ratio 7.15 for a $r_{\mathrm{Out}} = 685$ nm, $r_{\mathrm{In}} = 570$ nm device, and ratio 6.3 ± 0.4 for a $r_{\mathrm{Out}} = 920$ nm, $r_{\mathrm{In}} = 820$ nm device.[19-20] Evidently, as the device area increases, the ratio of the magnetic field periods approaches 5 because the 2/5 FQH island occupies a larger part of the whole island area. Since the fundamental flux period is h/e in the $f = 1$ integer regime, we conclude that the flux period is indeed $\Delta_\Phi = 5h/e$ when $e/3$ quasiparticles of the $f = 1/3$ FQH fluid execute a closed path around an island of the 2/5 fluid.

We use the backgate technique to measure the charge period in the fractional regime.[14, 16, 20, 30] The backgate action $\delta Q / \delta V_{\mathrm{BG}}$, where Q is the electronic charge within the Aharonov-Bohm path, is calibrated with electrons in the integer regime. The calibration is done by evaluation of the coefficient α in $\Delta_Q = \alpha(\Delta_{V_{\mathrm{BG}}} / \Delta_B)$, setting $\Delta_Q = e$ in the integer regime. Note that this procedure normalizes the backgate voltage periods by the experimental $B-$ periods, canceling the variation in device area, for different devices and due to a front-gate bias. We could not calibrate α directly in the

same device since there was a leakage present between the back- and front gates, which was observed to increase fast at lower magnetic fields. Instead, we use the coefficient $\alpha \approx 7.44e$ mT / V for the similar interferometer device fabricated from the same GaAs heterojunction wafer.[30]

Figure 6.4 shows the oscillations as a function of V_{BG} in the fractional regime, and also the corresponding oscillations as a function of B. The front-gate voltage is the same for this matched set of complementary data. The periods are $\Delta_{V_{\mathrm{BG}}} = 303$ mV and $\Delta_B = 5.61$ mT. Using the interferometer area obtained directly from the Aharonov-Bohm data, i.e., taking into account that Δ_B corresponds to five "flux quanta", we obtain $\Delta_Q = \alpha(5\Delta_{V_{\mathrm{BG}}} / \Delta_B) = 2.01e$, equal (within the experimental uncertainty) to the expected value $\Delta_Q = 2e$.

In addition, the ratio $\Delta_{V_{\mathrm{BG}}} / \Delta_B = 54.1$ V / T, multiplied by the calibration coefficient α / e, is expected to give the ratio of electrons per "flux quanta", the quantum Hall filling f. Indeed, using the experimental periods we obtain $\alpha(\Delta_{V_{\mathrm{BG}}} / \Delta_B) = 0.403 \pm 0.001$, closely matching $f = 2/5$ and significantly distinct from $f = 1/3$. Thus, we conclude that the oscillations in Figure 6.4 have the flux period $\Delta_\Phi = 5h/e$ and the charge period $\Delta_Q = 2e$, consistent with the prior report.[20] Using the $\Delta_{V_{\mathrm{BG}}} / \Delta_B$ ratio technique and the matched (vs V_{BG}, vs B) data sets cancels, to first order, the dependence of the V_{BG} and B periods on the interferometer area and front-gate bias.

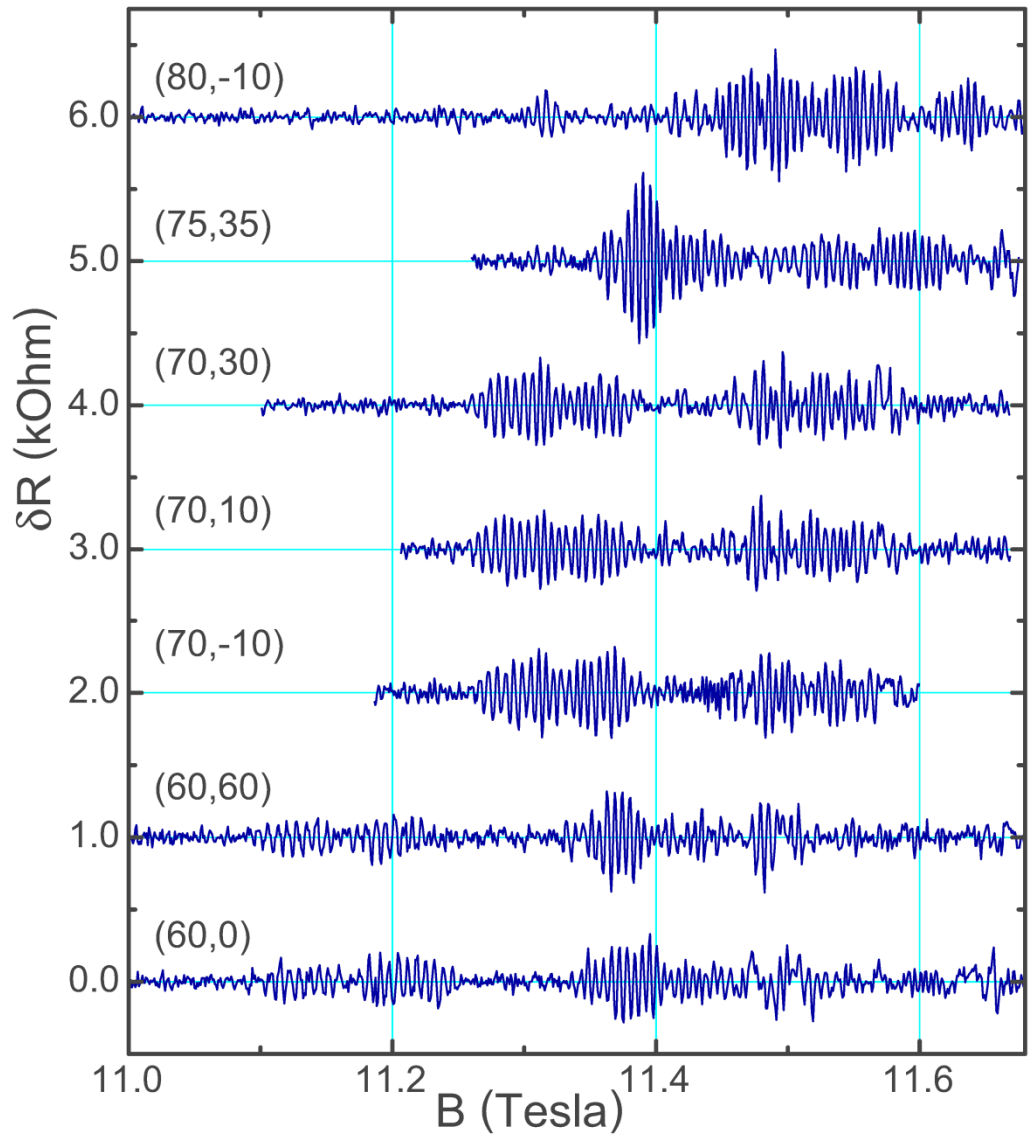

Figure 6.3: Representative oscillatory δR traces in the regime of $e/3$ quasiparticles encircling the 2/5 FQH island. Moderate front-gate V_{FG} is applied, the δR traces are labeled $(V_{\mathrm{FG1,2,3}}, V_{\mathrm{FG4}})$; the three voltages $V_{\mathrm{FG1,2,3}}$ are equal. Successive traces are shifted by $1\mathrm{k}\Omega$. A positive front-gate voltage increases the island electron density and shifts the region of oscillations to higher B.

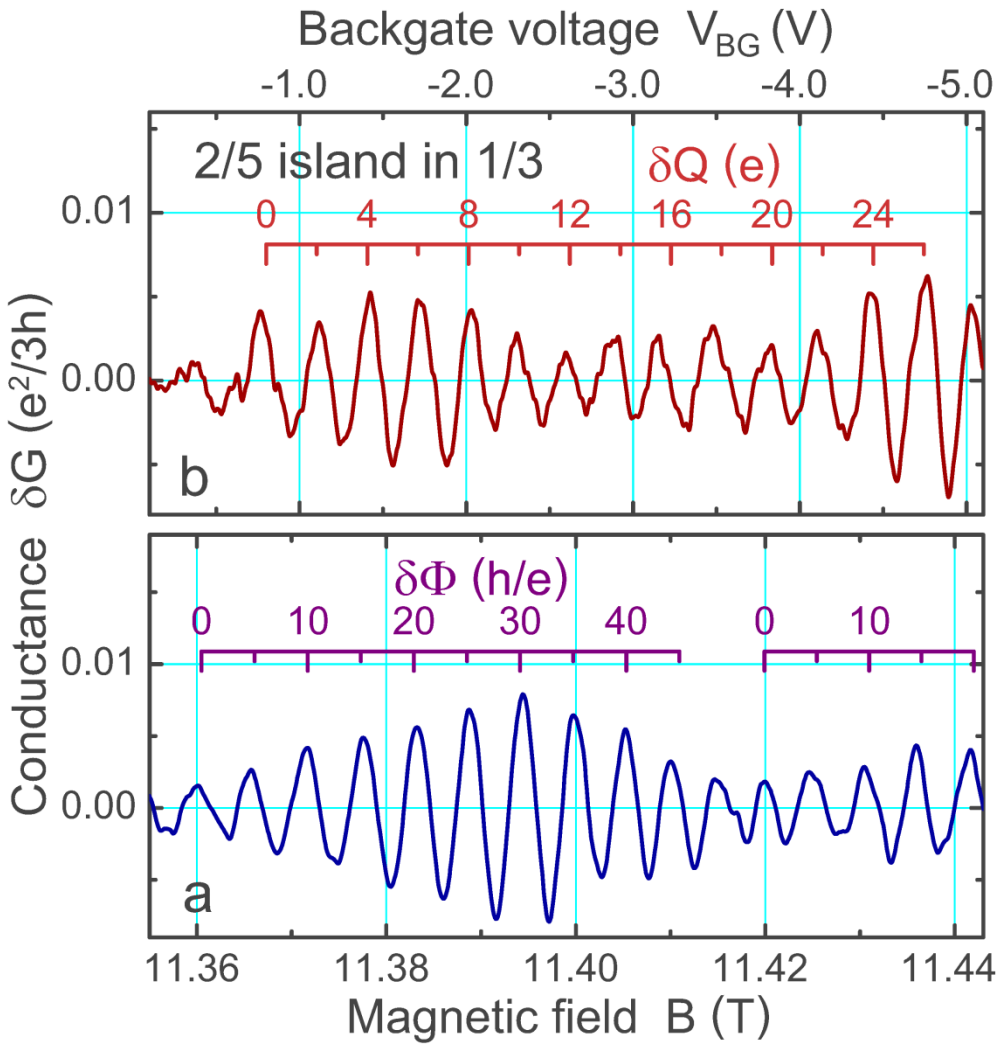

Figure 6.4: A matched set of interference conductance oscillations in the regime of $e/3$ quasiparticles circling an island of the 2/5 FQH fluid. (a) Magnetic flux through the island period $\Delta_\Phi = 5h/e$ corresponds to creation of ten $e/5$ quasiparticles in the 2/5 fluid, two per h/e. (b) The backgate voltage island charging period $\Delta_Q = 2e = 10(e/5)$ agrees with incremental addition of ten $e/5$ quasiparticles. The ratio of the two periods confirms that the interference originates in the $f = 2/5$ FQH island. The interferometer device is calibrated using conductance oscillations for electrons, $f = 1$.

6.4 Analysis and Discussion

Experiments clearly show interference of Laughlin quasiparticles in an edge channel of the filling $f = 1/3$ FQH fluid, passing through the constrictions and circling an $f = 2/5$ island. Experimental tests establish: (i) the transport current displaying the interference signal is carried by the $e/3$ Laughlin quasiparticles, as evidenced by the Hall $R_{XY} = 3h/e^2$ and $R_{XX} = 2h/e^2$, in Figure 6.1 and in Fig. 4 in Ref. 20; (ii) the interference signal has magnetic flux period $\Delta_\Phi = 5h/e$ and the corresponding electric charge period $\Delta_Q = 2e$, see Figure 6.2 and Figure 6.4; (iii) these superperiods originate in an island that has the FQH filling 2/5, as is evident from the period ratio and is further supported by 2D electron island depletion modeling. These experimental superperiods do not violate gauge invariance,[76, 104] and can be understood as follows.[101]

In an unbounded 2D FQH fluid, changing $\nu = hn/eB$ away from the exact filling f is accomplished by creation of quasiparticles; the ground state consists of the $\nu = f$ condensate and the matching density of quasiparticles.[3-4, 10, 105] Starting at $\nu = f$, changing magnetic field adiabatically maintains the system in thermal equilibrium. The equilibrium electron density, determined by the positively charged donors, is not affected. In present geometry, changing B changes the flux $\Phi = BS$ through the semiclassical area S enclosed by the interference path. At low temperature and excitation, the experiments probe the FQH ground state reconstruction within the interference path, in the large electron island, and the island is not isolated from the 2D bulk.

Thus, minimization of the total energy of the electron system by quasiparticle excitation in the large island is analogous to that in an unbounded 2D system. This holds as far as the Aharonov-Bohm oscillations are involved, which, in the ground state, are intimately connected with quasiparticle excitation. Changing filling ν by quasiparticle excitation eventually leads to a transition to the next FQH state. The island confining potential causes its edge state structure; this is also true in a large, but not infinite 2D

electron system. As a transition from one quantum Hall ground state to another occurs, the edge channels move in space. Such effects are however related to transitions between neighboring quantum Hall states, change of Landau level filling ν, not to the Aharonov-Bohm physics. Experimentally, periodic Aharonov-Bohm oscillations once in a while exhibit a jump, or a "phase slip". The phase slips [like that at $B \approx 11.417$ T in Figure 6.4(a)] are presumably due to the secular edge channel movement related to changing ν that eventually causes the transition to the next quantum Hall plateau. The physics is different, however, and can be easily distinguished in a large device as not linked to the Aharonov-Bohm period. Note that ν does not depend on the device area, but Aharonov-Bohm period does. Thus, in a large area device, there are sequences of many periodic Aharonov-Bohm oscillations, occasionally interrupted by a "jump" due to edge channel movement on the microscopic scale.

In the hierarchical construction,[11, 105] the exact filling 2/5 FQH "daughter" condensate consists of a "maximum density droplet" of $-e/3$ quasielectrons in addition to the exact filling $f = 1/3$ condensate. The concentration of the $-e/3$ quasielectrons $n_{-e/3} = eB/5h$ is determined by their anyonic statistics. The resulting total electron charge density en corresponds to the $f = 2/5$ exact filling condensate. Thus, the $f = 2/5$ island embedded in $f = 1/3$ FQH fluid can be understood as the island of $-e/3$ hierarchy quasielectrons on top of the $f = 1/3$ condensate, the 1/3 condensate extends beyond the quasielectron droplet and completely surrounds it, see Figure 6.5.

The elementary charged excitations of the $f = 2/5$ condensate are the $\pm e/5$ quasielectrons and quasiholes, excited out of the condensate when the FQH fluid filling ν deviates from the exact filling 2/5. The density of the $\pm e/5$ quasiparticles can be obtained from conservation of the total electronic charge: $n_{\pm e/5} = \pm 5(f - \nu)eB/h$, where quasiholes are excited for $\nu < f$ and quasielectrons for $\nu > f$. In the island geometry, deviation of ν from f also causes change in the number of the $-e/3$ hierarchy quasielectrons: $N_{-e/3} = n_{-e/3}S = SeB/5h$ in the island of area S. The two experimental methods of varying filling ν are: (i) sweeping the magnetic field B, and (ii) changing

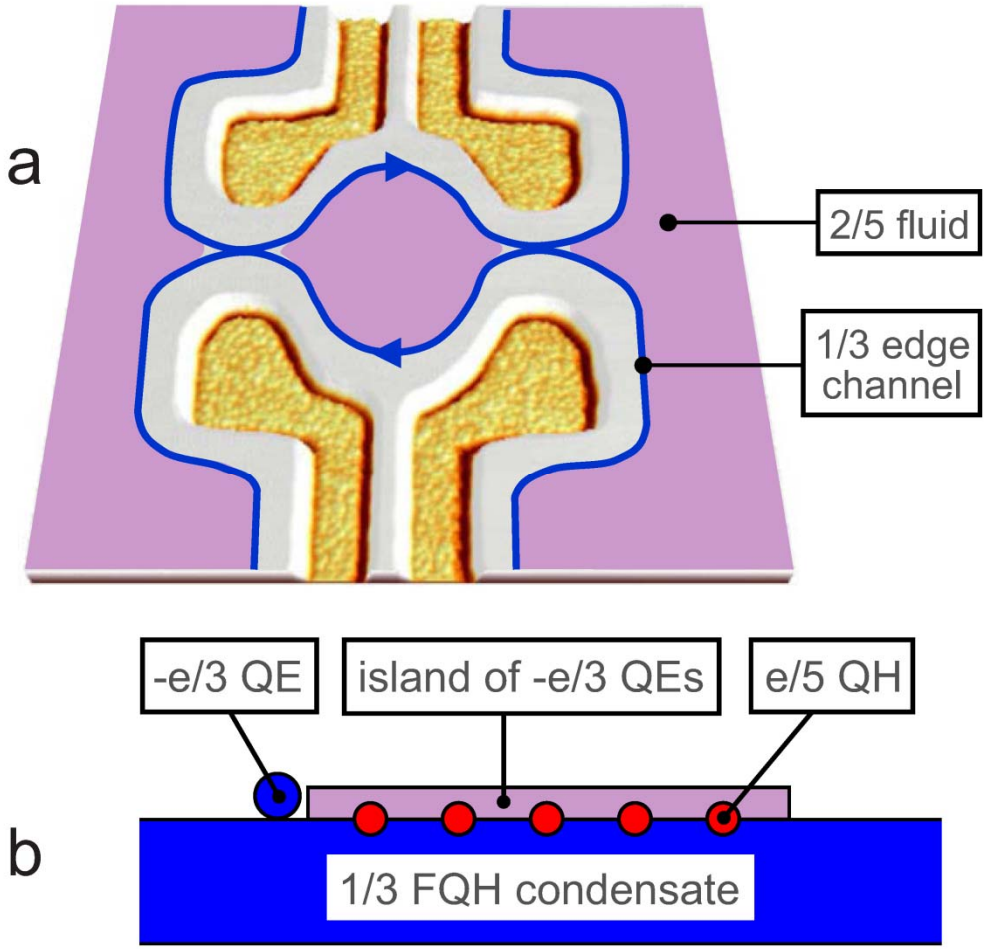

Figure 6.5: Atomic force (AFM) micrograph of the interferometer device with an illustration of the FQH filling profile. The transport current is carried in the 1/3 chiral edge channels. The path of the edge $-e/3$ quasielectrons is closed by tunneling in the two constrictions, and thus encircles the 2/5 island. (b) Illustration of the 2/5 island surrounded by 1/3 FQH fluid in the Haldane-Halperin hierarchy. The total 2D electron system is broken into three components: the incompressible exact filling 1/3 FQH condensate, the incompressible maximum density droplet of hierarchy $-e/3$ quasielectrons (QE), and the excited $e/5$ quasiholes (QH), appropriate for the $\nu < f = 2/5$ situation. A circling $-e/3$ QE is shown to the left of the island.

electron density n by sweeping the backgate voltage at a fixed B. In experiments, either B or n vary very slowly, so that near thermal equilibrium is maintained at any time.

When B is varied by a small δB, the equilibrium electron density profile (determined by the fixed positive background) is not affected except when transition to the next FQH state is considered, as discussed above. The island area is fixed by the large Coulomb energy, and the flux through the island $\Phi = BS$ is changed by $S\delta B$. The number of the $-e/3$ hierarchy quasielectrons in area S is incremented by $Se\delta B/5h$. Concurrently, the $f = 2/5$ island condensate electron density changes by $fe\delta B/h$, which results in excitation of $-e/5$ island quasiparticles, so as to maintain local charge neutrality of the total 2D electron system. Therefore, the minimal microscopic reconstruction of the island, the period $\delta B = \Delta_B$, occurs when one $-e/3$ hierarchy quasielectron is added, $Se\Delta_B/5h = 1$. This is exactly the observed $\Delta_\Phi = 5h/e$ flux periodicity. Within the period, increasing B, one $-e/3$ quasielectron is added to the island, the $f = 1/3$ condensate charge in area S increases by $-5e/3$, and ten $+e/3$ island quasiholes are excited. The total island electronic charge remains the same, $-e/3 - 5e/3 + 10(e/5) = 0$, within the unchanged area S.

This process can be expressed in terms of the Berry phase γ of the encircling $-e/3$ quasielectron, which includes the Aharonov-Bohm and the statistical contributions.[12, 101] Ref. 12 used the adiabatic theorem to calculate the Berry phase of quasiholes in the $f = 1/3$ Laughlin wave function on a disc. When a quasihole adiabatically executes a closed path, the wave function acquires a Berry phase. Taking counterclockwise as the positive direction, they found the difference between an "empty" loop, containing the FQH condensate "vacuum" only, and a loop containing another quasihole to be $\Delta\gamma_{1/3} = 4\pi/3$, identified as the statistical contribution.

We define the statistics parameter of the particles Θ so that upon exchange the wave function acquires a phase factor $\exp(i\pi\Theta)$. Then $\Theta_{1/3} = \Theta_{-1/3}$ is the statistics of $\pm e/3$ quasiparticles of the $f = 1/3$ FQH fluid, and $\Theta_{2/5}^{-1/3}$ is involved when a $-e/3$ quasielectron encircles a $e/5$ quasihole of the $f = 2/5$ island fluid, the "mutual statistics" of different kinds of quasiparticles.[106-107] Ref. 101 derives and solves the Berry

phase γ equation describing the present experimental situation. It obtains Berry phase period $\Delta_\gamma = 2\pi$:

$$\frac{\Delta_\gamma}{2\pi} = -\frac{5}{3} + \Theta_{1/3} + 10\Theta_{2/5}^{-1/3} = 1. \tag{6.1}$$

Two concurrent physical processes comprise the period: increase by one in the number of island hierarchy $-e/3$ quasielectrons, and the excitation of ten $e/5$ quasiholes in the island. Thus, the physics under consideration leads to interpretation of Equation (6.1) as two simultaneous equations, each with an integer Berry phase period:

$$1/3 + \Theta_{1/3} = 1 \tag{6.2a}$$

and

$$10\Theta_{2/5}^{-1/3} = 2. \tag{6.2b}$$

Equation (6.2a) is identical to that obtained when only $e/3$ quasiparticles are present (no 2/5 island).[12, 30, 38] Equation (6.2b) can be understood as sum of two $5\Theta_{2/5}^{-1/3} = 1$ equations, one for each of the two kinds of $e/5$ quasiparticles of the $f = 2/5$ condensate (the quantum numbers of the two kinds are expected to be identical). These equations are solved by $\Theta_{1/3} = 2/3$ and $\Theta_{2/5}^{-1/3} = 1/5$. The value $\Theta_{1/3} = 2/3$ is in agreement with the expectation and with recent experiments.[14, 30, 38] The value $\Theta_{2/5}^{-1/3} = 1/5$ appears to be consistent with what would be obtained in a Berry phase calculation similar to that of Ref. 12, by the Cauchy's theorem, including the charge deficiency in the 2/5 condensate created by excitation of an $e/5$ quasihole vortex, and maintaining the path of the adiabatically encircling $-e/3$ quasielectron fixed. Also, note that a $2.5h/e$ period (excitation of five island quasiparticles) were possible if $\Theta_{1/3}$ were an integer, that is, if the encircling $e/3$ quasiparticles were either bosons or fermions. Thus, the observed $5h/e$ superperiod requires both $\Theta_{2/5}^{-1/3}$ and $\Theta_{1/3}$ are anyonic. The relative (mutual) statistics of quasiparticles of the two FQH condensates at different filling are meaningful because both quasiparticle kinds are different collective excitations of a single highly correlated electron system comprising the parent-daughter FQH fluid with different fillings.

The same Berry phase equation describes the physically different process of the island charging by the backgate.[88, 101] Here, in a fixed B, increasing positive V_{BG} increases the 2D electron density. The exact filling FQH condensate electron (and charge) density is fixed by the fixed B. The period consists of creating ten $-e/5$ quasielectrons out of the 2/5 FQH condensate within the interference path, while the path area increases by $5h/eB$ in the fixed B. Excitation of quasiparticles while the condensate density is fixed is possible because the condensate is not isolated from the bulk 2D electron system, and the charge imbalance is ultimately supplied from the contacts. Note that there is one more $-e/3$ hierarchy quasielectron in the 2/5 condensate of increased area $S+5h/eB$. Thus, increasing ν by charging the island by the uniform electric field of the remote backgate is accommodated by creation of $-e/5$ quasielectrons and by concurrent outward shift of the $1/3-2/5$ boundary, that is, the interference path. Ten $-e/5$ quasielectrons are excited out of the condensate (or, equivalently, ten quasiholes are absorbed into the condensate), the fixed condensate density is restored from the contacts, in constant B, the total FQH fluid electronic charge (condensate plus quasiparticles) changes by $-2e$ per S, the charge period.

Single-particle theory predicts Aharonov-Bohm flux period $\Delta_\Phi = 2\pi\hbar/q$ for charge q particles.[75-76] This period is also expected for many-particle systems if the particle exchange statistics is integer, Fermi or Bose. In interacting many-electron systems, effective low-energy quasiparticles may have charge $q \neq e$. In the multiply-connected many-electron system, if a "fluxon" h/e is added in the region of space from which the electrons are excluded (electron vacuum), the added flux can be annulled by a singular gauge transformation, leaving the many-electron system in the same state as before, and superperiods $> h/e$ are not possible even when $q < e$.[75-76] In our experiments, however, a uniform magnetic field is varied, rather than flux is inserted in the region of electron vacuum, and the situation is more subtle. The added flux results from increase in the applied magnetic field. The interacting electron system does reconstruct periodically, quasiparticles are excited, and the many-electron system is not in the same microscopic state as before. Thus, gauge invariance does not preclude superperiods in the Fabry-Perot interferometer geometry, where there is no electron vacuum within the interference path.

Chapter 7

Conclusions

In summary, we realized two kinds of novel Laughlin quasiparticle interferometers. The central interference region of the interferometer consists of two constrictions defined by etch trenches in the two-dimensional electron layer, enclosing an approximately circular island. In the quantum Hall regime, currents are carried by counterpropagating edge channels at the periphery of the two-dimensional electron system. Edge channels are coupled by coherent tunneling in the constrictions, resulting in a closed interference path around the electron island, and production interference oscillations in the detected magnetoresistance.

In the first device, we find that application of front-gate voltage affects the constriction electron density, while the bulk density remains unaffected. This results in quantized plateaus in longitudinal resistance, while the Hall resistance is dominated by the low-density, low-filling constriction. At lower field, when the quantum Hall plateaus fail to develop, we observe bulk Shubnikov-de Haas oscillations in series corresponding to an integer filling of the magnetoelectric subbands in the constriction. From a Fock-Darwin analysis, we obtain the constriction electron density as a function of the front gate bias and, the zero-field number of 1D electric subbands (conductance channels), resulting from the electron confinement in the constrictions.

In the same interferometer, by carefully tuning the constriction front gates, we find a regime where interference oscillations with period $h/2e$ persist throughout the transition between the integer quantum Hall plateaus 2 and 3, including half-filling. In our experiment, neither period nor amplitude of the oscillations show a discontinuity at half-filling. The continuous experimental oscillation sequence indicates that only one

interference path exists throughout the transition. We also present experiments and an analysis of the front-gate dependence of the phase of the oscillations. The results point to a single physical mechanism of the observed conductance oscillations: Aharonov-Bohm interference of interacting electrons in quantum Hall regime

In the second interferometer, we realize the situation that $e/3$ Laughlin quasiparticles execute a closed path around an island of the 2/5 FQH fluid. Most of the island area is occupied by the 2/5 FQH fluid, so that the directly-measured magnetic field period well approximates the flux period. The central experimental results obtained, that is, the flux and charge superperiods of $\Delta_\Phi = 5h/e$ and $\Delta_Q = 2e$, are robust and do not involve any adjustable parameter fitting to a model. In Section III we presented a microscopic model of the origin of the superperiod based on the Haldane-Halperin fractional-statistics hierarchical construction of the 2/5 FQH fluid. The superperiod comprises incrementing by one the state number of the $-e/3$ quasielectron circling the island and concurrent excitation of ten $e/5$ quasiparticles in the island 2/5 fluid. Variation of the magnetic field does not affect the charge state of the island. Quantization of the Berry phase of the circling $e/3$ quasiparticles in integer multiples of 2π gives anyonic statistics $\Theta_{1/3} = 2/3$ for the $e/3$ quasiparticles, and $\Theta_{2/5}^{-1/3} = 1/5$, the mutual statistics, when a $-e/3$ quasielectron encircles a $e/5$ quasihole of the 2/5 fluid.

Bibliography

[1] K. von Klitzing, G. Dorda, and M. Pepper, Phys. Rev. Lett. **45**, 494 (1980).

[2] D. C. Tsui, H. L. Stormer, and A. C. Gossard, Phys. Rev. Lett. **48**, 1559 (1982).

[3] R. E. Prange and S. M. Girvin eds., *The Quantum Hall Effect* (Springer, New York, 1990).

[4] D. Yoshioka, *The Quantum Hall Effect* (Springer, New York, 2002).

[5] T. Chakraborty and P. Pietilainen, *The Quanum Hall Effects, Springer Series in Solid State Sciences* (Springer, Berlin, 1990).

[6] Y. B. Zhang, Y. W. Tan, H. L. Stormer, and P. Kim, Nature **438**, 201 (2005).

[7] K. S. Novoselov, A. K. Geim, S. V. Morozov, D. Jiang, M. I. Katsnelson, I. V. Grigorieva, S. V. Dubonos, and A. A. Firsov, Nature **438**, 197 (2005).

[8] X. Du, I. Skachko, F. Duerr, A. Luican, and E. Y. Andrei, Nature **462**, 192 (2009).

[9] R. B. Laughlin, Phys. Rev. B **23**, 5632 (1981).

[10] R. B. Laughlin, Phys. Rev. Lett. **50**, 1395 (1983).

[11] B. I. Halperin, Phys. Rev. Lett. **52**, 1583 (1984).

[12] D. Arovas, J. R. Schrieffer, and F. Wilczek, Phys. Rev. Lett. **53**, 722 (1984).

[13] J. K. Jain, Phys. Rev. Lett. **63**, 199 (1989).

[14] V. J. Goldman and B. Su, Science **267**, 1010 (1995).

[15] I. J. Maasilta and V. J. Goldman, Phys. Rev. Lett. **84**, 1776 (2000).

[16] V. J. Goldman, I. Karakurt, J. Liu, and A. Zaslavsky, Phys. Rev. B **64**, 085319 (2001).

[17] V. J. Goldman, J. Korean Phys. Soc. **39**, 512 (2001).

[18] F. E. Camino, W. Zhou, and V. J. Goldman, Phys. Rev. Lett. **95**, 246802 (2005).

[19] F. E. Camino, W. Zhou, and V. J. Goldman, Phys. Rev. B **72**, 155313 (2005).

[20] F. E. Camino, W. Zhou, and V. J. Goldman, Phys. Rev. B **72**, 075342 (2005).

[21] J. M. Leinaas and J. Myrheim, Nouvo Cimento Soc. Ital. Fis., B **37B**, 1 (1977).

[22] F. Wilczek, Phys. Rev. Lett. **48**, 1144 (1982).

[23] F. Wilczek, Phys. Rev. Lett. **49**, 957 (1982).

[24] C. D. C. Chamon, D. E. Freed, S. A. Kivelson, S. L. Sondhi, and X. G. Wen, Phys. Rev. B **55**, 2331 (1997).

[25] P. Bonderson, A. Kitaev, and K. Shtengel, Phys. Rev. Lett. **96**, 016803 (2006).

[26] R. Ilan, E. Grosfeld, and A. Stern, Phys. Rev. Lett. **100** (2008).

[27] A. Stern and B. I. Halperin, Phys. Rev. Lett. **96**, 016802 (2006).

[28] F. E. Camino, W. Zhou, and V. J. Goldman, Phys. Rev. B **74**, 115301 (2006).

[29] F. E. Camino, W. Zhou, and V. J. Goldman, Phys. Rev. B **76**, 155305 (2007).

[30] F. E. Camino, W. Zhou, and V. J. Goldman, Phys. Rev. Lett. **98**, 076805 (2007).

[31] W. Zhou, F. E. Camino, and V. J. Goldman, Phys. Rev. B **73**, 245322 (2006).

[32] R. B. Laughlin, Rev. Mod. Phys. **71**, 863 (1999).

[33] R. L. Willett, H. L. Stormer, D. C. Tsui, A. C. Gossard, and J. H. English, Phys. Rev. B **37**, 8476 (1988).

[34] F. D. M. Haldane and E. H. Rezayi, Phys. Rev. Lett. **54**, 237 (1985).

[35] F. D. M. Haldane, Phys. Rev. Lett. **51**, 605 (1983).

[36] J. K. Jain, Science **266**, 1199 (1994).

[37] J. K. Jain and V. J. Goldman, Phys. Rev. B **45**, 1255 (1992).

[38] V. J. Goldman, J. Liu, and A. Zaslavsky, Phys. Rev. B **71**, 153303 (2005).

[39] B. J. van Wees, L. P. Kouwenhoven, C. J. P. M. Harmans, J. G. Williamson, C. E. Timmering, M. E. I. Broekaart, C. T. Foxon, and J. J. Harris, Phys. Rev. Lett. **62**, 2523 (1989).

[40] L. P. Kouwenhoven, B. J. van Wees, K. J. P. M. Harmans, and J. G. Williamson, Surf. Sci. **229**, 290 (1990).

[41] R. Willett, J. P. Eisenstein, H. L. Störmer, D. C. Tsui, A. C. Gossard, and J. H. English, Phys. Rev. Lett. **59**, 1776 (1987).

[42]W. Pan, J. S. Xia, V. Shvarts, D. E. Adams, H. L. Stormer, D. C. Tsui, L. N. Pfeiffer, K. W. Baldwin, and K. W. West, Phys. Rev. Lett. **83**, 3530 (1999).

[43]B. I. Halperin, Phys. Rev. B **25**, 2185 (1982).

[44]A. H. Macdonald and P. Streda, Phys. Rev. B **29**, 1616 (1984).

[45]X. G. Wen, Int. J. Mod. Phys. B **6**, 1711 (1992).

[46]D. B. Chklovskii, B. I. Shklovskii, and L. I. Glazman, Phys. Rev. B **46**, 4026 (1992).

[47]B. Y. Gelfand and B. I. Halperin, Phys. Rev. B **49**, 1862 (1994).

[48]S. Ihnatsenka and I. V. Zozoulenko, Phys. Rev. B **77**, 235304 (2008).

[49]A. Baumgartner, T. Ihn, K. Ensslin, K. Maranowski, and A. C. Gossard, Phys. Rev. B **76**, 085316 (2007).

[50]G. F. Giuliani and G. Vignale, *Quantum Theory of the Electron Liquid* (Cambridge Unviversity Press, Cambridge, 2005).

[51]B. J. van Wees, H. van Houten, C. W. J. Beenakker, J. G. Williamson, L. P. Kouwenhoven, D. van der Marel, and C. T. Foxon, Phys. Rev. Lett. **60**, 848 (1988).

[52]D. A. Wharam, et al., J. Phys. C **21**, L209 (1988).

[53]H. van Houten, C. W. J. Beenakker, and A. A. M. Staring, *Single Charge Tunneling* (Plenum, New York, 1992).

[54]W. Zhou, F. E. Camino, and V. J. Goldman, AIP Conf. Proc. **850**, 1351 (2006).

[55]M. D. Godfrey, P. Jiang, W. Kang, S. H. Simon, K. W. Baldwin, L. N. Pfeiffer, and K. W. West, arXiv:0708.2448 (unpublished) (2007).

[56]C. M. Marcus, (Private communication).

[57]R. L. Willett, L. N. Pfeiffer, and K. W. West, Proc. Nat. Acad. Sci. USA **106**, 8853 (2009).

[58]C. Nayak, S. H. Simon, A. Stern, M. Freedman, and S. Das Sarma, Rev. Mod. Phys. **80**, 1083 (2008).

[59]A. Stern, Ann. Phys. **323**, 204 (2008).

[60]P. Bonderson, M. Freedman, and C. Nayak, Ann. Phys. **324**, 787 (2009).

[61]M. Shayegan, V. J. Goldman, M. Santos, T. Sajoto, L. Engel, and D. C. Tsui, Appl. Phys. Lett. **53**, 2080 (1988).

[62] R. J. Haug, A. H. Macdonald, P. Streda, and K. Vonklitzing, Phys. Rev. Lett. **61**, 2797 (1988).

[63] L. D. Landau and E. M. Lifshitz, (Pergamon, London, 1984), Vol. 8.

[64] V. J. Goldman, B. Su, and J. K. Wang, Phys. Rev. B **47**, 10548 (1993).

[65] M. Büttiker, Phys. Rev. B **38**, 9375 (1988).

[66] J. K. Jain and S. A. Kivelson, Phys. Rev. B **37**, 4276 (1988).

[67] J. K. Wang and V. J. Goldman, Phys. Rev. B **45**, 13479 (1992).

[68] I. M. Ruzin, S. Marianer, and B. I. Shklovskii, Phys. Rev. B **46**, 3999 (1992).

[69] V. Fock, Z. Phys. **47**, 446 (1928).

[70] C. G. Darwin, Proc. Cambridge Philos. Soc. **27**, 86 (1931).

[71] R. B. Dingle, Proc. R. Soc. London, Ser. A **211**, 500 (1952).

[72] S. B. Kaplan and A. C. Warren, Phys. Rev. B **34**, 1346 (1986).

[73] B. J. van Wees, L. P. Kouwenhoven, H. Vanhouten, C. W. J. Beenakker, J. E. Mooij, C. T. Foxon, and J. J. Harris, Phys. Rev. B **38**, 3625 (1988).

[74] A. Sididiki, (Private communication).

[75] Y. Aharonov and D. Bohm, Phys. Rev. **115**, 485 (1959).

[76] Y. Aharonov and D. Bohm, Phys. Rev. **123**, 1511 (1961).

[77] C. N. Yang, Rev. Mod. Phys. **34**, 694 (1962).

[78] I. Karakurt, V. J. Goldman, J. Liu, and A. Zaslavsky, Phys. Rev. Lett. **87**, 146801 (2001).

[79] V. J. Goldman, J. Liu, and A. Zaslavsky, Phys. Rev. B **77**, 115328 (2008).

[80] M. Kataoka, C. J. B. Ford, G. Faini, D. Mailly, M. Y. Simmons, D. R. Mace, C. T. Liang, and D. A. Ritchie, Phys. Rev. Lett. **83**, 160 (1999).

[81] H. S. Sim, M. Kataoka, and C. J. B. Ford, Phys. Rep. **456**, 127 (2008).

[82] S. Ihnatsenka, I. V. Zozoulenko, and G. Kirczenow, Phys. Rev. B **80**, 115303 (2009).

[83] I. Giaever and H. R. Zeller, Phys. Rev. Lett. **20**, 1504 (1968).

[84] K. K. Likharev, Proc. IEEE **87**, 606 (1999).

[85]M. W. C. Dharma-wardana, R. P. Taylor, and A. S. Sachrajda, Solid State Commun. **84**, 631 (1992).

[86]N. Y. Hwang, S. R. E. Yang, H. S. Sim, and H. Yi, Phys. Rev. B **70**, 085322 (2004).

[87]B. Rosenow and B. I. Halperin, Phys. Rev. Lett. **98**, 106801 (2007).

[88]G. A. Fiete, G. Refael, and M. P. A. Fisher, Phys. Rev. Lett. **99**, 166805 (2007).

[89]Y. M. Zhang, D. T. McClure, E. M. Levenson-Falk, C. M. Marcus, L. N. Pfeiffer, and K. W. West, Phys. Rev. B **79**, 241304 (2009).

[90]D. T. McClure, Y. M. Zhang, B. Rosenow, E. M. Levenson-Falk, C. M. Marcus, L. N. Pfeiffer, and K. W. West, Phys. Rev. Lett. **103**, 206806 (2009).

[91]P. V. Lin, F. E. Camino, and V. J. Goldman, Phys. Rev. B **78**, 245322 (2008).

[92]T. Nakajima, T. Ueda, and S. Komiyama, J. Phys. Soc. Jpn. **76**, 094703 (2007).

[93]L. V. Litvin, A. Helzel, H. P. Tranitz, W. Wegscheider, and C. Strunk, Phys. Rev. B **78**, 075303 (2008).

[94]Y. Ji, Y. C. Chung, D. Sprinzak, M. Heiblum, D. Mahalu, and H. Shtrikman, Nature **422**, 415 (2003).

[95]P. Roulleau, F. Portier, P. Roche, A. Cavanna, G. Faini, U. Gennser, and D. Mailly, Phys. Rev. Lett. **100**, 126802 (2008).

[96]R. de-Picciotto, M. Reznikov, M. Heiblum, V. Umansky, G. Bunin, and D. Mahalu, Nature **389**, 162 (1997).

[97]L. Saminadayar, D. C. Glattli, Y. Jin, and B. Etienne, Phys. Rev. Lett. **79**, 2526 (1997).

[98]F. Wilczek, The Spin, 61 (2008).

[99]P. V. Lin, F. E. Camino, and V. J. Goldman, Phys. Rev. B **80**, 125310 (2009).

[100]E. A. Kim, Phys. Rev. Lett. **97**, 216404 (2006).

[101]V. J. Goldman, Phys. Rev. B **75**, 045334 (2007).

[102]K. W. Chen and C. R. Chang, Phys. Rev. B **78**, 235319 (2008).

[103]J. K. Jain and C. Shi, Phys. Rev. Lett. **96**, 136802 (2006).

[104]N. Byers and C. N. Yang, Phys. Rev. Lett. **7**, 46 (1961).

[105]F. D. M. Haldane, Physical Review Letters **51**, 605 (1983).

[106]F. Wilczek, Phys. Rev. Lett. **69**, 132 (1992).

[107]W. P. Su, Y. S. Wu, and J. Yang, Phys. Rev. Lett. **77**, 3423 (1996).